MOTION ESTIMATION AND MOTION-COMPENSATED RECONSTRUCTION FOR FOUR-DIMENSIONAL CONE BEAM COMPUTED TOMOGRAPHY (4D-CBCT)

APPROVED BY SUPERVISORY COMMITTEE

NOTE: The top line is for the Supervising Professor's name. There should be as many lines as there are members of the committee. All signatures must be original and in ink. Adjust "Approved by Supervisory Committee" line upward if the committee list is very large.

Jing Wang, Ph.D

Xun Jia, Ph.D

Xiankai Sun, Ph.D

Steve Jiang, Ph.D

DEDICATION

To my parents

MOTION ESTIMATION AND MOTION-COMPENSATED RECONSTRUCTION FOR FOUR-DIMENSIONAL CONE BEAM COMPUTED TOMOGRAPHY (4D-CBCT)

by

XIAOKUN HUANG

DISSERTATION

Presented to the Faculty of the Graduate School of Biomedical Sciences

The University of Texas Southwestern Medical Center at Dallas

In Partial Fulfillment of the Requirements

For the Degree of

DOCTOR OF PHILOSOPHY
The University of Texas Southwestern Medical Center at Dallas

Dallas, Texas

May, 2020

MOTION ESTIMATION AND MOTION-COMPENSATED RECONSTRUCTION FOR FOUR-DIMENSIONAL CONE BEAM COMPUTED TOMOGRAPHY (4D-CBCT) AND APPLICATION

Xiaokun Huang

The University of Texas Southwestern Medical Center at Dallas, 2020

Supervising Professor: Jing Wang Ph.D

The emerging of sophisticated radiation therapy such as stereotactic body radiation therapy (SBRT) characterizing as high dose in each fraction and few fraction number requires higher accuracy for tumor localization. For organs influenced by the respiration, respiration induced motion becomes the principal cause for tumor localization uncertainty and four dimensional (4D) cone beam computed tomography (CBCT) has been developed to locate tumor in each respiration phase to better estimate the possible motion range of the tumor motion during the treatment. However, 4D-CBCT reconstructed by conventional methods on current commercial scanners is

not optimal for tumor localization due to low image quality caused by insufficient number of projections located in each phase after the projection binning according to respiration phases.

The specific aims of this dissertation research are to: 1) improving the accuracy of inter-phase motion model to feed in a motion-compensated reconstruction scheme to improve the 4D-CBCT image quality; 2) utilizing high-quality 4D-CBCT for motion evaluation and 4D dose accumulation for lung cancer patients receiving SBRT. The motion-compensated reconstruction suppresses motion and improves image quality by deforming other phase image to the reference phase using inter-phase motion model to reconstruct reference phase image using projections from all phases. Therefore, it is essential to improve the inter-phase motion model accuracy. Two methods, biomechanical modeling based and convolutional neural network (CNN) based, were applied to fine-tune the inner lung motion model. The biomechanical modeling is a physics-driven method which introduced tissue related elasticity properties to simulate the movement of lung and solve the deformation by finite-element analysis. Biomechanical modeling requires boundary condition which is the deformation vector fields (DVFs) estimated from a 2D-3D registration. For CNN based methods, boundary DVFs are also used as the input for the U-net based architectures to predict the inner lung motion. All methods can improve accuracy of DVFs and further improve reconstructed 4D-CBCT images quality. After obtaining high-quality 4D-CBCT images, we created a tool using 4D-CBCT images to evaluate the motion variation as well as calculate the accumulated 4D dose to monitor and evaluate the delivered dose for lung SBRT patients.

TABLE OF CONTENTS

PRIOR PUBLICATIONS

PEER-REVIEWD JOURNAL PUBLICATIONS

Huang, X., Zhang, Y., Chen, L., & Wang, J. U-net-based Deformation Vector Field Estimation for Motion-Compensated 4D-CBCT Reconstruction. *Medical Physics*.

Zhang, Y., **Huang, X.** & Wang, J. Advanced 4-dimensional cone-beam computed tomography reconstruction by combining motion estimation, motion-compensated reconstruction, biomechanical modeling and deep learning. Vis. Comput. Ind. Biomed. Art 2, 23 (2019) doi:10.1186/s42492-019-0033-6

Zhang, Y., Folkert, M. R., **Huang, X.**, Ren, L., Meyer, J., Tehrani, J. N., ... & Wang, J. (2019). Enhancing liver tumor localization accuracy by prior-knowledge-guided motion modeling and a biomechanical model. Quantitative imaging in medicine and surgery, 9(7), 1337.

Zhang, Y., Folkert, M. R., Li, B., **Huang, X.**, Meyer, J. J., Chiu, T., ... & Jia, X. (2019). 4D liver tumor localization using cone-beam projections and a biomechanical model. Radiotherapy and Oncology, 133, 183-192.

Zhao, C., Zhong, Y., Duan, X., Zhang, Y., **Huang, X.**, Wang, J., & Jin, M. (2018). 4D cone-beam computed tomography (CBCT) using a moving blocker for simultaneous radiation dose reduction and scatter correction. Physics in Medicine & Biology, 63(11), 115007.

Huang, X., Zhang, Y., & Wang, J. (2018). A biomechanical modeling-guided simultaneous motion estimation and image reconstruction technique (SMEIR-Bio) for 4D-CBCT reconstruction. Physics in Medicine & Biology, 63(4), 045002.

Huang, X., Zhang, Y., & Wang, J. (2017, March). A biomechanical modeling guided simultaneous motion estimation and image reconstruction technique (SMEIR-Bio) for 4D-CBCT reconstruction. In Medical Imaging 2017: Physics of Medical Imaging (Vol. 10132, p. 101322B). International Society for Optics and Photonics.

CONFERENCE ABSTRACTS

Huang, X., Zhang, Y., & Wang, J, (2020, March.) U-net based Automatic CBCT based Liver Tumor Localization using Biomechanical modeling, CT Meeting

Huang, X., Zhang, Y., & Wang, J, (2019, July.) Deformation vector field estimation using convolutional neural network for motion-compensated 4D-CBCT reconstruction, American Association of Physicist in Medicine

Huang, X., Zhang, Y., & Wang, J, (2019, June.) U-net based deformation vector field estimation for motion-compensated 4D-CBCT reconstruction, The International Conference on the Use of Computers in Radiation Therapy

Huang, X., Zhang, Y., & Wang, J, (2018, July.) Characterizing inter-fraction motion variation for lung SBRT patients using 4D-CBCT reconstructed by simultaneous motion estimation and image reconstruction, American Association of Physicist in Medicine

Huang, X., Zhang, Y., & Wang, J, (2018, July.) Dose reconstruction for lung Stereotactic Body Radiation Therapy (SBRT) patients using on-board 4D Cone-beam CT, American Association of Physicist in Medicine

Zhang, Y., Chiu, T., Li, B., Folkert, M., **Huang, X.**, Jia, X., & Wang, J, (2018, August.) Comprehensive Evaluation of a Biomechanical Modeling-Guided CBCT Reconstruction Technique (Bio-Recon) for Liver Imaging, American Association of Physicist in Medicine

Niu, S., Zhong, Y., **Huang, X.**, Zhang, Y., Ma, J., Wang, J. (2018, August.) Noise Suppression in Image-Domain Material Decomposition for Triple-Energy CT, American Association of Physicist in Medicine

Huang, X., Zhang, Y., & Wang, J, (2017, July.) A biomechanical modeling guided simultaneous motion estimation and image reconstruction technique (SMEIR-Bio) for 4D-CBCT, American Association of Physicist in Medicine

Huang, X., Guo, H., (2014, Jan) Compressed Sensing Reconstruction for T1rho Imaging, The 2nd International Congress on Magnetic Resonance Imaging & The 19th Annual Scientific Meeting of KSMRM

LIST OF FIGURES

LIST OF TABLES

LIST OF DEFINITIONS

3D-CBCT – three dimensional cone beam computed tomography

4D-CBCT – four dimensional cone beam computed tomography

aSi – amorphous Silicon

ART-TV – total variation-regularized algebraic reconstruction technique

ART – adaptive radiation therapy

CBCT – cone beam computed tomography

CNN – convolutional neural network

CT – computed tomography

DIR – deformable image registration

DRR – digitally reconstructed radiograph

DVF – deformation vector field

DVH – dose-volume-histograms

EPID – electronic portal imaging device

FBP – filtered back projection

FDK – Feldkamp-Davis-Kress

FOV – field of view

HU – Hounsfield unit

GPU – graphic processing units

IGART – image-guided adaptive radiation therapy

IGRT – image-guided radiation therapy

IMRT – Intensity modulated radiation therapy

ITV – internal target volume

KV – kilovoltage

LINAC – linear accelerator

MC-SART – motion-compensated simultaneous algebraic reconstruction technique

MRI – magnetic resonance imaging

MV – megavoltage

NCC – normalized cross correlation

NSCLC – Non-small cell lung cancer

OAR – organ at risks

PET – positron emission tomography

PTV – planning target volume

RE – relative error

RMSE – root mean square error

ROI – region of interest

SART – simultaneous algebraic reconstruction technique

SBRT – stereotactic body radiation therapy

SMEIR – simultaneous motion estimation and image reconstruction

SMEIR-Bio – simultaneous motion estimation and image reconstruction combined with biomechanical modeling

TFT – thin film transistor

TV – total variation

U-net-3C – U-net structure with 3 channels of DVFs as input to fine-tuning DVFs

U-net-4C – U-net structure with 3 channels DVFs and one additional CBCT image channel as input to fine-tuning DVFs

UQI – universal quality index

US – ultrasound

1 CHAPTER ONE
Introduction

1.1 IMAGE GUIDED RADIATION THERAPY

1.1.1 Brief introduction of radiation therapy

Cancer is the leading cause of death world-wide. Radiation therapy play a critical role in cancer treatment that about 50 percentages of cancer patients receive radiation therapy alone or along with other treatment such as surgery, chemotherapy and immunotherapy[1]. External beam radiation therapy is the most common type of radiation therapy which has been used for multiple cancer sites treatment [2].

The development of radiation therapy originated in 1895, when Wilhelm Roentgen from Germany discovered X-ray which enables people to see the inside structure of human body. The clinical usage of ionization is appreciated and investigated. In 1911, Marie Curie won her second Nobel Prize in the division of chemistry for her researches into radioactive elements, discovering radium and polonium. They became the pioneers who lead people to find the pathway for both diagnostic (X-ray) and cancer treatment (radio-activities) in the practice of medicine.

The radiation therapy developed along with the effort to obtain standardized high-energy radiation as well as the investigation of radiobiology and radiation metrology. External beam radiation therapy started from superficial and orthovoltage therapy generated by X-ray tubes. In 1910's, Coolidge developed “hot cathode tube” to emit kilovoltage (KV) X-ray to treat cancers imbedded deeper inside body[3]. In 1950s, radiation therapy stepped from Orthovoltage era into Megavoltage (MV) era. The invention of teletherapy through sealed cobalt 60 sources by H.E.

Johns in Canada enabled high-photon-energy radiation. Meanwhile, the invention of linear accelerator (LINAC) brought megavoltage radiation therapy into reality[1, 4]. MV-LINAC treats deep tumor inside by delivering high-energy photon beams to achieve better tumor control and less side effects.

The evolution of sophisticated radiation therapy techniques has made radiation therapy become a recognized medical specialty. 3D Conformal radiotherapy uses computed tomography (CT) images to localize tumor and delineate critical tissues to optimize beam placement and shielding. Intensity modulated radiation therapy (IMRT) characterized by modulating radiation beams to make the radiation dose to conform more precisely to the three-dimensional shape of the tumor and to spare normal tissues. Image guided radiation therapy (IGRT) further improves the conformality of radiation dose by increasing the tumor localization accuracy using imaging modalities to avoid or decrease impact generated from tumor motion and patient setup errors[1]. The most advanced radiation therapy, adaptive radiation therapy (ART) broke the assumption that daily anatomy remains the same as treatment planning and focused on modifying treatment plan to improve the delivery accuracy by considering patients anatomical changes through treatment courses. Information collected in images was feed to plan to ensure the optimal tumor coverage and normal tissue sparing. ART, which requires images to provide anatomical geometry, is also called image guided adaptive radiation therapy (IGART) [5].

1.1.2 Image guided radiation therapy

Image guided radiation therapy is an advanced paradigm to address problems emerging from inter- and intra-fractional anatomic variations. IGRT is the combination of advanced imaging techniques and conformal radiation therapy with expectation to improve the accuracy of tumor targeting to maximize the dose deposited to the targets while minimize the dose deposited to surrounding normal tissue. IGRT can achieve high accuracy tumor localization by considering anatomical variations through the whole treatment procedures.

Variety of imaging modalities are used in IGRT to acquire images contains anatomical geometry to better localize the tumor. Computed tomography (CT), ultrasound (US) and magnetic resonance imaging (MRI) are typical imaging modalities used to acquire anatomy inside of the body. Functional information embedded in positron-emitted tomography (PET) or dynamic contrast-enhanced MRI (DCE-MRI) images integrated with geometric information can boost the accuracy of tumor targeting [6, 7].

Imaging technologies are primarily been employed in 3 stages in a radiation therapy treatment process: 1) treatment simulation and treatment planning; 2) patient setup; 3) localization of the target during beam delivery. For treatment planning, CT/PET/MRI can be utilized individually or combined to visualize inside body structures to determine the shape and location of the tumor. CT-simu or MRI-simu is used to conduct a treatment simulation session and to create reference images for treatment. Patient setup requires US/In-room CT/radiographic imaging/cone-beam computed tomography (CBCT) to obtain patient's anatomy at the treatment position and align the on-board image to the reference image to correct or verify the patient setup.

1.1.3 Image guided adaptive radiation therapy

The emerging of IGRT enables the image guided adaptive radiation therapy. The principle of adaptive radiation therapy is to modify the treatment planning according to the anatomic change during a treatment course. Therefore the treatment plan can be adapted to patient's updated anatomy with optimized dose distribution.

The IGART composed of 3 main steps: Image guidance, dose verification and treatment adaptation. Image guidance obtains the patient anatomy on the treatment day. The difference between anatomy on the planning day and that on the treatment day are evaluated based on the shape and location of tumors and surrounding organs at risk (OAR). Dose verification recalculated the dose distribution based on the anatomy of the treatment day, which is obtained in the image guidance step. Treatment adaptation aims on optimizing dose distribution for both tumor and OARs aiming to minimize the discrepancies between the anatomies of treatment and planning. Several methods have been explored to achieve treatment adaption, including patient re-positioning, plan optimization and re-planning. The relationship between these 3 steps is shown in Figure 1-1. Image guidance provides imaging information to dose verification and treatment adaptation to optimize and finalize the treatment.

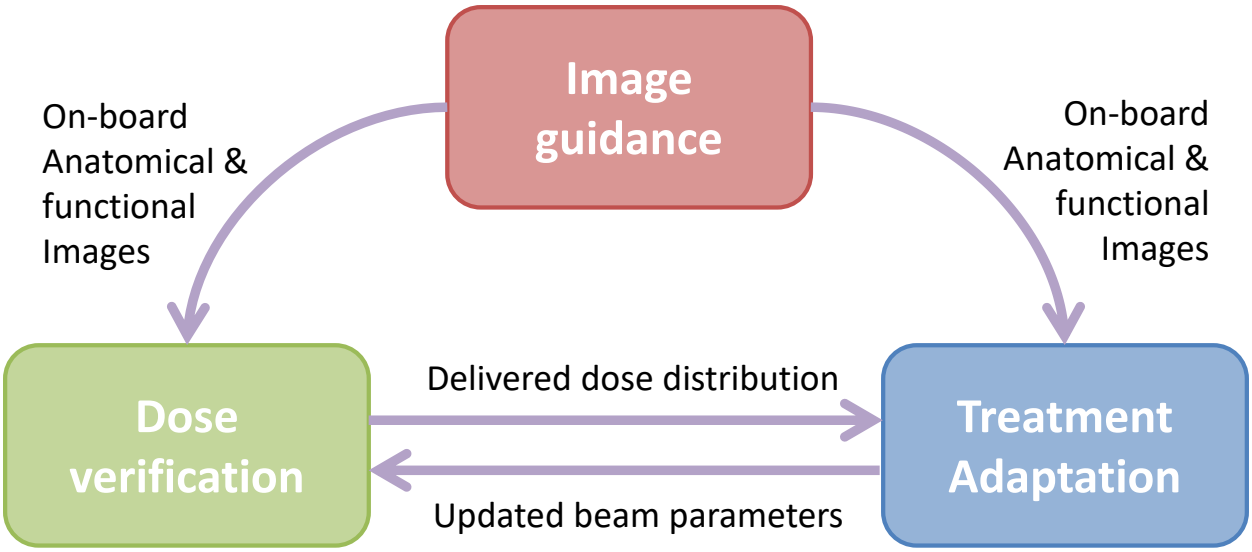

Figure 1-1 Three steps of IGART

1.1.4 Imaging techniques used in IGRT and adaptive radiation therapy

1.1.4.1 Ultrasound

Ultrasound imaging utilizes acoustic waves to detect the anatomy of inside of the body. US probes are employed to send and receive acoustic waves. Portion of the acoustic waves reflects back to the probe when physical properties of tissues change inside the scanned volume. Therefore the interface between difference tissues can be detected and recorded using US. The scanned volumes can be reconstructed by analyzing the amplitude and timing difference between reflections and image of the scanned volume can be reconstructed. Ultrasound imaging can provide nonionizing, volumetric imaging with better soft-tissue contrast[8] than ionizing modalities such as CT and CBCT for different anatomical sites (e.g., prostate and liver). The limitation of US is its low image quality and image formation is user dependent [9].

1.1.4.2 In-room CT

In-room CT is an ionizing imaging modality to verify the patient setup and tumor localization. In-room CT is often a CT-on-rail system inside a linear accelerator (LINAC) room [10], as shown in Figure 1-2. The LINAC and free-standing CT share the same couch. The free-standing CT can be moved in the treatment room for different applications. Different Vendors have constructed their own in-room CT systems. The EXaCT system integrated a CT scanner from GE healthcare with 21EX accelerator from Varians [11]. AIRO Mobile Intraoperative CT from Mobius Imaging LLC can also be used for setup [12].

Before the treatment, patients are positioned on the couch with treatment setup and the CT scanner is mounted on rails to acquire patient anatomy using CT rotation. In-room CT can obtain the 3D volumetric patient images for patient setup evaluation and tumor localization.

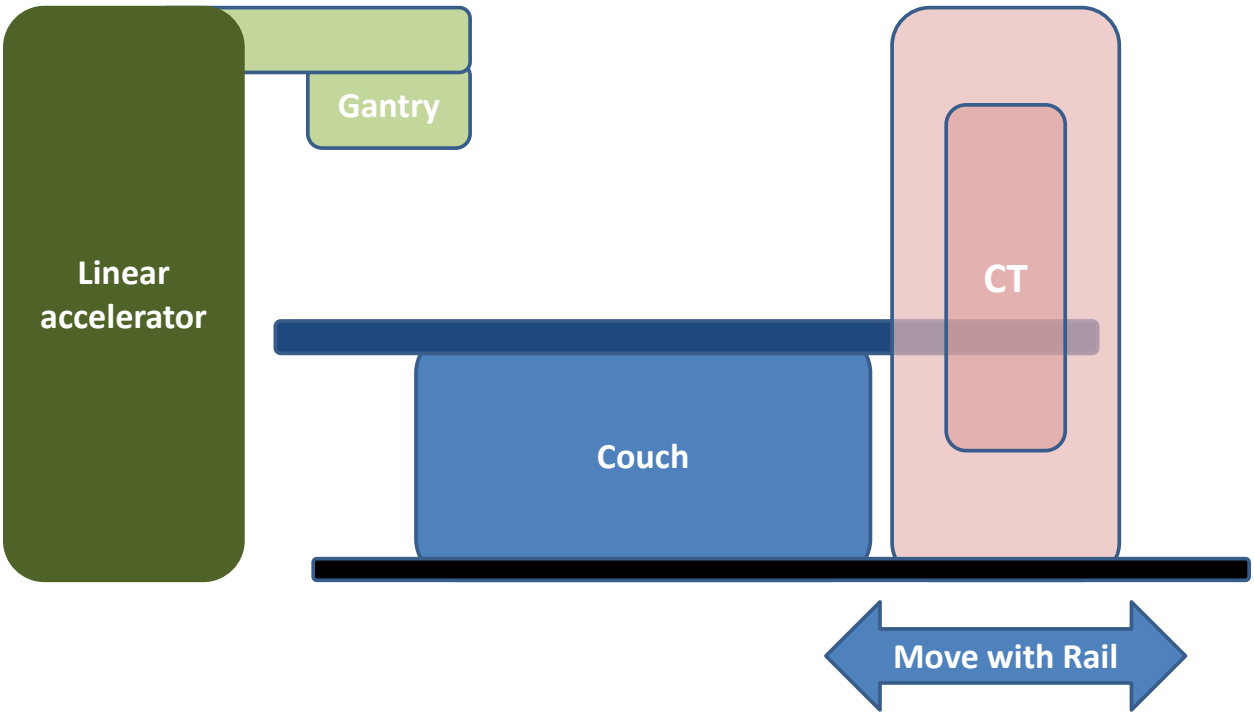

Figure 1-2 In-room CT system

The dark green denotes the linear accelerator and the light green is the gantry. The dark blue and light blue denotes the couch and the red part on the right is the free-standing CT which can move with the black rail

1.1.4.3 Two dimension radiographic Imaging

Two-dimensional (2D) radiographic (projection) imaging is used prior to the beam delivery in treatment rooms to assist the alignment for treatment [13]. A treatment unit with radiographic imaging is shown in Figure 1-3.

Megavoltage (MV) electronic portal imaging (EPI) is the most widely used type of radiographic imaging for patient setup before the introduction of Kilovoltage (KV) imager and detector to LINAC [14]. Megavoltage EPI uses the LINAC treatment head to deliver X-rays for imaging, which generate the X-ray beams for therapy. Therefore, it can provide the patient setup verification from beam's eye view. However, images acquired with high-energy X-rays will provide poor image quality with low contrast. Kilovoltage (KV) imaging can provide diagnostic-like image quality. KV X-rays tubes and corresponding detectors are integrated to LINAC gantry, perpendicular to the treatment beam axis. With either kV or MV imaging, two orthogonal X-rays 2D projections are acquired to determine the correction to patient setup by matching to the reference digitally reconstructed radiographs (DRRs) obtained from planning CT. The advantages of two-dimension radiographic imaging are the short acquisition time relatively low imaging dose as compared to CT. However, it does not provide 3D anatomical structures required for adaptive radiation therapy.

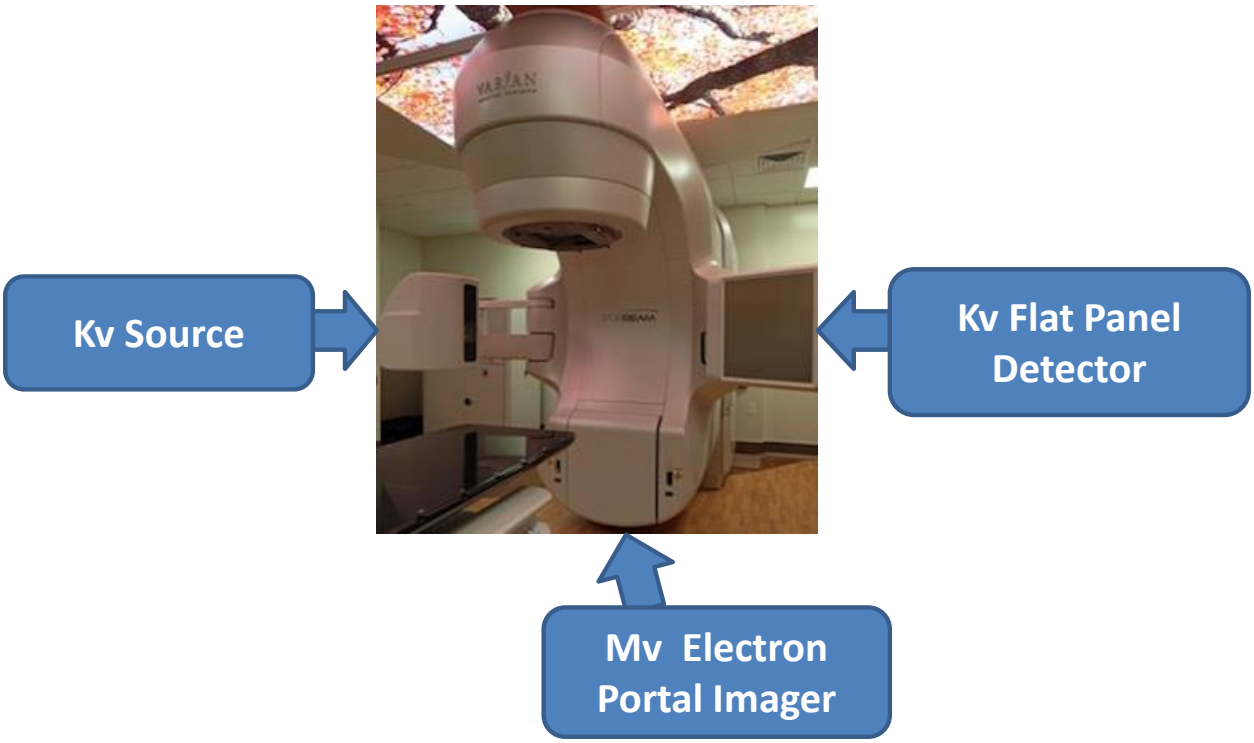

Figure 1-3 Treatment unit with integrated KV X-ray source and detector as well as MV EPI.

1.1.4.4 Cone beam CT

Cone beam CT images are acquired through X-ray imaging device integrated to linear accelerators [15, 16], as is shown in Figure 1-3. The KV CBCTs are acquired through KV cone-shaped X-ray tube and flat-panel detector, which are orthogonal to the treatment beam. CBCTs acquire multiple 2D projections (radiographic images) before beam delivery through rotating the gantry. The acquisition time is about 1-2 minutes. Standard cone-beam CT employs a filtered back-projection algorithm to reconstruct a 3D volumetric image [17] with high spatial resolution and sufficient soft tissue contrast to be compared with the planning CT as reference for patient setup correction and tumor localization [18]. MV CBCT utilizes the therapy beam and flat panel detector for electronic portal imaging (EPI) to rapidly acquire multiple, low-dose 2D projection images.

These projections are then used to reconstruct the 3D volumetric dataset that can be compared with the planning CT.

MV and KV CBCT have their own advantages. MV CBCT provides superior characteristics including high-z artifact suppression and direct dose calculation without attenuation coefficient extrapolation [19]. KV CBCT offer better image quality with better inherent physical contrast. The CBCT images patients at the same position as patients get treated, which minimizes the positioning uncertainty related to the imaging procedure.

To summarize, different imaging techniques used for patient setup and tumor localization before or during the treatment all have their own pros and cons and are suitable for different treatment sites. This dissertation mainly focuses on CBCT.

1.1.5 CBCT

1.1.5.1 CBCT geometry

The geometry of CBCT is shown in Figure 1-4(A). Compared with conventional fan beam CT (FDCT) shown in Figure 1-4 (B) that using a linear series of detectors and a collimator-restricted fan beam to scan several time to obtain a 2D projection, cone beam CT utilizes conical geometry with a cone-shape X-ray tube and a flat panel detector. Conventional FDCT acquired projections with both gantry rotation and Z-direction translation. For each rotation, filtered-back-projection (FBP) reconstruction method is used to reconstruct a CT image that only covers one or several slices in Z direction. In contrast, CBCT acquires multiple 2D projections containing entire volumetric dataset with a single rotation. The group of projections are utilized to reconstruct 3D

volumetric images using Feldkamp–Davis–Kress (FDK) algorithm [17]. Since CBCT acquires 2D projections, the coverage of field-of-view (FOV) is decided by the size of the flat panel detector. To enlarge the coverage of FOV in X and Y direction (cross-section), flat panel detector with an offset can be applied, known as half-fan scanning.

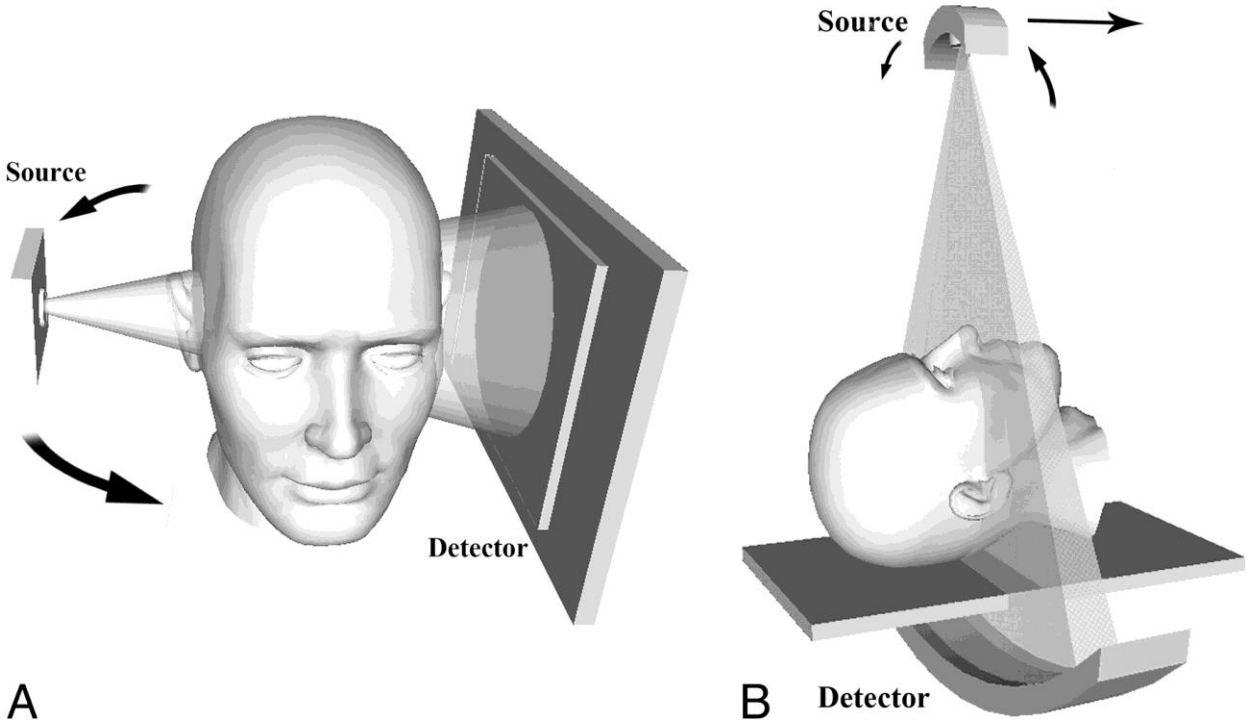

Figure 1-4 Geometry of Cone beam and Fan beam. A) Cone beam geometry. B) Fan beam geometry.

Figure Adapted from : Miracle, A. C., and S. K. Mukherji. "Conebeam CT of the head and neck, part 1: physical principles." American Journal of Neuroradiology 30.6 (2009): 1088-1095.

1.1.5.2 Flat-panel detector

The development of high-resolution flat panel detector boosted the application of CBCT in capturing cone-shaped X-ray beams to verify patient's setup. Amorphous-silicon (a-Si) flat panel imagers are utilized nowadays. The detector is composed of an array of detector unit. Each detector unit is composed of a cesium iodide (CsI) scintillator, a a-Si pin photodiodes and a thin

film transistor (TFT) gates [20]. The X-ray is converted to visible light after the scintillator layer [21, 22]. A-Si pin photodiodes generate and record electrical signals in proportion to the light received from scintillator layer. The electrical signal is read out using TFT switch row by row. The flat panel detector has been widely used in clinic for CBCT image acquisition. However, further investigation is expected to overcome problems such as image lag and suboptimal linearity to obtain better image quality, compared with fan beam CT.

1.2 FOUR DIMENSIONAL (4D) CBCT

1.2.1 KV 4D-CBCT

Cone beam CT has been used routinely in clinic for patient setup correction and has become a powerful tool for image guided radiation therapy. Due to the limitation of gantry rotation speed (according to the International Electric Commission recommendation), 60 seconds are required to finish one rotation of 360° to acquire ~700 projections. Therefore, each entire scan will contain projections from 10-20 respiration cycles. In the thoracoabdominal region, organs such as lung and liver are influenced by the respiration motion. The inconsistency of the patient geometric anatomy of different respiration phase induces inconsistency of corresponding projections. The inconsistency of projections results in motion artifacts within the field of view in the reconstructed images using static reconstruction methods. Four dimensional (4D)-CBCT binned projections into different groups according to the respiration phase [23]. For each phase, one 3D volumetric image is reconstructed individually. A series of volumetric images from different respiratory phase can illustrate the dynamic changes of patient anatomy.

In 4D-CBCT, after the phase sorting, the number of projections within each phase substantially decreased. Strong streak artifacts due to insufficient sampling will degrade 4D-CBCT image quality. Therefore, more projections are required for 4D-CBCT compared with 3D-CBCT. There are two methods to acquire more projections, slow the gantry speed or multiple gantry rotations[24]. However, acquiring more projections means longer acquisition time and higher imaging dose which limited the clinical application.

Advanced reconstruction methods are desired to reduce the acquisition time while maintaining the 4D-CBCT image qualities to achieve obtaining high quality 4D-CBCT image with 3D-CBCT projections.

1.2.2 Importance of 4D-CBCT

1.2.2.1 Four dimensional image guided radiation therapy

Tumor control probability and normal tissue complication probability are closely related to dose received[25, 26]. Therefore, it is critical to define the tumor volume and to increase the accuracy of tumor localization. Respiration induced motion of tumor and surround organs-at-risks are the principal cause of uncertainties in radiation therapy in the thoracoabdominal region [27], whose influence involves in at all steps of the radiation therapy procedure: target definition, margin selection, patient set-up, treatment delivery and dose calculation. Respiration correlated CT (4D-CT) imaging has been widely used clinically to remove motion artifacts and perform motion management for precise tumor volume delineation and margins assessment based on tumor motion range [28].

1.2.2.2 Rationale for application of 4D-CBCT in IGART

Patient set-up and treatment delivery also require high precision of patient positioning and tumor localization. Cone beam CT can provide on-board image before treatment for IGART to adapt the treatment to the anatomy-on-treatment-day. The difference in patient anatomy between planning CT and on-board CBCT decides the following modification of treatment. Patients' geometric anatomy changes can be categorized into intra-fractional variations and inter-fractional variations arising from respiration, tumor regression or growth, and other pathologic changes. These two types of difference contribute differently to the total tumor localization uncertainty depending on the disease sites. For example, adaptive radiation therapy for lung cancer concerns more about addressing intra-fractional motion to better locate the tumor and determine the target volume, but less on inter-fractional motion [29, 30]. As for prostate, inter-fractional anatomic change obtained more attention due to the significant shape and volume change for tumor and surrounding OARs such as bladder and rectum [31].

In the thoracoabdominal region, intra-fraction anatomy variation resulting from respiration motion is the primary cause for tumor localization uncertainty. Population-based margins are added to the tumor including large volume of normal tissue adjacent to the tumor. 4D-CBCT can aid to quantify the intra-fraction motion range. Locations of tumor in each phase are integrated to obtain a patient-specific tumor motion range. Patient-specific planning target volume (PTV) margin is desired to find appropriate volume for irradiation to improve dose escalation and reduce radiation toxicity to achieve better tumor control and normal tissue complication [30].

1.2.3 4D-CBCT Reconstruction

4D-CBCT image quality directly decides the tumor localization accuracy. Researches have been conducted on this topic to obtain high quality 4D-CBCT. Those methods can be summarized into 2 categories: individual-phase reconstruction and motion-compensated reconstruction.

1.2.3.1 Individual-phase reconstruction

Individual-phase reconstruction methods reconstruct CBCT volumes mainly with the sorted projections assigned to the current phase. Conventional analytical Feldkamp–Davis–Kress (FDK) reconstruction algorithm[16] , which is widely used in the clinic for CBCT reconstruction, generates images with severe streak artifacts from under-sampled projections. The principal problem for 4D-CBCT reconstruction is the streak artifacts caused by insufficient number of projections in each phase after the phase binning.

Iteratively reconstruction methods such as algebraic reconstruction (ART) algorithm [32] and the simultaneous algebraic reconstruction (SART) algorithm [33] cannot overcome the streak artifacts problem either. Those methods do not include any priori knowledge for CBCT reconstruction. Advanced iterative reconstruction embraces priori knowledge during the reconstruction process to reduce or remove streak artifacts and improve reconstructed 4D-CBCT image quality. These algorithms solve the reconstruction problem by iteratively matching the forward projections of the reconstructed image to the actually acquired projections. In addition to data fidelity, these techniques usually add sparsifying transformations, such as total variation minimization [34-36] and nonlocal mean regularization [37] in the objective function to optimize

the reconstructed image. With the introduction of priori knowledge to the reconstructed images, these iterative methods can greatly improve image quality as compared to FDK reconstruction. However, when the projection number is small for each phase, the reconstructed images suffer from over-smoothing and intricate structures are erased in the FOV, since the phase-correlated reconstruction methods reconstruct each respiratory phase independently. The convergence of those advanced iterative reconstruction methods which require regularizations are sensitive to parameters requiring multiple manual tuning to obtain the best results.

1.2.3.2 Motion-compensated reconstruction

In addition to the use of projections within a single phase, the correlations between different respiratory phases can be extracted and applied to improve the 4D-CBCT reconstruction quality [38]. Motion-compensated (MC) CBCT reconstruction algorithms have been investigated to reconstruct a single motion-suppressed reference phase image using projections from all phases integrated by an inter-phase motion model [39-41]. The image quality of motion-suppressed reference phase, reconstructed using the combination of projections in every phase, is much better than images reconstructed using projections from a single phase alone. Additional information, known as the inter-phase motion model, in the form of deformation vector fields (DVFs), is required in the process of MC CBCT reconstruction.

The inter-phase motion model can be generated by registering between the low-quality CBCT images reconstructed using projections from each single phase. Due to limited number of projection available for each phase, artifacts existed in low quality of reconstructed CBCT images degrades the accuracy of estimated motion model [40]. Other methods requires prior deformation

vector fields generated from prior 4D-CT images to combine projections from all phases [39]. These methods can perform well under the circumstance that respiration patterns of 4D-CT and 4D-CBCT remains the same. On the one hand, when the geometric anatomy and motion pattern changes between 4D-CT acquisition and 4D-CBCT acquisition, the induced inaccuracies in the estimated deformations can, in contrast, degrade the image quality of reconstructed motion-suppressed reference phase [39-42]. Furthermore, prior 4D-CT image set is not always available for each patient.

1.2.4 Motion model estimation

The accuracy of inter phase motion model largely determined the image quality of reconstructed reference phase image. Given that sever artifacts often present in individual phase CBCT reconstructed by conventional algorithms, many methods have been investigated to obtain inter-phase motion model from cone beam CT projections. Below is the summary of different categories of inter-phase motion model generation, including 3D-3D registration, 2D-3D registration, biomechanical modeling and convolutional neural network based methods.

1.2.4.1 Demons Method

Demons method is a deformable registration method proposed by Thirion [43] to achieve image-to-image matching to generate the inter-phase motion models. This is termed as 3D-3D registration because the registration occurs between two 3D volumetric CBCT images.

Demons deformable registration method is a greyscale image-based method which achieves images matching based on voxels intensity alone. The demons algorithm determines the forces to deform the 'moving' image into a static scene image based on the gradient information given from static scene image. The demons forces are estimated using optical flow equation. The displacement of moving image can be calculated as described in Equation 1-1.

$$\vec{u} = \frac{(m-s)\vec{\nabla}s}{|\vec{\nabla}s|^2+(m-s)^2} \quad \textbf{1-1}$$

$\vec{u}$ denotes the displacement shift. m denotes the moving image while s denotes the static scene image. The $\vec{\nabla}s$ denotes the gradient of static scene image. Equation 1-1 is working as an iterative approach. In each iteration, the optical flow computation is regularized by the smoothness of the deformation field.

Demons algorithm is a mature and simple deformable registration method. This method has been widely employed in motion-compensated CBCT reconstruction for inter-phase motion model estimation [38, 44-47] due to the linear computational complexity.

1.2.4.2 2D-3D registration

3D-3D registration methods perform registration between two 3D volumetric images. The accuracy of inter-phase motion model entirely depends on the images quality. For 4D-CBCT, phase image reconstructed using projections from the corresponding single phase suffered from heavy under-sampling artifacts. Therefore, the accuracy of inter-phase motion model generated using 3D-3D deformable registration method is degraded and further decreases the accuracy of reconstructed image through MC reconstruction. 2D–3D deformable registration can be applied to

update the DVFs between the reference phase and all the other phases [46, 48]. 2D-3D deformable registration is an intensity-matching based method. Different from 3D-3D registration method, the intensity-matching occurs in the projection domain. The forward projections of deformed images from reference phase using deformation vector field are compared with projections acquired from LINAC. This method gets rid of the influence of artifacts caused by the reconstruction algorithm. The method is called as 2D-3D registration because the 3D volumetric images are projected into 2D digitally reconstructed radiography to be matched with scanned 2D CBCT projection.

1.2.4.3 Biomechanical modeling

Biomechanical modeling is a commonly used method for deformation vector field estimation. As a part of biomechanical modeling, finite element modeling (FEM) has been employed for deformable registration of multiple organs such as lung [49-52], prostate [52, 53], liver [54-58] , heart [59] and brain [60] to predict the 3D displacement of anatomy between different time-points. Biomechanical modeling is a physic-driven method based on the continuum mechanics theory, aiming at predicting soft tissue deformation that has the advantage of providing physically realistic solutions[61]. The description of elastic properties of soft tissue is formulated using strain energy density function. To apply biomechanical modeling, the tetrahedral mesh is generated based on the segmentation of the organ to perform registration. Finite element analysis based biomechanical modeling requires boundary condition to derive the inside-soft-tissue motion model. Voxel-based displacement defined in the organ boundary region serves as the boundary condition. Once the boundary condition is defined, nodes of tetrahedral mesh start to move towards to a given position, pushed by the displacement.

1.2.4.4 Convolutional neural network

CNN can be regarded as foundation of modern computer vision. CNNs can be historical roots traced back to the 1980s, when the neocognitron was proposed by Kunihiko Fukushima [62]. Later in 1990, LeNet proposed by LeCun et al. became a pioneering work in CNN, aiming at recognizing handwritten digits. It succeeded in recognizing and classifying the visualized pattern directly from the input image. Later in 2012, Krizhevsky‘s work about using a AlexNet to do classification, which substantially decreased the error rate on ILSVRC competition, which is another milestone in the field of computer vision [63]. Various variations of AlexNet structures have been proposed which makes AlexNet the most fundamental and influential work in computer vision field.

The success achieved in the field of computer vision has attracted attention from other fields. The application of CNN has been extended to radiation therapy field to solve imaging and treatment related problems. For example, deep learning techniques have been widely explored for medical image registration due to their ability to automatically learn to combine the information of various complexities embedded in images for specific task implementation. Both supervised and unsupervised learning have been investigated to achieve medical image registration with advanced network structures such as fully convolutional network[64], reinforce learning[65], AlexNet [63] and generative adversarial network (GAN)[66].

However, image registration methods performed in the image domain are not suitable for motion-compensated reconstruction as high-accuracy inter-phase deformation vector fields are required for motion-compensated reconstruction. As mentioned in the Demons registration section,

the quality of image reconstructed using single phase projections are poor, inducing the poor quality of deformation vector field using image-domain registration. Nevertheless, we can improve the quality of DVF from a low-quality DVF through a model storing the relationship between the low quality DVFs and high quality DVFs using CNN.

1.3 4D-CBCT APPLICATION IN IGART

1.3.1 Patient setup

CBCT acquisition prior to treatment has been routinely used a clinically for patient setup. The first step of patient setup is aligning a patient to the room lasers. For respiration-involved sites, a 4D-CBCT can be acquired with the KV CBCT imager mounted to LINAC gantry. There is no generalized protocol using 4D-CBCT for patient setup. One method using a reconstructed Mid-ventilation CT for target definition and treatment planning [67]. Under this situation, for patient setup, each phase of 4D-CBCT was rigidly registered to Mid-ventilation CT through bony matching based on self-defined ROI containing vertebrae to correct patient setup residual errors. A ROI in Mid-ventilation CT containing tumor was register to each phase of 4D-CBCT to obtain the location of tumor in each phase. The mean tumor location over 4D-CBCT phases was compared with tumor location in Mid-ventilation image to obtain tumor base-line shift. The base-line shift was corrected through couch shift.

Other methods are also available for target delineation and tumor localization in patient setup using 4D-CT and 4D-CBCT. The tumor locations in each 4D-CT phase image can combine together to form the maximum intensity projection (MIP) including volumes that the tumor

occupied through the whole respiration cycle [68, 69]. Target delineation was performed by adding a margin to internal target volume (ITV) in the form of MIP. An isotropic 5 mm margin was added to the ITV. For patient setup, the tumor on 3D-CBCT reconstructed image is aligned to the tumor average intensity projection (AIP) of 4D-CT to correct the patient setup error.

1.3.2 4D dose calculation

For lung SBRT, in UTSW clinical practice, a second CBCT is acquired before the last beam delivery of each fraction. This CBCT is to verify the patient anatomy during delivery. Dose calculation based on the second 4D-CBCT presents the dose distribution under current anatomy which can be used to calculate the actual dose delivered to patients. The second CBCT can also be used to evaluate the dosmetric influence brought by intra-fraction motion which can be quantified by comparing the accumulated dose based on 4D-CBCT.

2 CHAPTER TWO
A biomechanical modeling-guided simultaneous motion estimation and image reconstruction technique (SMEIR-Bio) for 4D-CBCT reconstruction

2.1 INTRODUCTION

Linear accelerator-integrated cone-beam computed tomography (CBCT) has become a clinical routine for acquiring high resolution 3D volumetric anatomical images for image-guided radiation therapy (IGRT). However, respiratory motion induced motion artifacts such as blurring, streaking, and distortion, will highly degrade the image quality of 3D-CBCT volumetric image and further affects the application of CBCT in IGRT. Respiratory correlated CBCT [23], also called four-dimensional (4D)-CBCT, has been developed to acquire phase-resolved volumetric images to reduce respiration induced motion artifacts. Projections of 4D-CBCT are binned into different respiratory phases and projections acquired in the same phase from each respiratory cycle are used to reconstruct a phase image. These phase-sorted projections decrease the geometry inconsistency within each phase and contain minimal intra-phase motion, which substantially removes the motion artifacts from the reconstructed image. Subsequently, a series of phase-resolved 3D volumetric images can be stacked to obtain the anatomical structures' motion trajectory through the entire respiratory cycle.

Using sorted traditional 3D-CBCT scan projections to reconstruct a high-quality 4D-CBCT image would achieve a short scanning time and low imaging dose. However, this leads to under-sampling of each phase. Therefore, image reconstructed using projections from a single phase by conventional FDK method always suffers from severe streak artifacts due to lack of information. Recently, we developed a simultaneous motion estimation and image reconstruction (SMEIR) technique for 4D-CBCT reconstruction [46]. SMEIR uses an inter-phase motion model to combine

projections of all phases to reconstruct a reference phase image. The inter-phase motion is represented as deformation vector fields (DVFs) between the reference phase image and all other phase images. Specifically, SMEIR is composed of two steps: the motion-compensated reconstruction step and the motion estimation step. The first step uses a motion-compensated simultaneous algebraic reconstruction technique (MC-SART) to reconstruct a reference image using projections of all phases and the inter-phase DVFs [46]. The motion estimation step uses inverse consistent 2D–3D deformable registration to update the DVFs between the reference phase and the other phases [46, 48]. The DVFs are iteratively updated during the SMEIR optimization, so their qualities and accuracies continuously improve without being constrained by the initial quality of the reconstructed CBCT phase images. However, 2D–3D deformation updates the DVFs based solely on image intensity matching. These DVFs achieve high accuracy at lung boundary regions, but they suffer from limited accuracy in regions which contain small fine details. Accordingly, the accuracy of reconstructed CBCT images at these regions is limited.

This study developed a biomechanical modeling-guided SMEIR technique (SMEIR-Bio) to improve motion model accuracy in regions with small fine details whose reconstruction quality is degraded by limited projections at each phase. Biomechanical modeling has been proposed recently to solve deformation problems based on tissue composition and their corresponding elasticity properties, rather than on image intensity matching [49-52, 70-75].Therefore, biomechanical modeling can improve motion accuracy in regions with limited intensity variations. By applying appropriate boundary conditions, computational mechanical models enable the derivation of physiological and physical organ behaviors in the form of intra-organ deformation vector fields (DVFs) by finite element analysis (FEA). Therefore, the DVFs generated by SMEIR-Bio, combined with biomechanical modeling, can be more biomechanically realistic and accurate

in region ns with small, fine structures, which can also boost the accuracy of reconstructed 4D-CBCT images. We evaluated this method with 4D-CT data from 11 lung cancer patients. 4D-CBCT projections simulated from the 4D-CT images and used them for reconstruction. We made quantitative comparisons between images reconstructed by different methods and evaluated the DVFs' accuracy. This method can offer detailed information inside lung with high accuracy which can offer high quality geometric anatomy and benefit for IGRT.

2.2 METHODS AND MATERIALS

2.2.1 Method

SMEIR-Bio is a reconstruction algorithm that iterates and alternates between motion-compensated reconstruction, intensity-driven motion estimation, and biomechanical modeling-guided motion fine-tuning. Detailed descriptions of each key component and the entire workflow follow below.

2.2.1.1 Motion-compensated reconstruction

In this study, deformation vector fields (DVFs), which deform volumetric images through trilinear interpolation, represent the motion model between different 4D-CBCT phases [46, 76]. Motion compensated reconstruction uses these DVFs to deform images of other phases into a single reference phase, effectively combining all projection information to resolve the under-sampling that results from phase-sorting. We selected the end-expiration phase (phase 0) as the

reference phase because of its relative stability[77]. We applied the motion-compensated simultaneous algebraic reconstruction technique (MC-SART), which combines projections from all respiratory phases, to reconstruct the reference phase image. This reference phase image can be deformed to other phases using the backward DVFs [46], as shown in Equation 2-1 and Equation 2-2:

$$\mu_j^{0,(k+1)} = \mu_j^{0,(k)} + \lambda \frac{\sum_{t,n} d_{jn}^{t\to 0} \sum_i \left[a_{in} \frac{p_i^t - \sum_n a_{in} \mu_n^{t,(k)}}{\sum_{n=1}^{J} a_{in}} \right]}{\sum_{t,n} d_{jn}^{t\to 0} \sum_i a_{in}} \quad \textbf{2-1}$$

$$\boldsymbol{\mu_n^{t,(k)} = \sum_j d_{jn}^{0\to t} \mu_j^{0,(k)}} \quad \textbf{2-2}$$

μ^0 denotes the voxel-wise attenuation coefficients of the CBCT volume at the reference phase 0. μ^t denotes the corresponding attenuation coefficients at phase t. j and n denote the voxel coordinates for μ^0 and μ^t, respectively. k denotes the iteration number. a_{in} represents the elements of the forward projection matrix along projection line i. p_i^t represents the projection integral value at corresponding pixel i for phase t. $d_{jn}^{t\to 0}$ denotes the elements of the voxel-wise forward deformation vector field from phase t to phase 0. $d_{jn}^{0\to t}$ denotes the elements of the voxel-wise backward deformation vector field from phase 0 to phase t in Equation 2-2.

In Equation 错误!未找到引用源。, the term $p_i^t - \sum_n a_{in} \mu_n^{t,(k)}$ calculates the mismatch between the actual acquired projection of phase t and the forward projection of the reconstructed image at phase t by ray-tracing [78]. Then, the projection-domain mismatch is back-projected into the 3D volumetric image domain. The deformation vector field $d_{jn}^{t\to 0}$ deforms the error image of phase t to add to the reference phase image for correction. For each phase image t, $d_{jn}^{t\to 0}$ applies

the deformation vector fields to deform the n th voxel at phase t onto the j th voxel at the reference phase. For each phase t, there may be more than one voxel that could be deformed to the jth voxel in the reference phase image. Therefore, a summation of n is required. By applying corresponding DVFs, information from all phases is combined to reconstruct and fine-tune the reference phase image. The reconstruction results depend on the accuracy of the inter-phase DVFs, which necessitates DVF optimization by motion estimation. The relaxation factor λ in Equation 2-1 is set to 1. The same value has been used in our previous publications [79, 80], which balances the speed of convergence and the reconstruction noise. The same λ value has been used throughout the SMEIR-Bio algorithm. The motion-compensated SART reconstruction is followed by total variation regularization of the image to reduce artifacts and noise. The TV minimization uses a standard gradient descent approach with 10 iterations in our study.

2.2.1.2 Motion estimation

For motion estimation, an inverse-consistent 2D-3D registration algorithm is applied to solve $d_{jn}^{t\to 0}$ and $d_{jn}^{0\to t}$ simultaneously. By minimizing the cost functions $f_1(D^{0\to t})$ and $f_2(D^{t\to 0})$, the DVFs can be solved. f_1 and f_2 are defined as below:

$$f_1(D^{0\to t}) = \|\boldsymbol{p}^t - A\boldsymbol{\mu}^0(\boldsymbol{x} + \boldsymbol{D}^{0\to t})\|_{l_2}^2 + \beta\phi(\boldsymbol{D}^{0\to t}) \quad \textbf{2-3}$$

$$f_2(D^{t\to 0}) = \|\boldsymbol{p}^0 - A\boldsymbol{\mu}^t(\boldsymbol{x} + \boldsymbol{D}^{t\to 0})\|_{l_2}^2 + \beta\phi(\boldsymbol{D}^{t\to 0}) \quad \textbf{2-4}$$

A denotes the projection system matrix. x denotes the coordinate grids of the volumetric image. $D^{t\to 0}$ denotes the forward DVF matrix, and $D^{0\to t}$ denotes the backward DVF matrix. $d_{jn}^{0\to t}$ in Equation 2-1 makes the element of $D^{0\to t}$, and $d_{jn}^{t\to 0}$ makes the element of $D^{t\to 0}$. The first term

on the right side of each equation denotes the data fidelity term, which measures the differences between the acquired projections and the computed projections of the deformed CBCT volume. The second term on the right side denotes an energy function that regularizes the smoothness of DVFs, which promotes faster and more stable convergence [80]. The parameter β is set to 0.05, a value applied in previous 2D-3D deformation studies [79-81].

D is a matrix of additive displacements. Each element of D denotes one deformation vector containing the displacement of voxel along x (lateral), y (sagittal) and z (caudal) directions between two phases. D can be decomposed into 3 matrices denoting displacement along these three spatial directions individually: D_x, D_y and D_z.

Based on D_x, D_y, and D_z, the relationship between two phase images (μ^0 and μ^t) can be described as following:

$$\mu^0(i,j,k) = \mu^t(i + D_x^{t\to 0}(i,j,k), j + D_y^{t\to 0}(i,j,k), k + D_z^{t\to 0}(i,j,k)) \quad \textbf{2-5}$$

The symbols i, j, k denote the voxel coordinates along the three spatial directions x, y and z.

We formulate the solution of the DVF motion model as an optimization problem to minimize the objective functions f_1 and f_2. The solution of the DVF is also subject to the inverse consistency constraint defined in Equation 2-6 and Equation 2-7.

$$D^{0\to t} \circ D^{t\to 0} = 0 = D^{t\to 0} \circ D^{0\to t} \quad \textbf{2-6}$$

$$D^{0\to t} \circ D^{t\to 0} = D^{0\to t}(x + D^{t\to 0}) + D^{t\to 0} \quad \textbf{2-7}$$

Equation 2-7 defines the composition scheme of forward and backward deformation fields, which should result in zero displacement (2-6). Equation 2-6 also ensures the inverse consistency

of the deformation, as the composition from either direction should result in zero displacement. Based on Equation 2-6, we can solve the forward or the backward deformation field using the available counterpart from either f_1 or f_2 minimization. The same DVF inversion scheme is applied in reference [82]. We applied a nonlinear conjugate gradient algorithm to minimize f_1 and f_2 alternately. The updated $D^{t\to 0}$ from minimizing f_2 is inverted and input into f_1 as the initial start to update $D^{0\to t}$. The updated $D^{0\to t}$ is inverted and subsequently fed back into f_2 to update $D^{t\to 0}$. In total, we apply 10 iterations to optimize $D^{t\to 0}$ and $D^{0\to t}$ in an interleaved fashion. More details on the non-linear conjugate gradient algorithm, together with the corresponding parameters, can be found in the pseudo codes provided in our previous publication [80].

The projection intensity matching-based data fidelity term in the objective function plays an essential role in optimizing the DVFs, as shown in Equation 2-3 and Equation 2-4. Accordingly, the solved DVFs will be accurate in high-contrast image regions with large intensity variations. However, the DVF accuracy will be limited in low-contrast image areas or areas with small fine structures, both of which suffer from insufficient intensity differences on 2D projections. For lung, the small fine anatomical details are submerged and smeared in 2D projections although they can be fairly easily visualized in appropriate lung windows in the 3D image. This is the reason why we consider the contrast inside of lung within a projection image is low. In the motion estimation step, we are trying to match the projections simulated from a deformed CBCT and actual measured projections (Equation 2-3 and Equation 2-4). As the contrast within lung is low on a projection image, this will limit the DVF estimation accuracy when we rely on projection intensity difference only. As a result, the reconstruction accuracy of these areas suffers from inaccurate DVFs in the corresponding regions.

2.2.1.3 Biomechanical modeling

To boost intra-lung DVF accuracy, we introduce biomechanical modeling into the SMEIR algorithm. Biomechanical modeling is a physics-driven deformation approach that can correct and fine-tune the deformation in regions with small fine details by using boundary conditions defined at high-contrast organ surfaces through finite element analysis. To perform this analysis, an organ mesh composed of finite elements must be constructed with a corresponding material model. In this study, we use the hyper-elastic Mooney-Rivlin material model to describe the lung. This model is often applied to biological tissues with large deformations [83, 84]. The strain energy density function of the Mooney-Rivlin model is shown in Equation 2-8:

$$W = c_{10}(I_1 - 3) + c_{01}(I_2 - 3) + \frac{1}{2} * k(J - 1)^2 \quad \textbf{2-8}$$

The first two terms on the right side of Equation 2-8 denote the strain energy needed to deform the shape without changing the volume. The third term on the right denotes the strain energy needed to change the volume without altering the shape. I_1 and I_2 are the first and second invariants, respectively, of the right Cauchy-Green deformation tensor. J is the volume ratio [85]. k represents the bulk modulus. c_{10} and c_{01} are coefficients that represent material elastic properties.

Note that the biomechanical modeling can be generally applied to all organs to improve their intra-DVF accuracy. In this study, we focus on modeling the lung for 4D-CBCT reconstruction. To apply biomechanical modeling, the lung is first segmented out from the reference phase image. The segmentation accuracy also affects the boundary condition extracted from the 2D-3D deformation. The lung boundary's high contrast makes it easy to segment by an

automatic segmentation technique. For other organs with less clear boundaries (such as the prostate or kidney), automatic segmentation accuracy might be limited, which may require manual correction or more advanced segmentation techniques [86-88]. In our work, auto-segmentation based on the "snake" [89] algorithm is used to generate lung segmentation.

Biomechanical modeling requires lung segmentation to build a tetrahedral mesh model. To evaluate the effects on SMEIR-Bio reconstruction by segmentation differences, we used the ITK-SNAP [90] software package to generate lung segmentations using different methods. There are 4 segmentation methods provided in the ITK-SNAP software, including thresholding, edge-attraction, clustering and classification. We used these 4 methods to generate 4 different lung segmentations and put them into the SMEIR-Bio workflow for image reconstruction. Specifically for this evaluation, we used the lung masks generated from the reference images reconstructed by the 1st iteration of SMEIR-Bio, and did not further update the lung mask during the optimization. Thus the lung masks also contained errors not corrected in the following iterations, which also served the purpose to evaluate how the segmentation errors might affect the reconstruction accuracy of SMEIR-Bio.

Based on this lung segmentation, a lung surface meshed with triangle elements is generated using the open-source Iso2Mesh package [91]. From the meshed lung surface, 3D tetrahedral elements are further generated to cover and model the full lung volume. The boundary condition, defined as the DVF at the lung mesh surface nodes, can thus be applied to solve intra-lung motion through finite element analysis and the Mooney-Rivlin energy density function. We used the open-source FEBio package in this study to solve the finite element analysis [92].

2.2.1.4 General workflow of SMEIR-Bio

Figure 2-1shows the general workflow of SMEIR-Bio. To estimate an initial motion model between the phase images, we use the total variation-regularized algebraic reconstruction technique (ART-TV) [81] to reconstruct a coarse 4D-CBCT set. Then, we perform demons registration [43] to obtain the initial deformation vector fields (DVFs) between the reconstructed reference phase (phase 0) image and all other phase images. We then input the initial DVFs, the coarse 4D-CBCT set, and the projections of all phases into the motion-compensation step to update the reference phase image. Based on the updated reference image, we perform motion estimation to update the inter-phase DVFs. Before biomechanical modeling, we automatically segment the lung volume out from the reference phase image to generate a tetrahedral mesh model and use the lung surface DVFs solved by motion estimation at each phase as the boundary condition for finite element analysis. We then input the biomechanically-corrected DVFs into a motion-compensated reconstruction step and assess the reconstruction results for convergence. If not converged, the reconstruction circles back to the motion estimation step, followed by biomechanical modeling and motion-compensated reconstruction until final convergence is achieved.

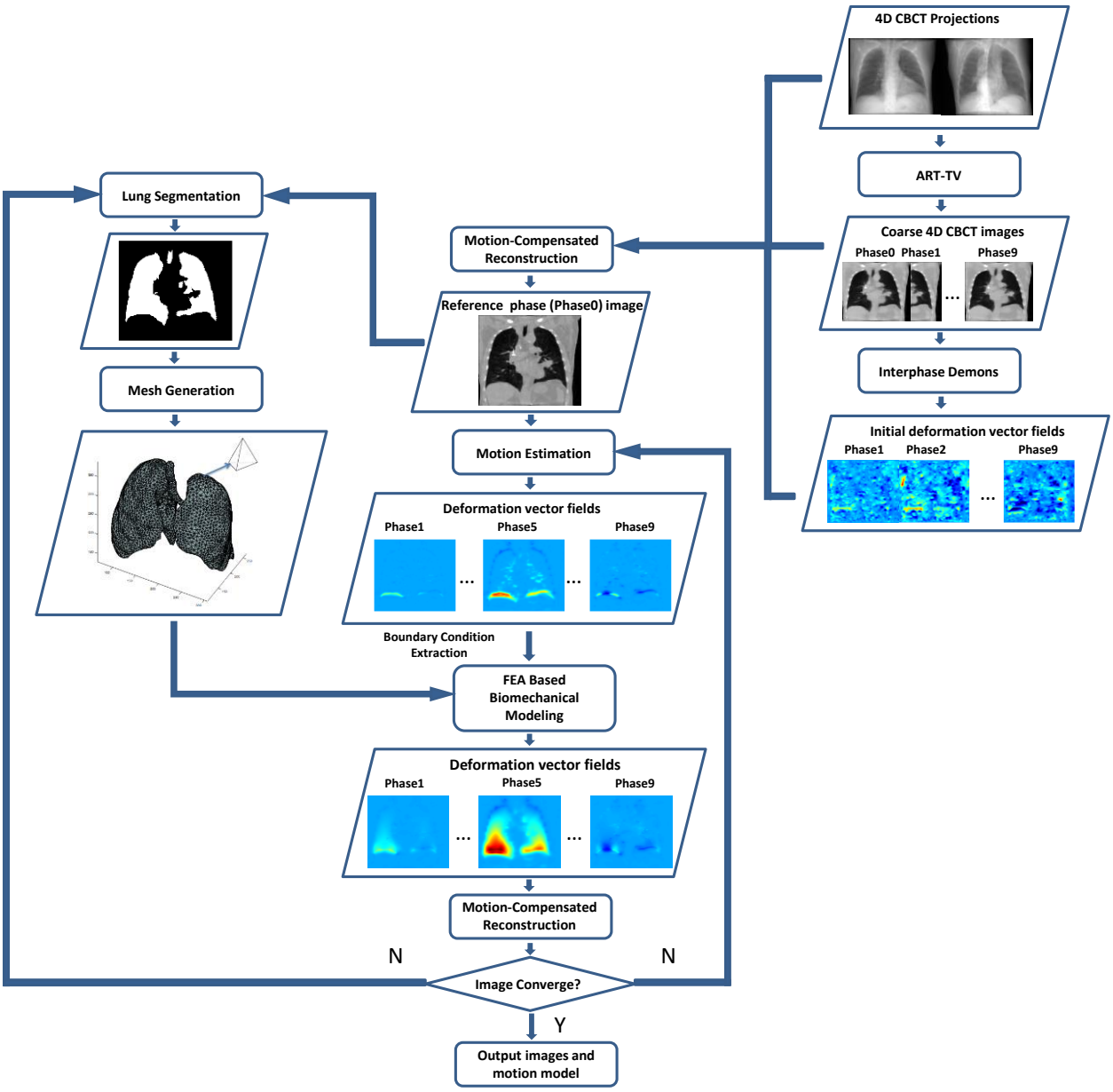

Figure 2-1 **Workflow of SMEIR-Bio**

2.2.2 Evaluation

2.2.2.1 Materials

We evaluated the performance of the SMEIR-Bio algorithm on 11 lung cancer patients. We simulated 4D cone-beam projections from a 4D-CT set of each patient for reconstruction. The image size is 256x256 for each patient and the slices number varies between different patients from 190 to 270. And the voxel size is 1.5 mm x 1.5 mm and the slice thickness is 2 mm. The respiratory rate is around 15 breathings per minute. For the simulation algorithm, we used the ray-tracing technique [78]. We did not add additional noise or scatter in the simulated projections, where only residue artifacts (noise, scatter, beam hardening) in the 4D-CT were considered. For each patient, we generated 4 groups of 4D-CBCT projections to simulate different acquisition sparseness, with 10, 20, 30, or 40 projections per phase. The 4D-CBCT projections were simulated from the 4D-CT images with 300 x 250 pixels in each projection. Each pixel measures 2 mm x 2 mm. The simulated source-to-axis distance is 1000 mm, and the source-to-imager distance is set at 1500 mm. Since the projections were simulated from each phase, the acquisition rate and respiration rate were irrelevant. The simulated projections of each phase are evenly distributed across a 360̊ scan angle. In total, 872 landmarks from all patients identified by expert radiation oncologists were used to verify motion model accuracy.

To further evaluate this method, we take real projections that contain scatter, noise and beam hardening into the consideration. The 4D-CBCT projections were scanned using a Varian Trilogy LINAC (Varian Medical Systems, Palo Alto, CA), with 120 kV peak voltage, and 80 mA/25 ms exposure for each projection. The distance between the x-ray source and the flat panel detector is 1500 mm while the source-to-isocenter distance is 1000 mm. The acquired angular range is [-265°, -75°].The scanning duration is 4.5 min and the average patient breathing cycle is 2.78 s. The 4D-CBCT set has 1982 projections in total, which has been sorted into 10 respiratory

phases. Each phase was reconstructed using the ART-TV algorithm and the reconstructed images were used as "gold-standard" reference image. The reconstructed image size is 200x200x100 and the image resolution is 2 mm. We then down-sampled the number of projections at each phase by a factor of 10 to around 20 and performed the SMEIR and SMEIR-Bio reconstructions separately based on the sparse projections.

2.2.2.2 Biomechanical parameter optimization

The specified elasticity parameters K, c_{10}, and c_{01}, represent the biomechanical features of the lung material, as shown in Equation 2-8. c_{10} and c_{01} denotes shear modulus and K denotes bulk modulus. The shear modulus determines the resistance of shape change and the bulk modulus determines the resistance of volume change. Their values will affect the solved intra-lung DVFs under the same boundary condition. The K, c_{10}, and c_{01} are related to Poisson's ratio (v_p) as shown in Equation 2-9:

$$\frac{K}{c_{10}+c_{01}} = \frac{4(1+v_p)}{3(1-2v_p)} \quad \textbf{2-9}$$

In this study, we set $c_{10} = c_{01} = c$ to simplify the problem. The relationship shown in Equation 2-9 can thus be represented as Equation 2-10:

$$\frac{K}{c} = \frac{8(1+v_p)}{3(1-2v_p)} \quad \textbf{2-10}$$

v_p is Poisson's ratio of material [93] defined as the ratio of lateral contraction to longitudinal extension when a bar is pulled out. It is a dimensionless parameter which is related to the compressibility of materials[94]. In the Mooney-Rivlin model, the ratio $\frac{K}{c}$ defined in Equation

2-10 describes the incompressibility of materials, or the k_factor, which is directly related to Poisson's ratio (v_p). Previous studies on lung modeling have used a range of Possion's ratios [70, 73, 75, 95, 96] Table 2-1.

Table 2-1 Previous studies on lung modeling.

The Poisson's ratio used in each study and the corresponding k_factor for the Mooney-Rivlin model are shown.

Previous Studies	Poisson's Ratio	k_factor
Lai-Fook S J *et al.* (ref. [95])	0.43	27
SH Sundaram, CC Feng (ref. [70])	0.45	40
Brock KK *et al.* (ref. [96])	0.45	40
A. Al-Mayah *et al.* (ref. [73])	0.4, 0.45, and 0.499	19, 40 and 2000
J Eom *et al.* (ref. [75])	0.4	19

We process a k_factor evaluation to find the appropriate k_factor used in the SMEIR-Bio reconstruction. As it is shown in Equation 2-10, the k_factor is calculated from material's Poisson's ratio and will increase with increasing Poisson's ratio. The isotropic lower limit of Poisson's ratio is -1 and the upper limit is 0.5[97]. The incompressibility of materials increases with Poisson's ratio. When Poisson's ratio reaches 0.5, it means the material is not compressible and the corresponding k_factor is infinite. Previous studies in Table 2-1 give a rough range to describe the Poisson's ratio of lung tissue from 0.4 (k_factor =19) to 0.499 (k_factor =1999). We extend this range to 0.4999. Therefore values of k_factor we chose to evaluate the k_factor are 20, 100, 200, 1000, 2000, 10000.

2.2.2.3 Quantitative image evaluation

For each projection group, we used the original 4D-CT images as the reference image (or "ground-truth") to evaluate the reconstructed images. We calculated different similarity metrics, including the relative error (RE) [98], the root-mean-square error (RMSE) [99], the normalized cross-correlation (NCC) [100], and the universal quality index (UQI) [101] to quantify the similarity between the reconstructed images and the reference images.

$$RE = \sqrt{\frac{\sum_N (A-B)^2}{\sum_N A^2}} \quad \textbf{2-11}$$

$$RMSE = \sqrt{\frac{\sum_N (A-B)^2}{N}} \quad \textbf{2-12}$$

$$NCC = \langle \frac{A}{\|A\|}, \frac{B}{\|B\|} \rangle \quad \textbf{2-13}$$

$$\boldsymbol{UQI = \frac{\sigma_{AB}}{\sigma_A \sigma_B} \cdot \frac{2\bar{a}\bar{b}}{(\bar{a})^2 + (\bar{b})^2} \cdot \frac{2\sigma_A \sigma_B}{{\sigma_A}^2 + {\sigma_B}^2}} \quad \textbf{2-14}$$

A denotes the reference image, and B denotes the reconstructed image. N denotes the total voxel numbers of A or B. $\bar{a}$ and $\bar{b}$ denote the averages of A and B, respectively. σ_A is the standard derivation of A, and σ_B is the standard derivation of B. σ_{AB} calculates the covariance between A and B.

We made quantitative comparisons between images reconstructed by SMEIR-Bio using different projection numbers to evaluate the method's performance under different sampling sparseness. We also performed quantitative comparisons between 4D-CBCT images reconstructed by ART-TV, SMEIR and SMEIR-Bio under the same sampling sparseness. We also used one method proposed in a previous work [102]. This method follows the work frame of SMEIR and uses mesh-based representation (in contrast to voxel-based representation) to update the DVFs without considering the elastic properties of tissue, which is referred to as the "SMesh" method in the following. In addition to image reconstruction accuracy, we also measured lung motion model

accuracy for each patient by comparing manually-tracked lung landmark motion with solved DVFs from different reconstruction methods. We tracked the lung landmarks displacement between the end-of-inspiration and end-of-expiration phases for evaluation, defining the displacement error $\vec{\boldsymbol{D}}_{error}$ as the difference vector between the manually-tracked landmark displacement and the corresponding displacement extracted from solved DVFs. We calculated and compared the averages and standard derivations of D_{error} under each projection group.

$$\vec{\boldsymbol{D}}_{error} = \vec{\boldsymbol{L}}_{manually} - \vec{\boldsymbol{L}}_{DVF} \quad \textbf{2-15}$$

$$D_{error} = \left\|\vec{\boldsymbol{D}}_{error}\right\| \quad \textbf{2-16}$$

$\vec{\boldsymbol{L}}_{manually}$ denotes the manually-tracked displacement vector composed of $l^{x}_{manually}$, $l^{y}_{manually}$, and $l^{z}_{manually}$, which denote motion along x (left-right), y (anterior-posterior), and z (superior-inferior) spatial directions, respectively. The $\vec{\boldsymbol{L}}_{DVF}$ denotes the displacement vector extracted from the solved DVFs, composed of l^{x}_{DVF}, l^{y}_{DVF}, and l^{z}_{DVF}. D_{error} denotes the norm-2 of the difference vector between $\vec{\boldsymbol{L}}_{manually}$ and $\vec{\boldsymbol{L}}_{DVF}$, or the length of the displacement error.

2.3 RESULTS

2.3.1 k_factor optimization

We evaluated the influence of different k_factor values by calculating the average $D^{SMEIR-Bio}_{error}$ of all landmarks. The corresponding results are shown in Figure 2-2 and Table 2-2. For patient 3, patient 7, and patient 11, the length of displacement errors (D_{error}) is the smallest when

the k_factor is equal to 1000 (Figure 2-2). For the others, the D_{error} gradually decreases with increasing k_factor values. Overall, a k_factor of 1000 generates the highest DVF accuracy in the parameterized study (Table 2-2). Thus, we used this value in the following evaluations.

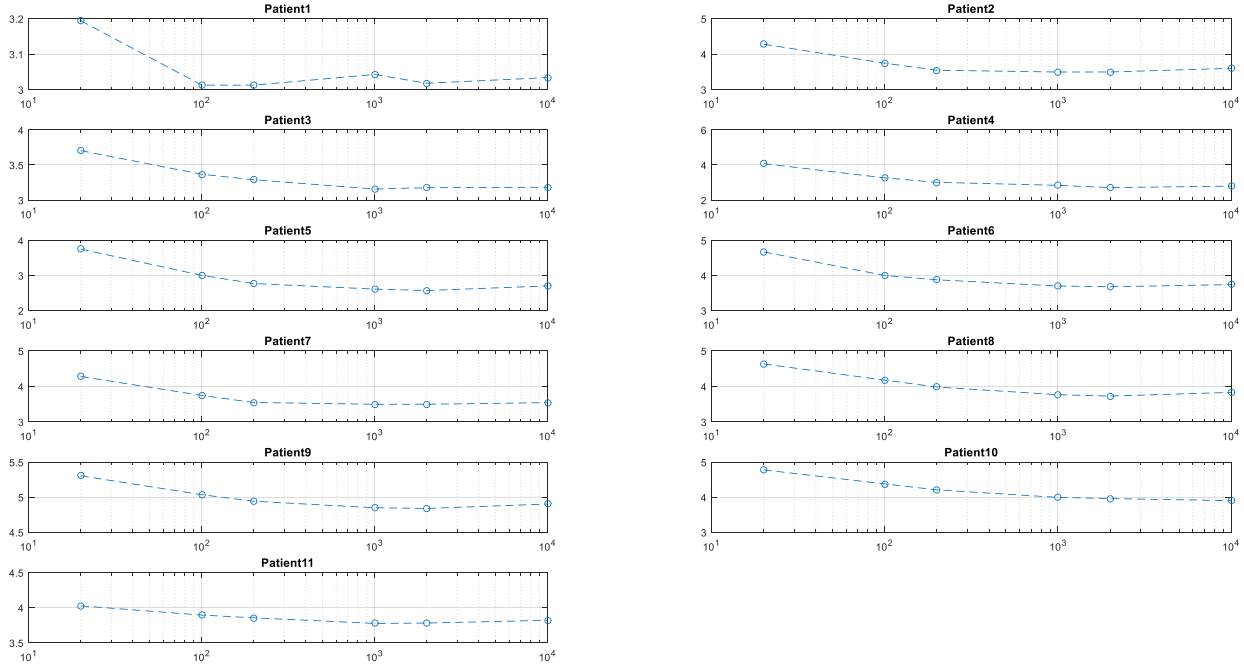

Figure 2-2 The average of all landmarks of D_error^(SMEIR-Bio) for each patient using different *k_factor* values.

Table 2-2 The average of all landmarks of D_error^(SMEIR-Bio) for all 11 patients using different k_factor values.

k_factor	20	100	200	1000	2000	10000
MEAN D_{error} (mm)	4.151 ± 0.659	3.719 ± 0.656	3.592 ± 0.656	3.460 ± 0.645	3.465 ± 0.646	3.539 ± 0.654

2.3.2 Reconstruction image quality

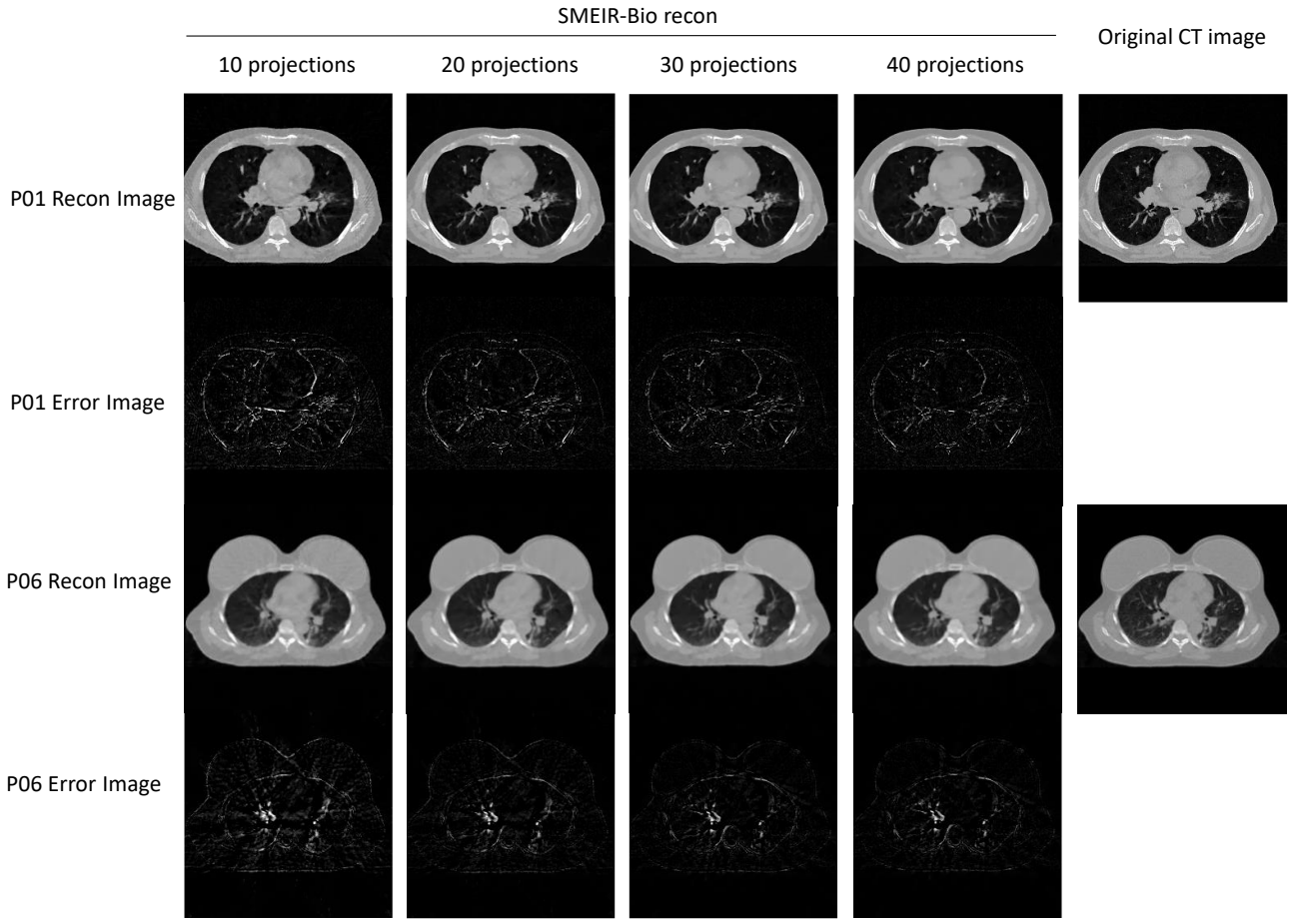

Figure 2-3 Comparison between the reference phase (phase 0) images reconstructed by SMEIR-Bio using different numbers of projections.

The left four columns show the reconstruction results using 10, 20, 30, and 40 projections, respectively. The rightmost column shows the same slice of the original CT image for comparison. The first row shows the reconstructed images with different projection number groups for patient 1, and the second row shows the difference image between the original CT image and the reconstructed images. The third row shows the reconstructed images with different projection number groups for patient 6, and the fourth row shows the difference image between the original CT image and the reconstructed images. The display window of the reconstructed images is [-1000, 635] HU, and the display window of the error images is [-1000 to -455] HU.

SMEIR-Bio method is evaluated using groups of different projection number. The difference between "ground-truth" and reconstructed images are made and shown in Figure 2-3. The difference is small, even when using 10 projections per phase for reconstruction. SMEIR-Bio method can achieve high quality image reconstruction even with small projection number. Using more projections helps to reduce the mismatches of the lung's fine structures.

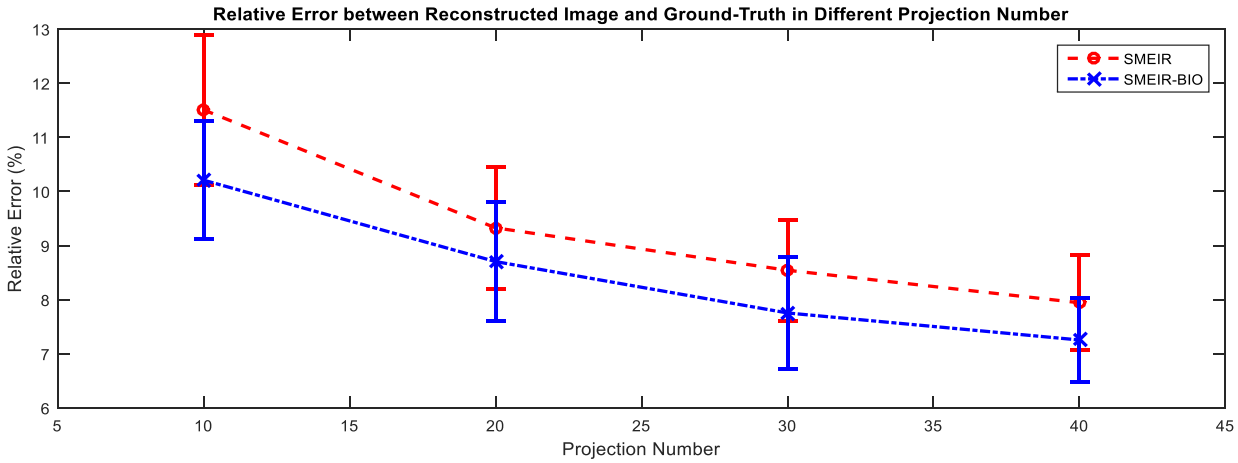

Figure 2-4 Average values with standard derivations for the relative error metric between reconstructed images and original "ground-truth" CT images (Phase 0) for all patients.

We calculated the relative error between the "ground-truth" and reconstructed images of each patient with different methods. The means and standard derivations of relative error of all patients for different projections are shown in Figure 2-4, for both SMEIR and SMEIR-Bio reconstructions. The relative error decreases with increasing projection number. Compared with SMEIR, SMEIR-Bio enables higher reconstruction accuracy with smaller relative errors.

To evaluate the performance of SMEIR-Bio in lung regions with small fine details, we performed quantitative comparisons on 10 intra-lung regions with fine pulmonary structures for all patients. 6 of the 10 selected regions of interest (ROIs) of patient 1 and patient 10 are shown in Figure 2-5. The SMEIR-Bio reconstructs fine lung details that better match the "ground-truth"

than the other two reconstruction techniques, in terms of both structure shape and intensity. Quantitative results of the comparison between ROIs demonstrate the superiority of SMEIR-Bio in reconstructing areas with small, fine details (Figure 2-6).

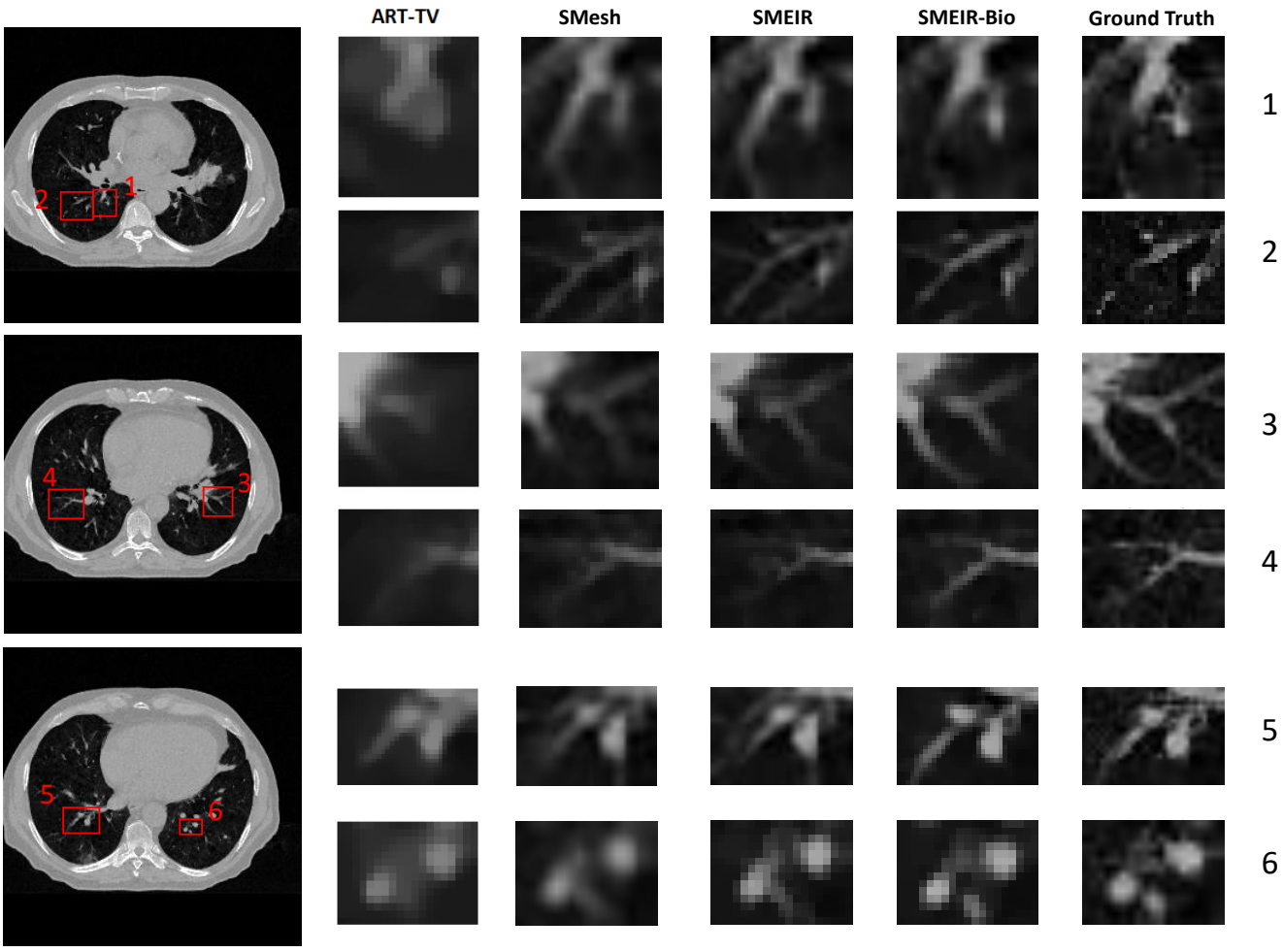

(A)

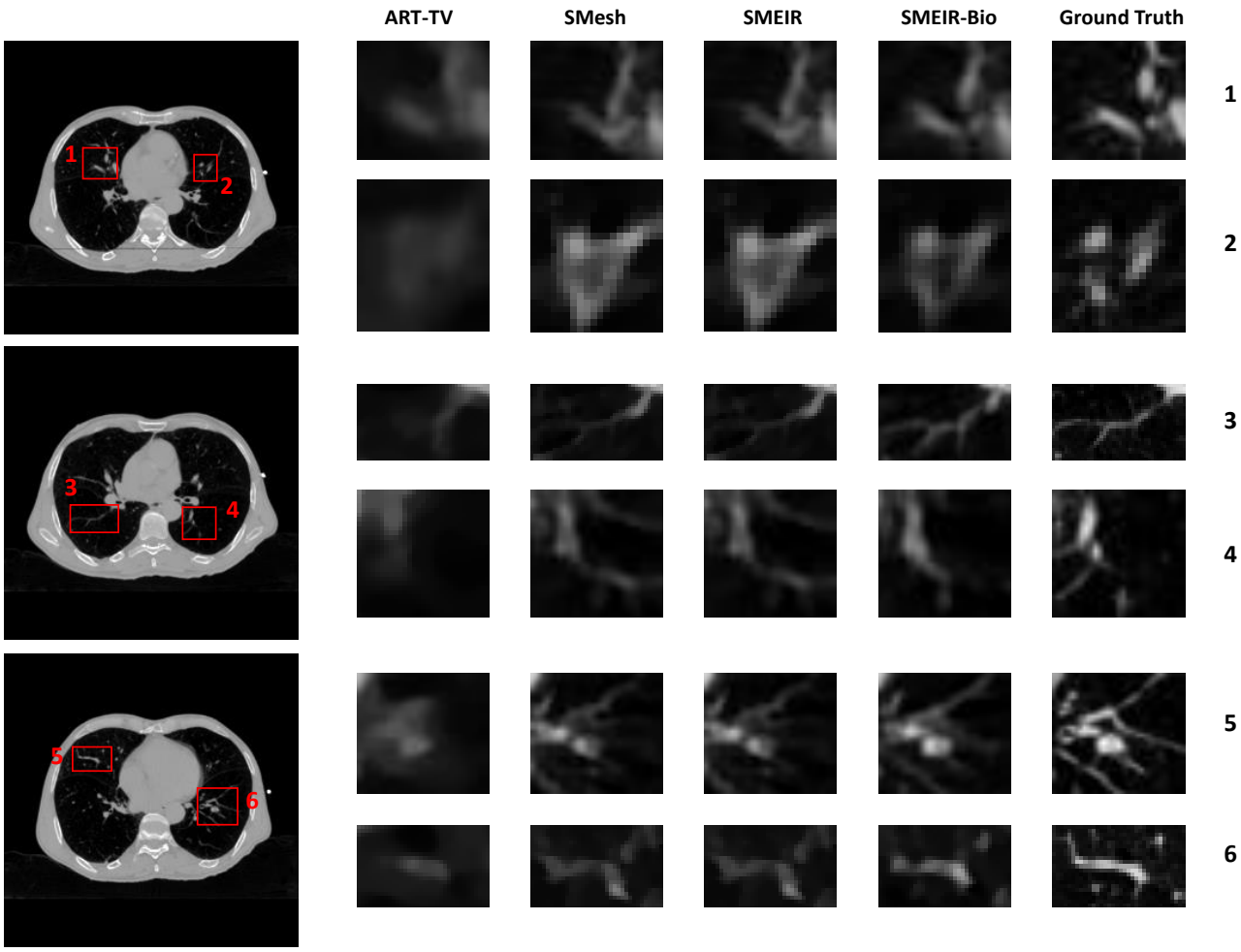

(B)

Figure 2-5 Extracted and zoomed details for 6 of the 10 regions of interest (ROIs) in the reference phase (phase 0) image of (A) patient 1, (B) patient 10.

The extracted ROIs are highlighted with red squares in each left-column slice. The four columns on the right display the same ROIs extracted from images reconstructed by ART-TV, SMesh, SMEIR, and SMEIR-Bio, reconstructed with 30 projections per phase, and from the original "ground-truth" CT image. The display window for all images is [-1000, 635] HU.

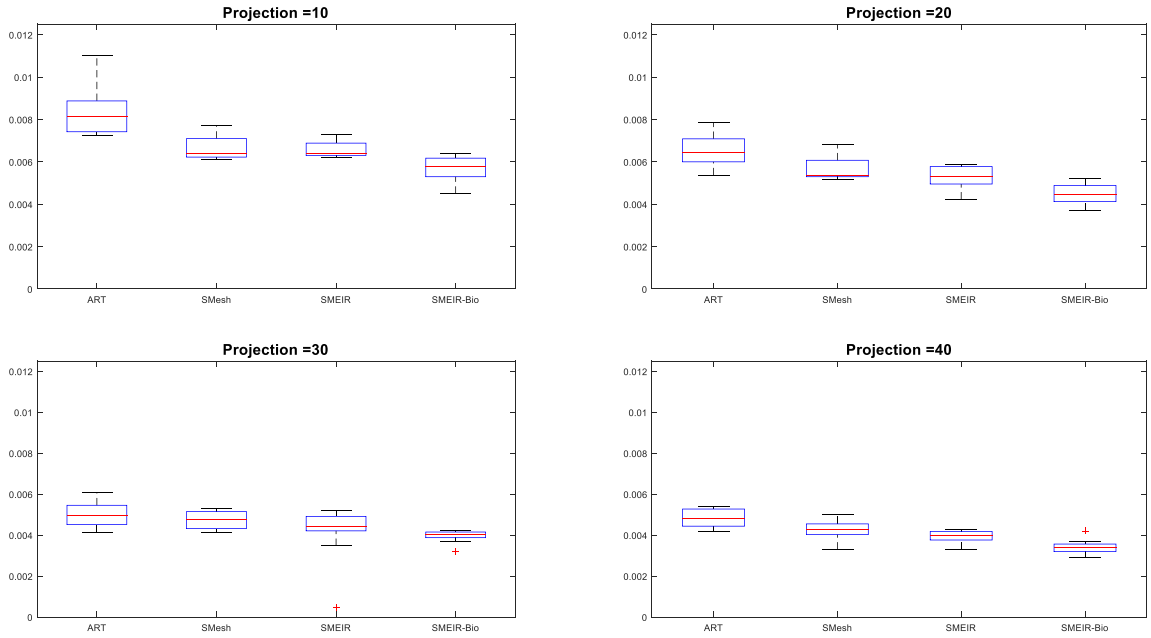
Projection =10
Projection =20
Projection =30
Projection =40
ART
SMesh
SMEIR
SMEIR-Bio

(A)

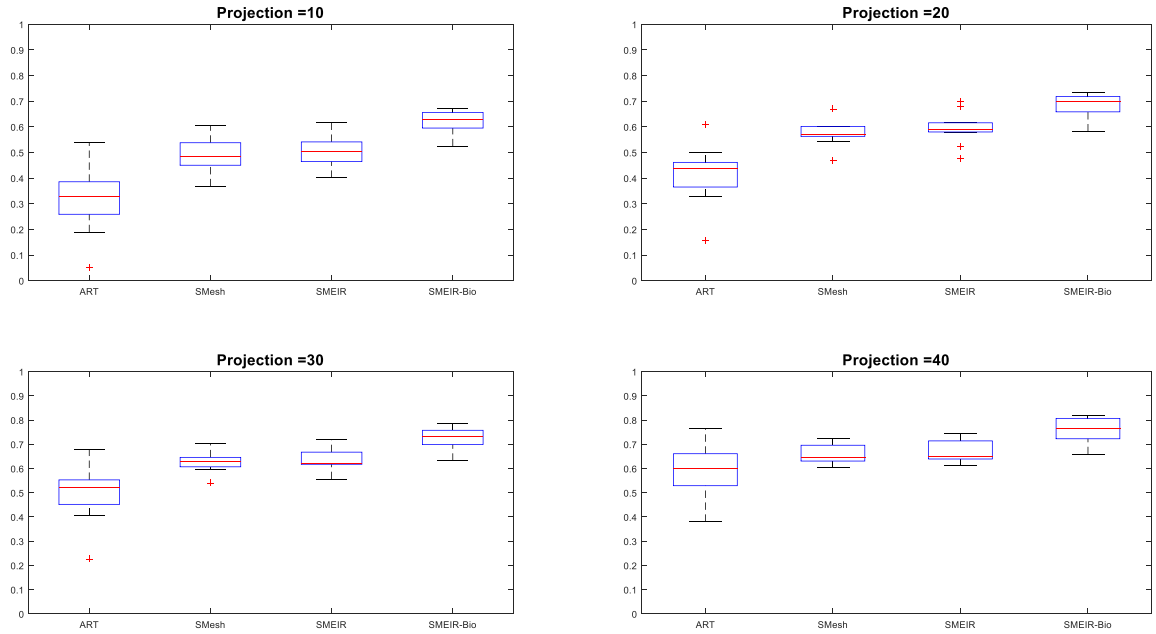
Projection =10
Projection =20
Projection =30
Projection =40
ART
SMesh
SMEIR
SMEIR-Bio

(B)

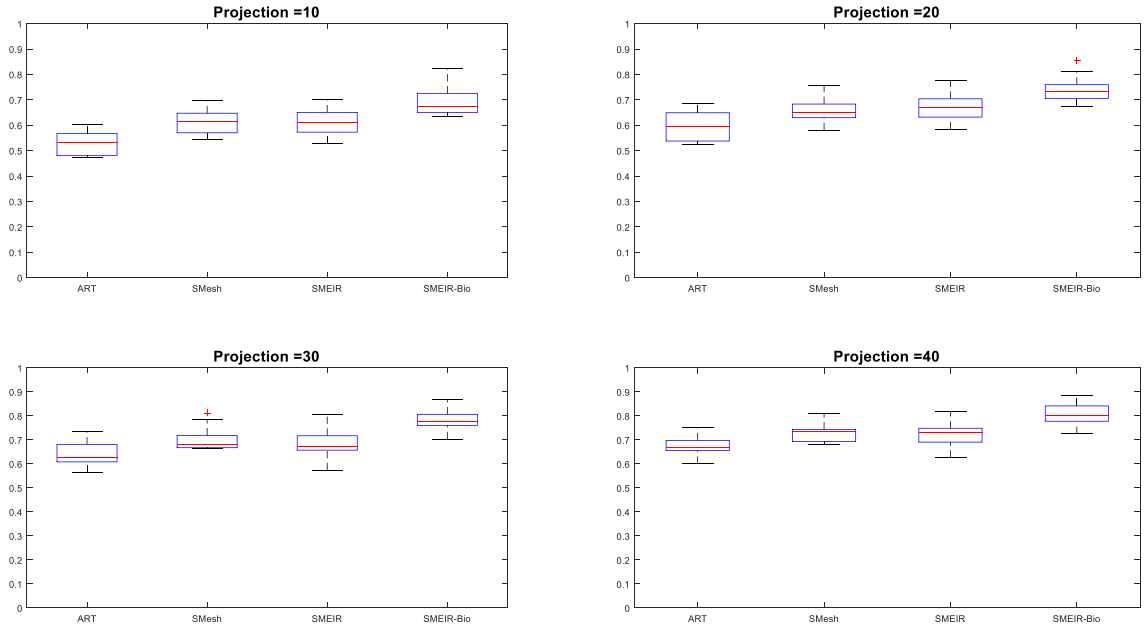

(C)

Figure 2-6 Quantitative comparison between ART-TV, SMesh, SMEIR and SMEIR-Bio with different projection number per phase. (A)RMSE; (B)UQI; (C) NCC.

The DVF accuracy, evaluated through manually-tracked lung landmarks, is shown in Figure 2-7. The landmarks displacement error calculated from different methods, SMEIR-Bio and SMEIR, using 30 projections per phase for reconstruction, along each of the Cartesian directions, x, y and z, is shown along with the D_{error}. In x and y direction, 9 out of 11 patients' displacement error for SMEIR-Bio are smaller than that for SMEIR. In z direction, all patients' displacement errors calculated from SMEIR-Bio are smaller than SMEIR. As lung motion occurs predominantly in the z (superior-inferior) direction, we specifically extracted DVFs in the z direction and calculated the corresponding landmarks displacement error between manually-tracked landmark motion and landmark motion extracted from DVFs. The average displacement difference along the z direction of all 11 patients is 2.49 mm for SMEIR-Bio and 4.03 mm for SMEIR. The average D_{error} of all 11 patients is 3.56 mm for SMEIR-Bio and 4.97 mm for SMEIR. We observed a

statistically significant difference ($p = 0.0013$, by Wilcoxon signed-rank test) between $D_{error}^{SMEIR-Bio}$ and D_{error}^{SMEIR} .

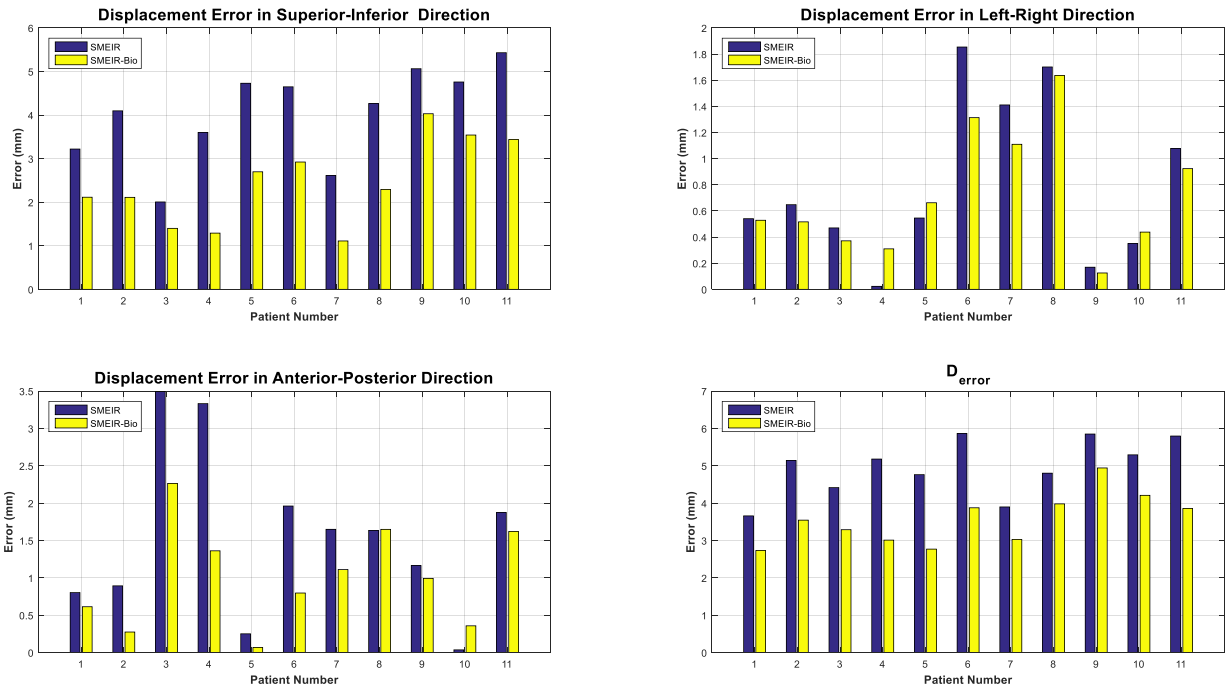

Figure 2-7 Average length of displacement error for all patients (1-11) along each of the three spatial directions (left-right (X direction), anterior-posterior (Y direction), and superior-inferior (Z direction)) and D_error.

Errors along each Cartesian direction and 3D vector errors are shown. For each patient, the left bar denotes the average displacement error of SMEIR reconstructions. The right bar denotes the corresponding error of SMEIR-Bio reconstructions. All reconstructions used 30 projections per phase.

The comparison between SMEIR and SMEIR-Bio reconstruction results based on real 4D CBCT patient data are showed below in Figure 2-8 and Table 2-3. In the Figure 2-8 the truncation artifacts are caused by the limited field of view during projection acquisition.

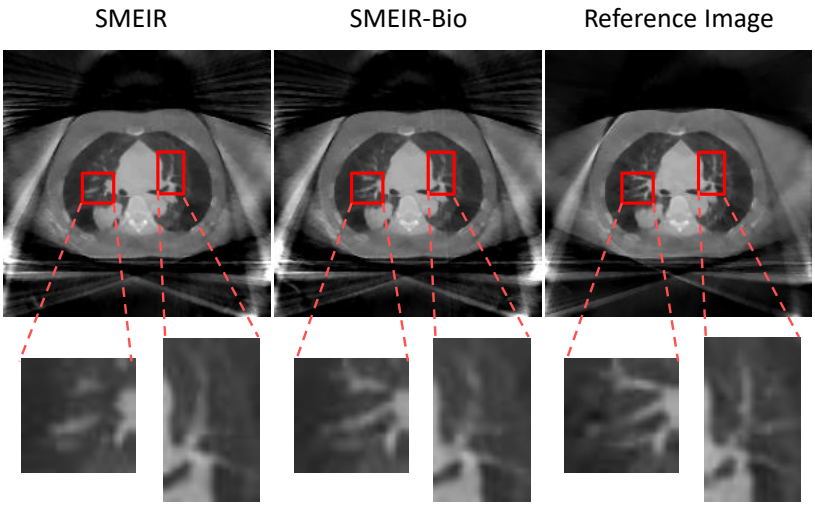

Figure 2-8 Comparison of patient 4D CBCT image at reference phase 0 reconstructed by SMEIR and SMEIR-Bio with the "gold-standard" reference image.

The first row shows images reconstructed by SMEIR and SMEIR-Bio, as well as the reference image. The second row shows 2 zoomed-in intra-lung ROIs. Note that the truncation artifacts are caused by the limited field of view during projection acquisition.

Table 2-3 Quantitative evaluation of patient 4D CBCT images at reference phase 0 reconstructed by SMEIR and SMEIR-Bio.

The images reconstructed from fully-sampled dense projections are used as the reference for evaluation.

	RMSE	RE	NCC	UQI
SMEIR	0.0033	15.22%	0.9383	0.9038
SMEIR-Bio	0.0031	14.53%	0.9435	0.9377

As shown in Figure 2-8 and Table 2-3, SMEIR-Bio can reconstruct images, especially the intra-lung details with higher accuracy. Using real clinical projections with scatter, noise and beam hardening, SMEIR-Bio outperforms SMEIR, and reconstructs images with fine lung details matched to the "gold-standard" reference image reconstructed from dense projections.

The effects brought by segmentation are evaluated. Visual and quantitative results for two patients are shown in Figure 2-9 and Table 2-4.

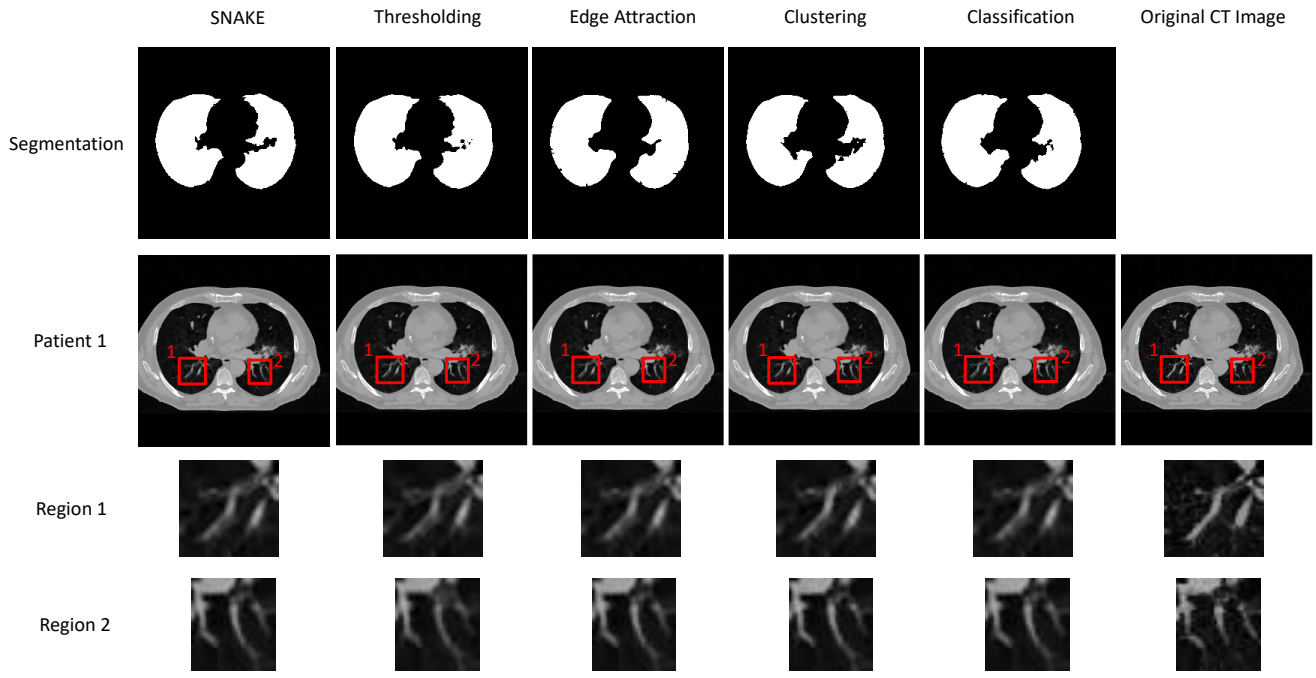

(A)

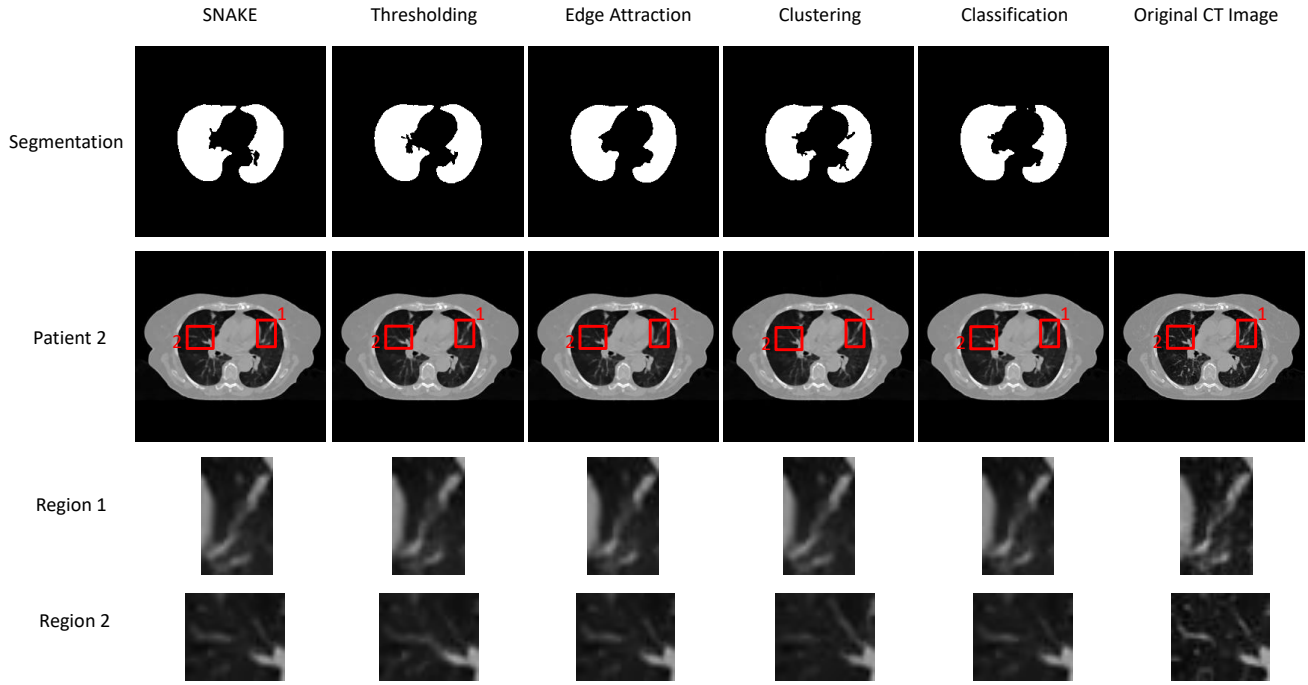

(B)

Figure 2-9 SMEIR-Bio reconstructed images at reference phase 0 with different segmentation methods

("snake", thresholding, edge-attraction, clustering and classification) for (A) patient 1 and (B) patient 2. For both (A) and (B), the first row shows lung segmentation using different methods; the second row shows images reconstructed by SMEIR-Bio using different segmentations, as well as the reference CT image; the third and fourth rows show intra-lung details extracted from second row. The display window for the second row is [-1000, 635] HU and is the same for zoomed-in region 1 and region 2.

As demonstrated in the Figure 2-9, segmentation masks generated using different methods have various boundaries especially around heart. However, when applied to the SMEIR-Bio, all of them can achieve high accuracy reconstruction compared with the ground-truth image. The reconstructed images share visual similarity. The effects of segmentation are quantified in Table 2-4. Lung regions are extracted to calculate RMSE, RE and NCC. The results show that reconstructed images are of similar accuracy when different segmentation methods are applied.

Table 2-4 Quantitative accuracy of the lung regions reconstructed by SMEIR-Bio with different segmentation methods

Images are reconstructed at the reference phase 0 using 30 projections from patient 1 and patient 2. The original 4D-CT image is used as the reference for evaluation.

	Patient 1				Patient 2			
	RMSE	RE	NCC	UQI	RMSE	RE	NCC	UQI
Thresholding	0.0033	14.38%	0.9778	0.8972	0.0035	13.52%	0.9724	0.8564
Edge-Attraction	0.0033	14.47%	0.9782	0.9011	0.0035	14.28%	0.9728	0.8723
Clustering	0.0032	13.69%	0.9794	0.8989	0.0036	14.54%	0.9714	0.8647
Classification	0.0033	14.05%	0.9790	0.9004	0.0035	14.22%	0.9729	0.8596
SNAKE	0.0032	14.29%	0.9780	0.8996	0.0036	14.43%	0.9725	0.8820

2.4 DISCUSSION AND CONCLUSION

We developed the SMEIR-Bio technique based on the SMEIR algorithm for 4D-CBCT reconstruction but added biomechanical modeling to the workflow to improve DVF and image reconstruction accuracy in low-contrast regions or regions with small fine details. Lung surface DVFs solved by 2D-3D deformation, whose accuracy benefits from the high-contrast lung boundary, served as the boundary condition to drive finite element analysis-based biomechanical modeling to fine-tune the intra-lung DVFs [103]. Based on our evaluation using 11 lung cancer patient cases, the proposed SMEIR-Bio algorithm enhances the reconstructed 4D-CBCT quality, as well as the accuracy of inter-phase DVFs. The accurate 4D-CBCT and DVFs have the potential to be applied to patient setup, tumor tracking, dose accumulation, and adaptive radiation therapy [104, 105].

Our work viewed the intra-lung structures as homogeneous in material. In reality, however, there are various heterogeneous structures within the lung, including bronchi and lung vessels. In addition, for patients who have large areas of necrosis, inflammation or pneumonitis in lung, the lung tissue elasticity may also vary from region to region. Correspondingly, the solved intra-lung DVF under the homogeneity assumption can be error-prone in these regions. Therefore, future research should consider different elastic properties and model the interactions between different structures inside the lung to achieve a more biomechanically realistic deformation. Multi-organ deformation analysis based on the biomechanical modeling method can be applied to SMEIR-Bio to simulate the lungs' motion in light of their interactions with different organs [96]. This analysis views the thoracoabdominal region as a whole and simulates the motion of organs that do not have

a clear boundary using adjacent organs' motion. Furthermore, the air low mechanics inside the lung could also be modeled to improve the accuracy of biomechanical modeling [106].

The proposed SMEIR-Bio method also requires more computation time than SMEIR because of the additional biomechanical modeling component. Currently, we only use the CPU for image reconstruction. Within each iteration, the motion-compensated reconstruction takes about 25 minutes, the 2D-3D registration takes about 20 minutes, and the biomechanical modeling takes about 20 minutes. For all 11 patients, 7-10 iterations were needed for SMEIR-Bio to converge. GPU programming as well as multi-threading in the CPU can help accelerate the image reconstruction process.

In summary, the developed SMEIR-Bio method enhances DVF accuracy of inside lung region with fine structures. To further decrease the computational time for biomechanical modeling, we applied CNN based method to solve the DVFs of inner lung which is introduced in the CHAPTER THREE.

3 CHAPTER THREE
U-net-based Deformation Vector Field Estimation for Motion-Compensated 4D-CBCT Reconstruction

3.1 INTRODUCTION

4D-CBCT images usually suffer from degraded image quality due to insufficient numbers of projections in each phase bin after phase-sorting. Many different methods have been developed to improve the 4D-CBCT image quality in the under-sampling scenario [40, 41, 45, 107]. Recently, we developed a method called simultaneous motion estimation and image reconstruction (SMEIR) for 4D-CBCT reconstruction. By using all acquired projections and the motion model for motion-compensated reconstruction, SMEIR can effectively reduce the under-sampling and over-smoothing effects in the reconstructed 4D-CBCT. Simultaneously, SMEIR optimizes the deformation-driven motion model between the reference phase CBCT image and all other 4D-CBCT phases.

To estimate the motion model, SMEIR uses an intensity-driven 2D-3D deformation method, which performs well at high-contrast regions such as the lung boundary, where motion causes large intensity variations on the 2D projections to drive the DVF optimization. For intra-lung regions, where many small, intricate structures exist, the 2D-3D deformation technique usually cannot estimate accurate DVFs since the movement of these small structures only leads to subtle changes on the 2D projections. To solve this issue, we recently combined finite-element-analysis (FEA)-based biomechanical modeling with SMEIR to enhance the accuracy of the intra-lung DVFs (SMEIR-Bio) [84, 108]. By biomechanical modeling, the intra-lung DVFs can be derived and optimized from lung boundary DVFs based on elastic parameters of lung tissues [108]. However, SMEIR-Bio involves additional steps including tetrahedral mesh generation, boundary

information extraction and FEA. A simpler and more efficient method can further improve the efficiency of the SMEIR-based algorithm.

In this study, instead of using biomechanical modeling, we used convolutional neural networks (CNNs) to fine-tune the DVFs estimated by 2D-3D deformation. Previous studies have shown that CNN-based approaches are effective in solving DVFs directly between 3D reference and moving images [109-112]. Those methods used MRI or CT images to achieve DVF estimation based on the high image quality. These methods cannot be applied towards 2D-3D deformation. Although we can reconstruct 3D images from phase-sorted projections before feeding into the network, their accuracy might be impaired by the streak artifacts in the 3D images, which in our cases are caused by under-sampled projections. Thus in this study, instead of using the CNN to directly derive DVFs between images, we used the network to fine-tune the 2D-3D deformation-estimated DVFs to mimic the role of biomechanical modeling. In this study, two CNN models were built based on the U-net [113] architecture to optimize the DVF estimated by 2D-3D deformation. Both models were trained, validated and evaluated on a simulated 4D-CBCT from a cohort containing 11 lung patient cases. We evaluated and compared the SMEIR techniques incorporating CNN-derived DVFs, with previously-developed techniques (SMEIR and SMEIR-Bio), in terms of image quality of reconstructed 4D-CBCTs and the motion model (DVF) accuracy.

3.2 MATERIALS AND METHODS

3.2.1 Methods

3.2.1.1 The SMEIR technique

The original SMEIR algorithm has two main steps: motion-compensated reconstruction and motion estimation. The overall workflow is shown in Figure 3-1. The detailed introduction is listed in the CHAPTER TWO section 2.2.1.

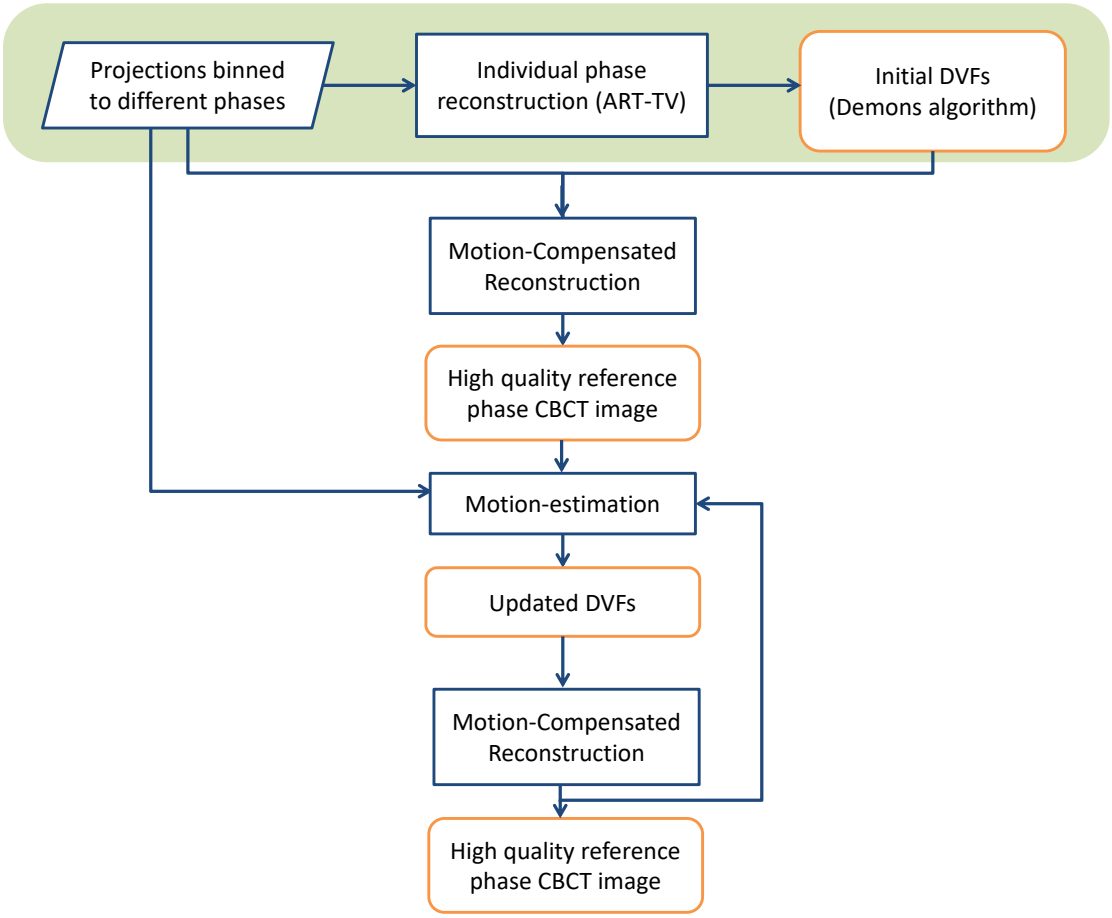

Figure 3-1 Workflow of the simultaneous motion estimation and image reconstruction (SMEIR) method.

ART-TV: algebraic reconstruction technique with total variation regularization [114]. The processes in green region are initialization part to obtain images of each phase and initial motion model.

3.2.1.2 SMEIR-Bio

In order to boost the accuracy of the intra-lung DVFs, we recently developed a biomechanical modeling-guided SMEIR technique to combine the SMEIR method with biomechanical modeling (SMEIR-Bio). By SMEIR-Bio, for each patient, a tetrahedral mesh based on segmented lung contours of the reference phase CBCT was generated. The lung boundary motion estimated by SMEIR, using 2D-3D deformation was extracted and assigned to the boundary vertices of the mesh. As high contrast and sharp variations exist at lung boundaries, the intensity-based 2D-3D deformation employed in the original SMEIR algorithm achieves high DVF accuracy at these regions, in contrast to intra-lung regions. After boundary condition assignment, corresponding lung elasticity parameters were also assigned to the lung tetrahedral mesh. Through finite-element-analysis [115], intra-lung DVFs can be obtained from the lung boundary motion and the lung elasticity parameters using displacement-based biomechanical modeling [116]. The workflow of SMEIR-Bio is shown in Figure 3-2. Our previous study showed that the SMEIR-Bio algorithm outperformed the original SMEIR method in fine-tuning the motion model at intra-lung regions. Details of the SMEIR-Bio method can be found in CHAPTER TWO Method section 2.2.1.3 [108].

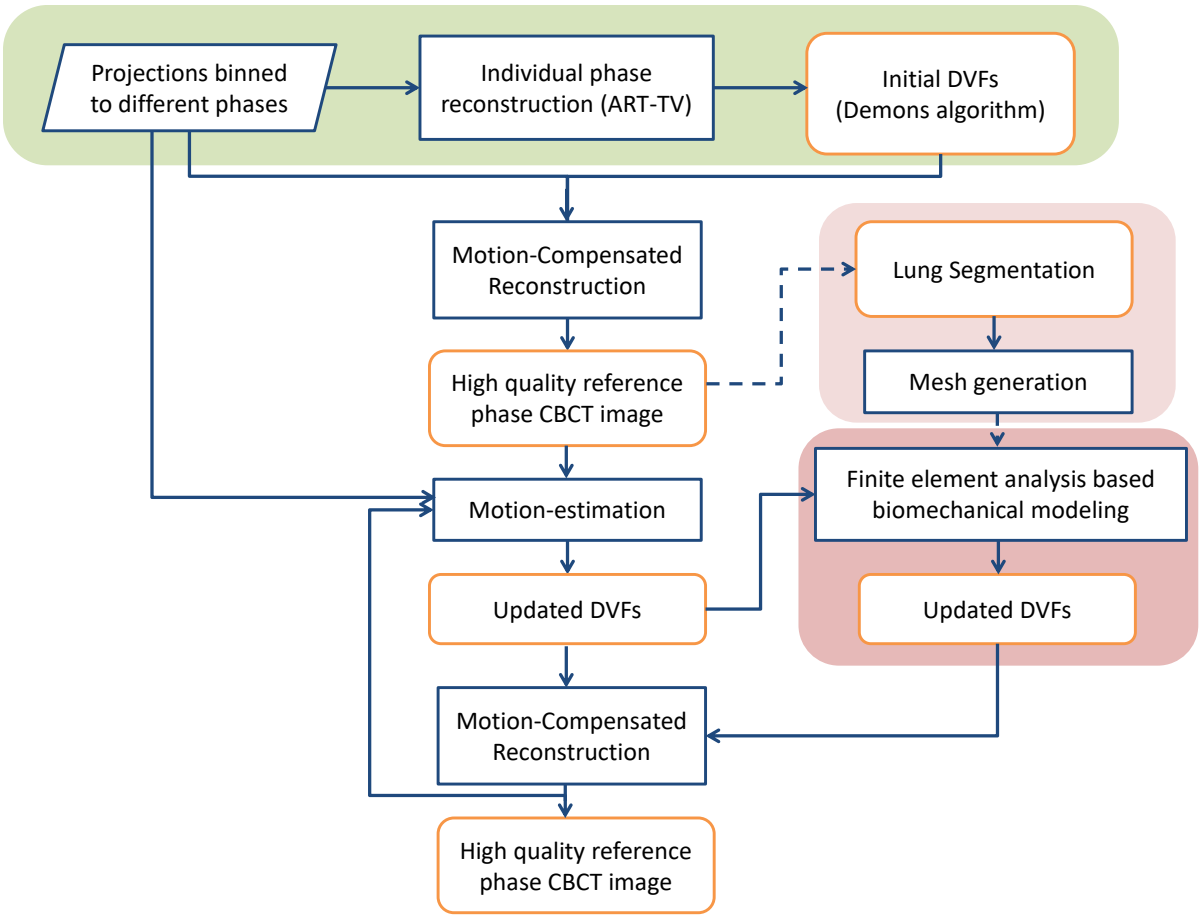

Figure 3-2 The workflow of SMEIR-Bio method.

The lung segmentation and mesh-generation parts in the light red region will only be processed once (dash line arrow). The Biomechanical modeling solved by FEA is in the dark red region demonstrating the on-line process which participated in iteratively reconstruction. The dark green region included processes to generate ART-TV images and initial DVFs before the SMEIR iteration.

3.2.1.3 SMEIR with U-net-based DVF optimization

SMEIR-Bio method iteratively optimizes the inner lung deformation vector field which is time consuming and the inner lung is regarded as homogeneous in the biomechanical model. Each patient needs to be assigned with patient-specific physical properties to achieve best performance. In this study, we proposed a deep learning-driven strategy to fine-tune the intra-lung DVFs

estimated through 2D-3D deformation method. We hypothesize that the CNN can find and learn informative features to derive intra-lung DVFs from accurate lung-boundary DVFs [113].

In detail, we developed two U-net based architectures to fine-tune the DVFs Figure 3-3. The first U-net architecture (U-net-3C) used three channels as input, which was denoted as U-net-3C. Each direction of the DVF (for three cardinal directions: x, y and z) served as one input channel, and had a dimension of $128 \times 128 \times 128$. The output also contained 3 channels, each for one cardinal direction of the updated DVF. Same as the input channel, each output channel was also of size $128 \times 128 \times 128$. In the second U-net architecture (U-net-4C), we added the CBCT reference phase image, which was reconstructed by SMEIR, as an additional input channel. The purpose of adding the lung CBCT image as the fourth channel was to train the network to learn heterogeneous properties of intra-lung tissues, which were potentially correlated with the local deformation patterns. The output of U-net-4C was the same as U-net-3C. DVFs estimated through 2D-3D registration methods served as input DVFs for both U-net-3C and U-net-4C channel. The ground-truth DVFs used for the network to match the input to are generated by the Demons registration algorithm [47] applied to high-quality 4D-CT between reference phase and other respiration phases.

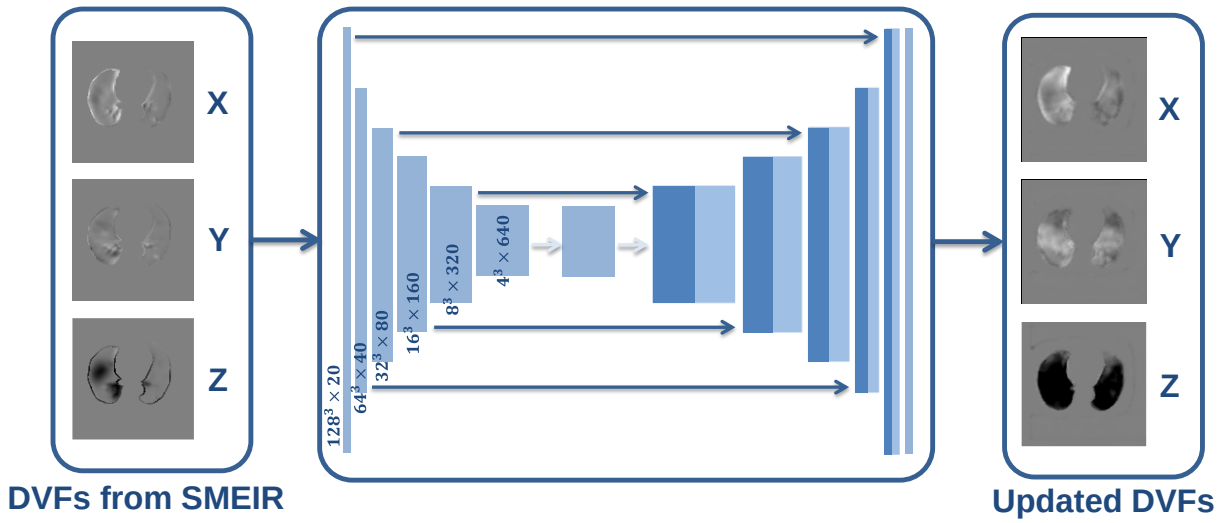

(A)

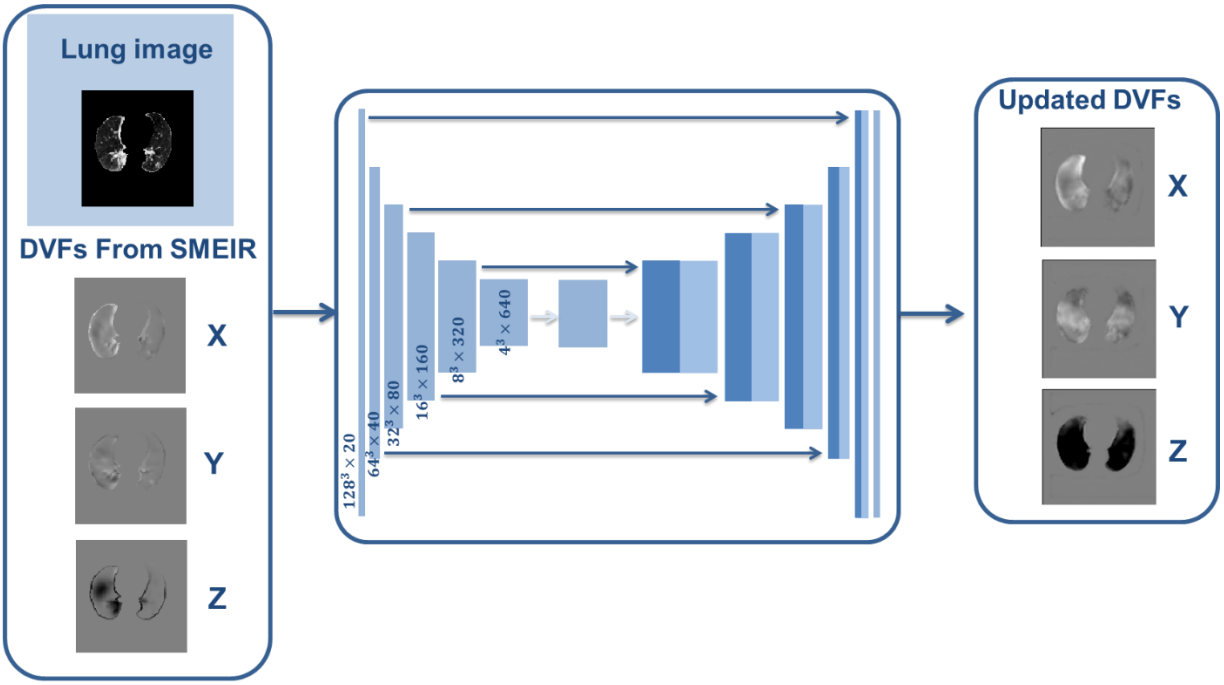

(B)

Figure 3-3 Two proposed CNN structures.

(A). U-net-3C architecture. The DVFs estimated by 2D-3D deformation were input using three channels (3C), and the output is updated DVFs with three channels. (B). U-net-4C architecture. Compared with U-net-3C, another channel was fed as the input for U-net-4C, which was the reference CBCT image reconstructed by SMEIR.

Both U-net-3C and U-net-4C contained two paths: the contraction path and the expansion path. The contraction path was composed of 5 blocks and each block was composed of 2 convolution layers and a max pooling layer. Symmetrically, the expansion path contained 6 blocks and each block contained 1 deconvolution layer and 2 convolution layers. The networks were implemented in Python with Keras as the backend. We used Adam [117], a method for efficient stochastic optimization, to optimize the network by minimizing the mean-square-error cost function with the initial learning rate set to from 1e-3 to 1e-7 (each time multiplying by 2 or 5) and β_1 and β_2 set as default. Model training starts with initial learning rate at 5e-5 have the best performance. The initial filter number was 20 and the size of each layer was shown in Figure 3-3 (A) and (B). The batch size of the training model was 4. We also trained the model with batch size of 8 while performance did not improve.

Both U-net-3C and U-net-4C were incorporated into the SMEIR workflow to fine-tune the estimated inter-phase DVFs, and the output DVFs were used to update the motion-compensated CBCT and the other phase CBCTs as a final step, before outputting the final 4D-CBCTs, as it is shown in the Figure 3-4. Based on different models used, we named the corresponding modified SMEIR algorithm as either SMEIR-U-net-3C or SMEIR-U-net-4C.

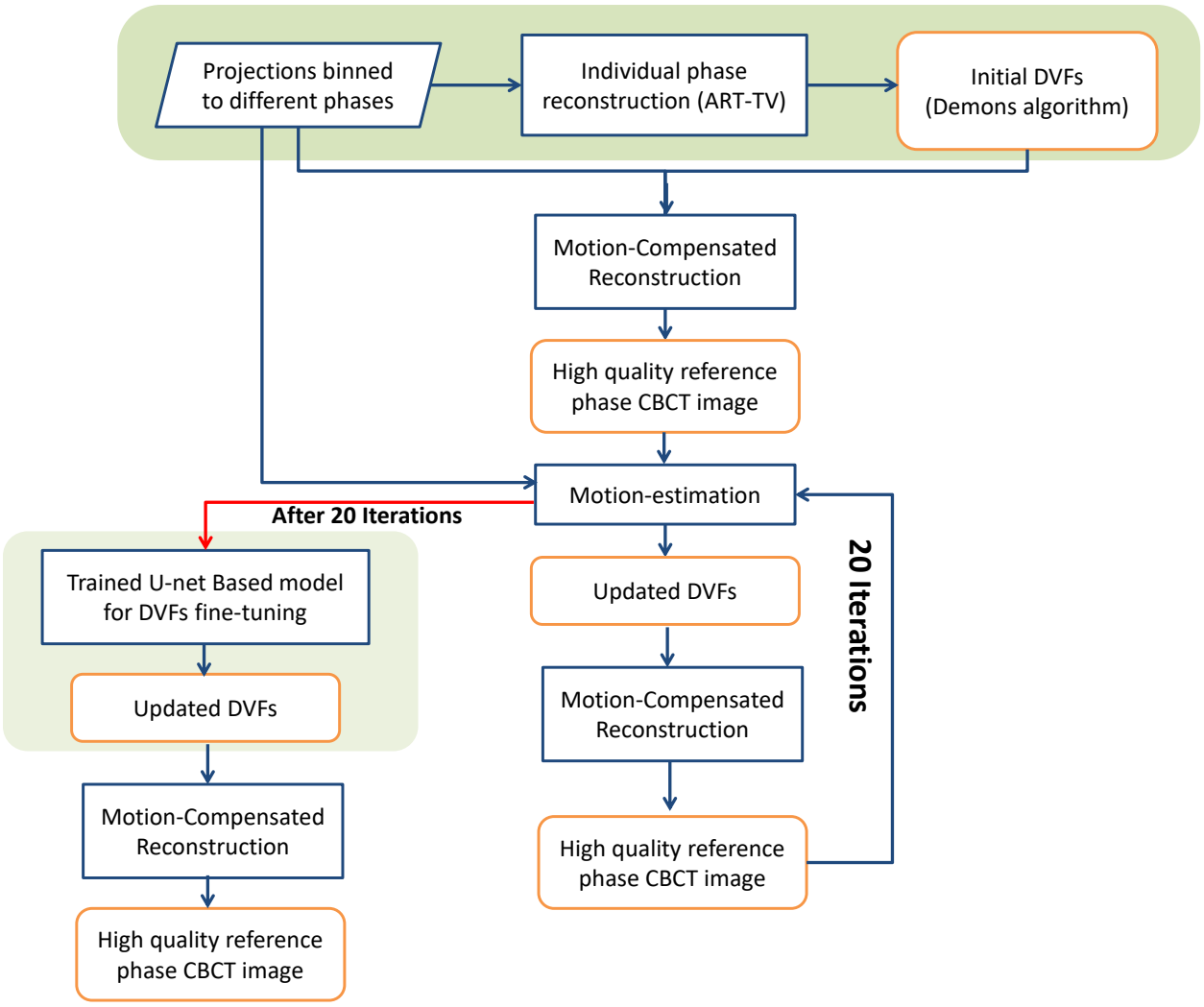

Figure 3-4 SMEIR-U-net workflow.

The trained model served as one fine-tuning step. The dark green region included processes to generate ART-TV images and initial DVFs before the SMEIR iteration. The light green region included processes to fine-tune the DVFs using U-net based methods.

3.2.2 Materials

To evaluate our method, we used a dataset consisting of 4D-CT images of 11 lung cancer patients [118]. The 4D-CT images were acquired by a 16-slice CT scanner (Brilliance, Philips Medical Systems, Cleveland, OH). Images were acquired in 3 different resolution levels

(0.7813×0.7813×1.5 mm^3, 0.9375×0.9375×1.5 mm^3 and 0.9766×0.9766×1.5 mm^3), and were resized into the same resolution level of 1.5×1.5×1.5 mm^3. In order to evaluate the feasibility of clinical usage of the proposed method, we applied Monte Carlo (MC) simulation using the toolkit gDRR [119, 120], which is a GPU-based MC simulation package, to generate projections with scatter to simulate the acquired CBCT projections from Linac. We used simulated projections with scatter to process the training, validation and testing.

For each patient, we performed MC simulation on 4D-CT images to obtain 4D-CBCT projections with scatterings and noise. For each phase, we used half-fan scanning protocol to simulate 80 projections with scan angles evenly distributed across 360°. The simulation source-to-axis distance was 1000 mm and the source-to-image distance was 1500 mm, while offset in X direction (Left-Right) is 148 mm to include the lung boundary. Each projection contained 512×384 pixels, with resolution 0.776×0.776 mm^2. We zeros-padded half-fan projections to synchronize rotation center and imager center to obtain the full-fan-sized projections. We down-sampled projections by two in each direction and the size of reconstructed images are 256×256×256. The SMEIR method was applied to reconstruct 4D-CBCTs and estimate intra-phase DVFs with resolution 1.5×1.5×1.5 mm^3, with dimension 256×256×256. The other reconstruction parameters were the same as those in our previous publication [46]. For SMEIR-Bio, the other parameters were also the same as those in our previous publication [108].

Four of the 11 lung SBRT patients had 10 phase images and the other had 8 phases. We can generate a total of 85 DVFs between the end-of-exhale (EE) phase (reference phase) and other 4D-CT phases to train the proposed model. The 11 patients were separated into 5 groups to form 5 folders, each containing DVFs from 2 or 3 patients, to perform a 5-fold cross validation. Each time we selected 3 folders for training, 1 for validation, and 1 for testing. For the two CNN-based

techniques, before CNN updates, we down-sampled the input DVFs generated by SMEIR (from 256×256×256) to 128×128×128 along each direction to tailor to the GPU memory limits. After CNN updates, we up-sampled the updated DVFs back to size 256×256×256 using cubic interpolation [121]. We used a NVIDIA Tesla v100-sxm2 GPU card for training. We trained the model of each fold for 400 epochs and saved the weights of the model at the 400th epoch. Then the training process continued based on the saved model weights and were stopped if the minimal validation loss did not change for 50 epochs. The computation time for each-fold training was around 6 hours. After we finished the training process, the trained network took roughly 10 seconds to output improved DVFs of size 128×128×128, for both U-net-3C and U-net-4C.

We compared the quality of the reconstructed images between SMEIR, SMEIR-Bio, SMEIR-U-net-3C and SMEIR-U-net-4C using metrics including the root-mean-square-error (RMSE) [99], the universal quality index (UQI) [101] and the normalized cross-correlation [100]. Since the study was focused on improving the reconstruction quality of intra-lung regions with fine details, we selected 10 relevant regions-of-interests (ROIs) inside the lung to compute these metrics. We used the original CT images as the 'gold-standard' reference to evaluate the reconstruct CBCT images.

For each 4D-CT set, around 80 landmarks were manually identified by expert physicians to track intra-lung motion from the EE to the end-of-inhale (EI) phases (872 in total). Using these landmarks, we evaluated the accuracy of DVFs estimated by the original SMEIR algorithm, SMEIR-Bio, SMEIR-U-net-3C, and SMEIR-U-net-4C. The DVF residual error was defined as the magnitude of the 3D difference between the manually-tracked landmark motion and DVF-tracked landmark motion.

To further evaluate the proposed method, we used 4D-CBCT data from SPARE challenge[122]. We selected 3 patients (with diaphragm covered by field-of-view) in the SPARE challenge dataset to test our trained models. We applied SMEIR reconstruction on those 3 patients to obtain reference phase image and raw DVFs. The estimated DVFs are truncated and down-sampled into the same size as our network structures. We applied fine-tuned DVFs in the MC-SART to obtain the updated reference phase image. The quantitative comparison between SMEIR-U-net-3C, SMEIR-U-net-4C and SMEIR methods are based on image quality. RMSE, UQI and NCC metrics are used.

3.3 RESULTS

3.3.1 Monte Carlo simulation data

Comparison between different DVFs was shown in Figure 3-5. The input intra-lung DVF was not well estimated by the original SMEIR algorithm. Compared with the input DVFs, the updated DVFs had visually improved accuracy for intra-lung regions. With additional channel input specifying lung heterogeneity information, the U-net-4C DVFs appeared more similar to the Demons DVF.

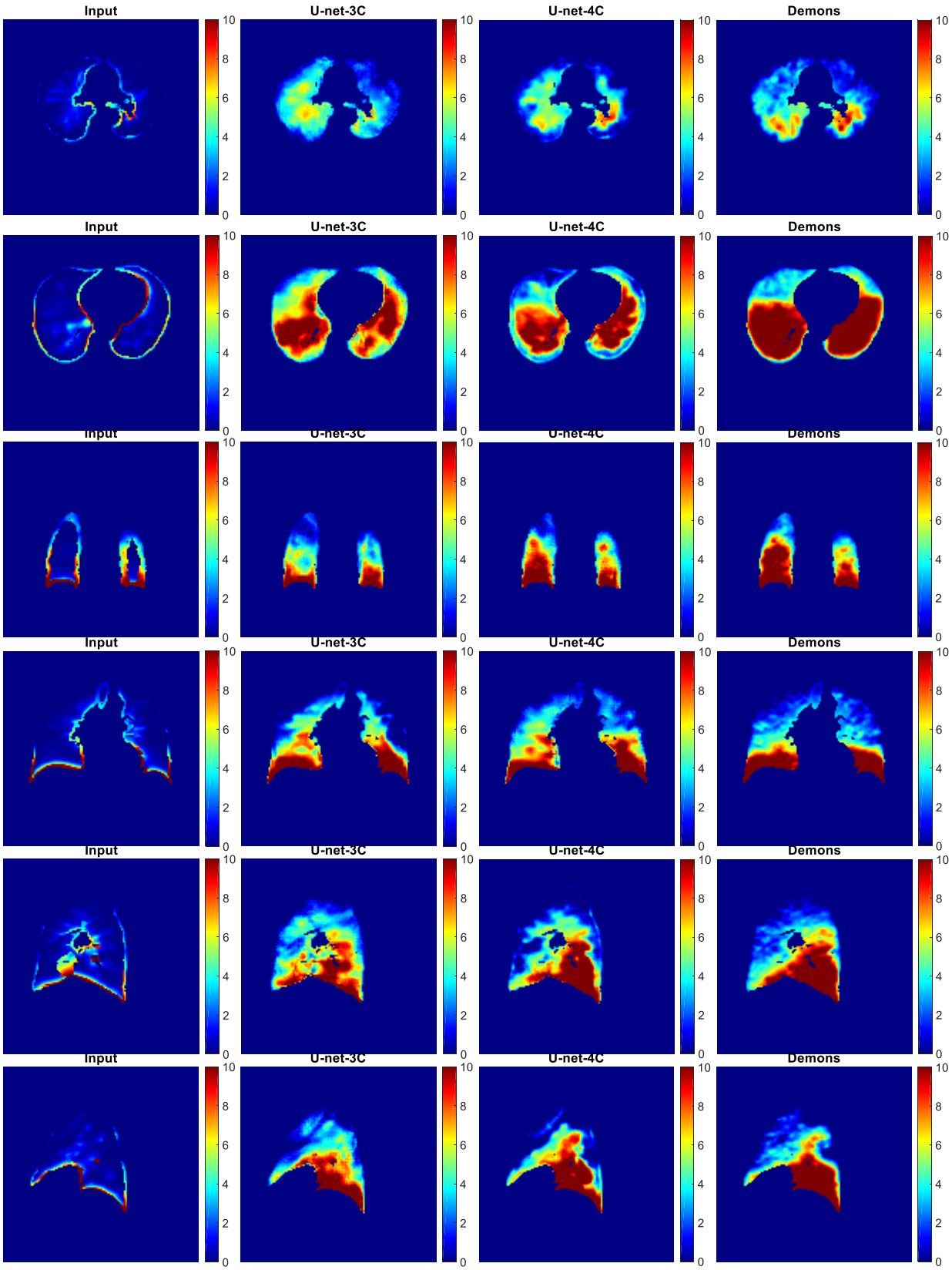

(A)

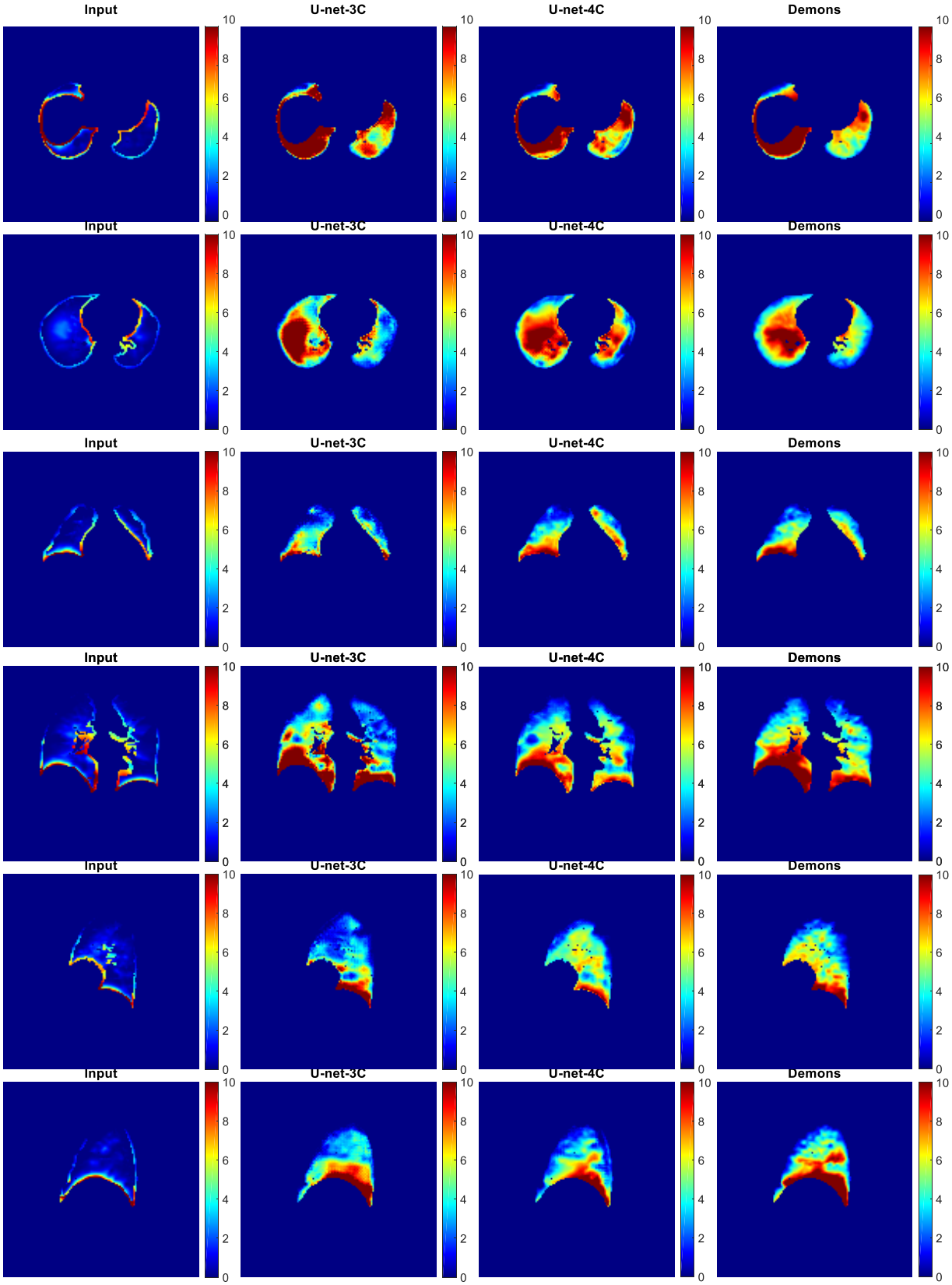

(B)

Figure 3-5 Comparison between DVFs for two patient cases: (A) and (B).

For each subfigure, the first column showed the input DVFs estimated by the original SMEIR algorithm. The second and third columns showed the updated DVFs by U-net-3C and U-net-4C, respectively. The fourth column showed the reference Demons DVFs, which were used as the 'ground-truth' for network training and validation. Row 1-2, 3-4 and 5-6 showed DVFs in axial, coronal and sagittal views, respectively, for two different slice locations. All DVFs were shown by window level [0, 10] voxels.

Figure 3-6 illustrated the residual DVF errors for different methods. Compared with SMEIR and SMEIR-Bio methods, CNN-based methods (U-net-3C and U-net-4C) achieved higher DVF accuracy. The average (± standard deviation) landmarks motion is $6.53 \pm 5.15\ mm$. When the input used 3-channel DVFs only (U-net-3C), the average residual error was $3.88 \pm 3.12\ mm$. When reference phase CBCT was added as an additional channel to the input layer (U-net-4C), the average residual error was reduced to $3.71 \pm 2.90\ mm$. The average DVF residual error was $5.73 \pm 4.61 mm$ for SMEIR method and $3.75 \pm 3.40\ mm$ for the SMEIR-Bio method. We applied Wilcoxon signed test on DVFs residual error of all 872 landmarks to evaluate the statistical significance for each pair of methods. SMEIR are statistically significant with both U-net based method ($p<0.001$). No statistical significance was found between the SMEIR-Bio method and either CNN-based method ($p>0.05$). No statistical significance was found between SMEIR-U-net-3C and SMEIR-U-net-4C ($p>0.0083$). We did Bonferroni correction [123, 124] for multiple comparisons.

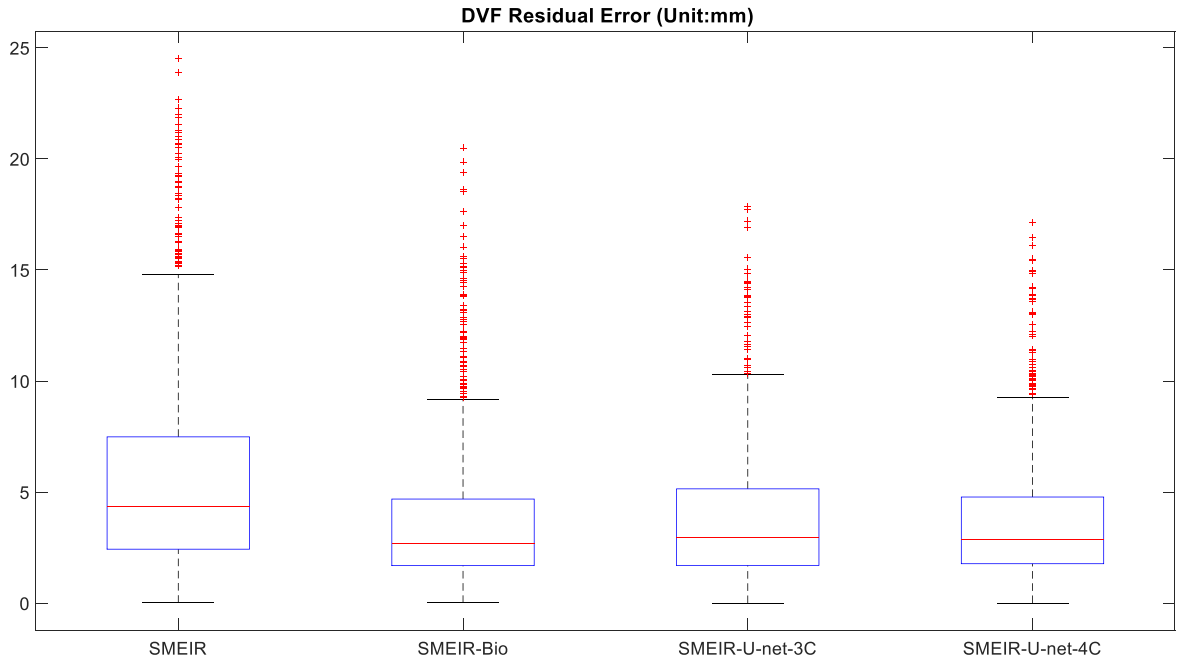

Figure 3-6 Boxplots of average residual DVF errors of all patients for SMEIR, SMEIR-Bio, SMEIR-U-net-3C and SMEIR-U-net-4C based on MC simulation projections.

The blue box shows the interquartile range (IQR) from 25th percentile (Q1) to 75th percentile (Q3). The dotted line extended from Q1-1.5×IQR to Q3+1.5×IQR. Red dots show the outliers.

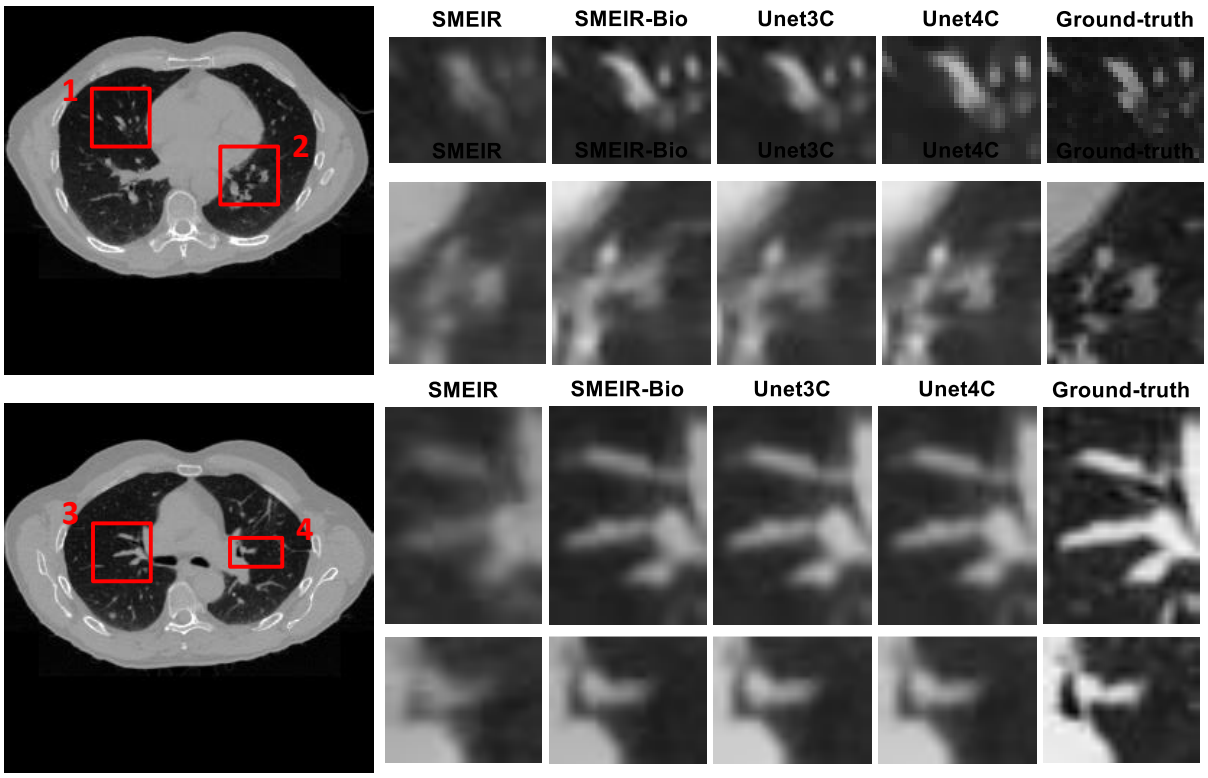

Figure 3-7 Extracted and zoomed-in details for 4 ROIs in the reconstructed reference phase CBCT image of one patient case.

The locations of the ROIs were highlighted by squares in the left-column. The 2nd to 5th columns on the right showed the zoomed-in ROIs from CBCTs reconstructed by SMEIR, SMEIR-Bio, U-net-3C and U-net-4C. The rightmost column showed the 'ground-truth' CT image at the reference phase. The display window (attenuation coefficient) for all images was [0, 0.04].

The corresponding CBCT images (at the reference EE phase) reconstructed by different methods were included in Figure 3-7. For each patient, we selected 10 ROIs inside lung. As shown, CBCT images reconstructed using DVFs updated by CNN-based methods can better recover fine details inside the lung. Figure 3-8 shows the boxplots of the quantitative metrics evaluating the similarity between the reconstructed CBCT images and the original CT images. The average (± standard deviation) RMSEs of the evaluated ROIs were 0.0046 ± 0.0004 (SMEIR), 0.0037 ± 0.0005 (SMEIR-Bio), 0.0037 ± 0.0005 (SMEIR-U-net-3C) and 0.0038 ± 0.0004 (SMEIR-U-net-4C). The average UQIs of the evaluated ROIs were 0.61 ± 0.04 (SMEIR), 0.82 ± 0.03 (SMEIR-

Bio), 0.82 ± 0.04 (SMEIR-U-net-3C) and 0.84 ± 0.04 (SMEIR-U-net-4C). Similarly, the average NCCs for SMEIR, SMEIR-Bio, SMEIR-U-net-3C and SMEIR-U-net-4C were 0.69 ± 0.05, 0.83 ± 0.04, 0.84 ± 0.06 and 0.87 ± 0.06, respectively. Overall, CNN-based SMEIR methods achieved better image reconstruction accuracy. We did Wilcoxon signed-rank test to evaluate the statistical significance of the UQI difference of images reconstructed by different methods. According to the results, there is statistical significance of UQI difference between SMEIR and SMEIR-U-net-3C as well as between SMEIR and SMEIR-U-net-4C ($p<0.001$). No statistical significance of UQI difference was found between SMEIR-Bio and SMEIR-U-net-3C, nor between SMEIR-Bio and SMEIR-U-net-4C ($p>0.0083$). There is no statistical significance of UQI difference between SMEIR-U-net-3C and SMEIR-U-net-4C ($p>0.0083$).

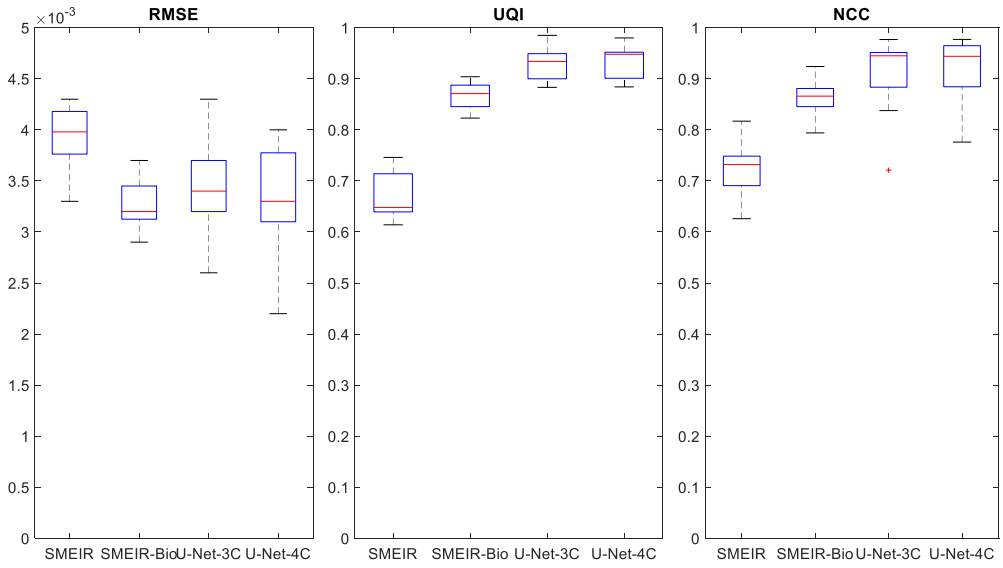

Figure 3-8 Boxplots of RMSE, UQI and NCC metrics for SMEIR, SMEIR-Bio, SMEIR-U-net-3C and SMEIR-U-net-4C.

In order to evaluate the influence brought by splitting training and validation dataset, we fixed the group 5 (Patient 10 and 11) as test group. We select 1-3 (patient 1-7) groups as training

dataset and groups 4 (patient 8 and 9) as validation dataset to train a model. Then, we selected 1, 3 and 4 group (patient 1, 2 and 5-9) as training dataset and group 2 (patient 3 and 4) as validation dataset to train the second model. The influence brought by splitting training/validation dataset is evaluated on manually tracked landmarks of patient 10 and patient 11. The DVFs residual errors calculated based on different training/validation splitting are displayed in Table 3-1. Different split of training and validation does not influence the accuracy of predicted DVFs.

Table 3-1 Influence of different training/validation split. Averaged (± standard derivation) DVFs residual errors calculated based on DVFs obtained from model trained by different training/validation split. (Unit:mm)

DVFs residual errors	U-net-3C	U-net-4C
Training (1-3)/ Validation(4)	3.84 ± 2.22	3.73 ± 2.13
Training(1,3,4)/Validation(2)	3.89 ± 2.41	3.80 ± 1.99

We separated landmarks by their locations, including inner lung and tumor. We calculated the residual error of DVFs of different methods based on landmarks in different groups to evaluate the location-specific improvement bring by proposed method. We focused on inner lung markers and markers inside tumor. The comparison results are shown in Table 3-2. Based on the results, we considered that proposed U-net based methods can improve the accuracy for DVFs estimation for inside lung region (including the tumor) compared with SMEIR method. The performances of U-net based methods are similar to that of SMEIR-Bio method. We applied the Wilcoxon signed-rank test to evaluate the statistical significance between different methods. For inner lung landmarks, the residual DVF error difference between the SMEIR method and either CNN-based method was statistically significant ($p<0.005$). The residual DVF error difference between the U-net-3C and U-net-4C method was statistically significant ($p<0.005$). The residual DVF error

difference between the U-net-3C and SMEIR-Bio method was statistically significant ($p<0.005$) while there is no statistical significance between SMEIR-Bio and U-net-4C. The residual DVF error difference between the U-net-3C and U-net-4C method was statistically significant ($p<0.005$). There are no statistical significance between SMEIR-Bio and U-net-4C ($p>0.1$) and between SMEIR-Bio and U-net-3C ($p>0.05$).

Table 3-2 The location-specific DVFs residual error (Unit: mm).

	SMEIR	SMEIR-Bio	U-Net-3C	U-Net-4C
Tumor markers (110)	4.03	3.03	2.98	2.75
Inner markers (433)	6.87	3.82	3.52	3.56

To evaluate the smoothness of the DVFs in the spatial domain, we calculated the total variation (TV) of DVFs generated from U-net based method and compared to the total variation of DVFs from Demons. The averaged total variation of DVFs obtained from U-net-3C, U-net-4C and Demons are 2.7383e+05, 3.1249e+05 and 3.0409e+05. The value of total variation calculated based on DVFs from different methods are in the same level. DVFs obtained from U-net-3C are smoother compared with DVFs from U-net-4C. It is reasonable since there is one additional input channel offering heterogeneous information for the network to learn from.

3.3.1.1 SPARE challenge data

We used metrics of RMSE, UQI and NCC to evaluate the quality of reconstructed images. The "gold-standard" images are reconstructed based on fully-sampled projections. For each patient, we select 10 ROIs inside of lung to evaluate the performance of detailed lung structure

reconstruction. Some of the ROIs are shown in Figure 3-9. The quantitative comparisons based on RMSE, UQI and NCC metrics are shown in Figure 3-10. You can see in the picture that SMEIR-Bio, SMEIR-U-net3C and SMEIR-U-net-4C have similar results for restoring intra-lung detailed structures. U-net-4C can have better performance for some ROIs.

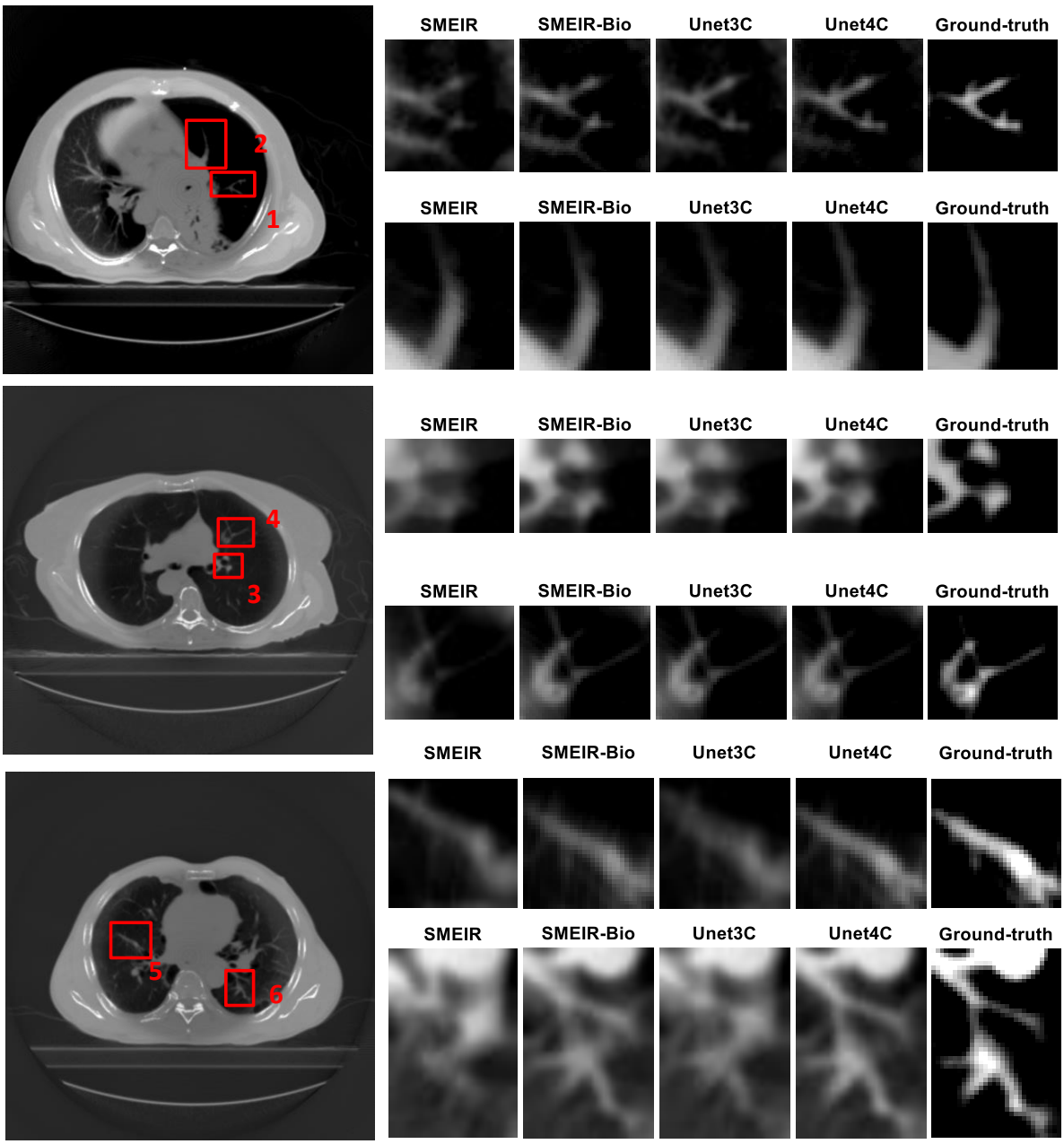

Figure 3-9 Extracted and zoomed-in details for 4 ROIs in the reconstructed reference phase CBCT image of 3 patients.

The locations of the ROIs were highlighted by squares in the left-column. The 2nd to 5th columns on the right showed the zoomed-in ROIs from CBCTs reconstructed by SMEIR, SMEIR-Bio, U-net-3C and U-net-4C. The rightmost column showed the 'Gold-standard' CBCT image at the reference phase reconstructed from fully-sampled projections. The display window (attenuation coefficient) for all images was [0, 0.03].

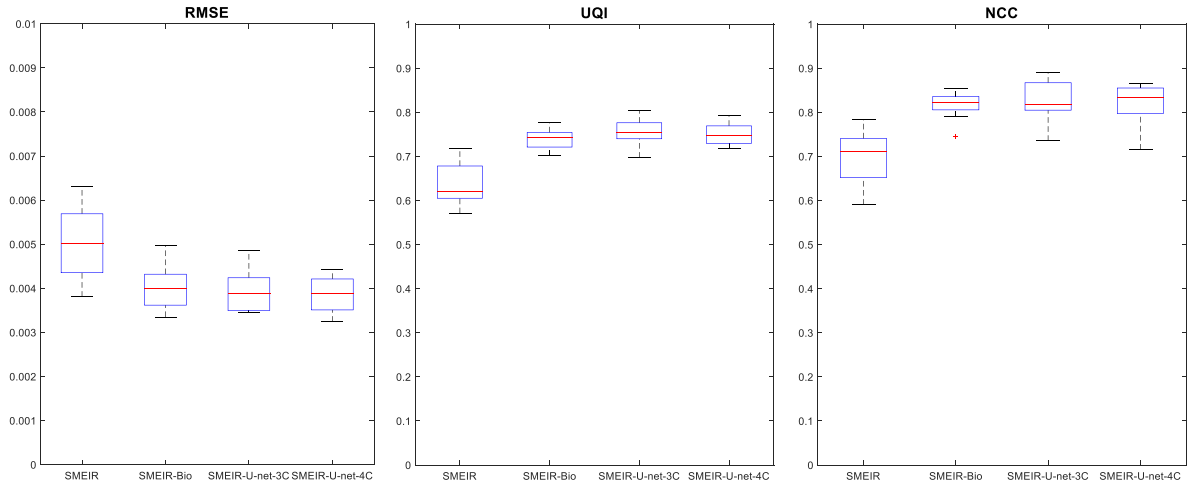

Figure 3-10 Boxplots of RMSE, UQI and NCC metrics for SMEIR, SMEIR-Bio, SMEIR-U-net-3C and SMEIR-U-net-4C.

The evaluations based on the whole images are shown in the Table 3-3. SMEIR-U-net based methods outperform SMEIR method in reconstructing fine-details inside lung. SMEIR-Bio and SMEIR-U-net methods have similar results.

Table 3-3 Quantitative evaluation of SPARE reference phase image of SMEIR, SMEIR-Bio, SMEIR-U-net-3C and SMEIR-U-net-4C method.

The images reconstructed from fully-sampled dense projections are used as the reference for evaluation.

	RMSE	NCC	UQI
SMEIR	0.0045	0.91	0.94
SMEIR-Bio	0.0035	0.94	0.96
SMEIR-U-net-3C	0.0036	0.93	0.96
SMEIR-U-net-4C	0.0033	0.93	0.97

3.4 DISCUSSION

In this study, we proposed a CNN-based DVF fine-tuning framework to improve the accuracy of intra-lung DVFs estimated by 2D-3D deformation for SMEIR. Since the lung contains many small fine structures, their deformation is hard to be estimated accurately, especially using only limited-view 4D-CBCT projections. Our U-net based techniques were able to update and fine-tune the 2D-3D DVFs from provided lung contours and lung images (Figure 3-3), through inferencing the relationship between the 2D-3D DVFs and the 'ground-truth' Demons DVFs via the lung structural information. The comparison between the U-net-based methods and the original SMIER algorithm demonstrated that the accuracy of the DVFs (Figure 3-6) and the CBCT images was substantially improved (Figure 3-7), especially for those small lung details. Accurate deformation and reconstruction of these small lung details are important for adequate dose accumulation for adaptive therapy [125], and could contribute to important dosimetric biomarkers to assess the toxicity of lung stereotactic body radiation therapy.

In our study, we found the DVF residual errors generated by SMEIR-Bio, SMEIR-U-net-3C and SMEIR-U-net-4C were comparable. No statistical significance was found for the DVF residual error difference between these three methods. As for models trained on MC-simulated dataset, the average DVF residual error was slightly higher for SMEIR-U-net-3C (3.88 mm), as compared to the SMEIR-Bio (3.75 mm) and SMEIR-U-net-4C (3.71 mm) methods. The introduction of image intensity information into SMEIR-U-net-4C potentially helps the method to better align the local intensity differences with local deformation field variations, which however

requires further investigation and verification. For the quantitative metrics of the reconstructed images (RMSE, UQI and NCC), both the U-net-based methods achieved better NCCs as compared to SMEIR-Bio. In terms of the UQI, the performances of U-net-based methods are similar to that of SMEIR-Bio. The RMSE values were comparable between the three methods, while the SMEIR-U-net-4C generated slightly better results. Since SMEIR-Bio used a biomechanical modeling approach assuming homogeneous lung tissues [103, 116], it didn't consider the local heterogeneities and might over-smooth the DVFs as well as the 4D-CBCT images with prominent local variations. Future studies comparing the U-net-based methods to biomechanical modeling with heterogeneity material modeling are warranted [126]. For SMEIR-Bio, the average DVF fine-tuning time was 74.2 ± 11.4 seconds for biomechanical modeling. In comparison, the U-net-based methods took 10.7 ± 1.0 seconds in average to update the DVFs with GPU acceleration. Using the U-net-based methods can further improve the clinical efficiency of the SMEIR-type algorithms.

In this work, we used the Demons DVFs obtained between high-quality 4D-CT images as the 'ground-truth' to train the fine-tuning model. The average residual DVF error of these Demons DVFs, calculated using manually-tracked lung landmarks, was $2.27 \pm 1.08\ mm$. Considering the inter- and intra-observer variations in localizing the lung landmarks, as well as the limitation posed by the CT voxel resolution and slice thickness (1.5 mm), the accuracy of the Demons DVF was slightly over the size of one voxel, and was acceptable for our study. In future, more accurate registration algorithms [127] could be employed to serve a better 'ground-truth' to train a more accurate model, and the results could be compared with our current findings.

In our model, the size of DVFs and images were all down-sampled to tailor to the GPU memory limits (32 GB). The down-sampling might lead to loss of detailed information, which impacted the CNN's accuracy. Though we up-sampled the DVFs back to the original size after the

CNN, the information was not fully recoverable via the cubic interpolation. Similarly, in consideration of the GPU memory limits, we used a batch size of 4 for CNN. Different batch size selections can lead to substantial variations in model performance [128]. The model accuracy can potentially be further improved when a GPU with larger memory becomes available, and further evaluations and comparisons are warranted.

The simulation study enables us to evaluate the reconstructions quantitatively. The feasibility of proposed method is evaluated with Monte Carlo simulated 4D-CBCT projections.

3.5 CONCLUSION

In this study, we developed two U-net based architectures to fine-tune DVFs to improve the accuracy of inter-phase motion models estimated by 2D-3D deformable registration for 4D-CBCT reconstruction. The feasibility of the proposed methods is demonstrated using data simulated by a Monte-Carlo package and a publicly-available dataset (SPARE). The proposed methods can improve the accuracy and the efficiency of 4D-CBCT reconstruction, which can benefit applications like image-guided radiation therapy and adaptive radiation therapy. The application of 4D-CBCT in clinical practice is investigated in CHAPTER FOUR.

4 CHAPTER FOUR
Evaluating motion variation and reconstructing dose for lung Stereotactic Body Radiation Therapy (SBRT) patients using on-board 4D cone-beam CT

4.1 INTRODUCTION

Stereotactic body radiation therapy (SBRT) has become a standard treatment for patients with inoperable, peripherally located early-stage non-small cell lung cancer (NSCLC) because of its superior conformality which can result in high local control rate compared with standard fractionated external beam radiotherapy [129]. Since SBRT is a sophisticated radiation regimen characterized by a high fraction dose and few fractions through the whole treatment course, tumor localization is especially essential for accurate beam delivery. In the lung regions, respiration motion substantially increases the uncertainty of tumor localization, thus large margins are added to the tumor contour to account for tumor localization uncertainty.

With image guidance techniques, inter- and intra-fractional tumor localization errors have been analyzed based on in-room 3D volumetric imaging such as on-board cone-beam computed tomography (CBCT). By matching on-treatment CBCT images acquired at different time points during a treatment fraction to the planning CT images, the intra-fractional deviation of target localization can be accessed [130-132]. However, static 3D-CBCT imaging cannot provide tumor motion range information during a treatment. Comparisons between tumor localization using 3D-CBCT and four-dimensional (4D) CBCT, which characterizes tumor motion over the respiration cycle, have shown that 4D-CBCT can provide more precise lung tumor targeting that considers respiration motion and can achieve better inter-observer agreement [133]. Therefore, 4D-CBCT was considered as a preferred method for tumor localization [134, 135].

The proposed simultaneous motion estimation and image reconstruction (SMEIR) method, dedicated for 4D-CBCT, yields 4D-CBCT images and inter-phase motion models, represented by deformation vector fields (DVFs) which can be used for analyzing tumor motion and dose accumulation [46].

Dose calculation based on CBCT images has been proposed to reconstruct the dose delivered to the patient during treatment [67, 136-139]. By using either a dedicated CBCT Hounsfield Unit (HU) to electron density curve or corrected HU number from planning CT, CBCT-based dose calculation can achieve satisfactory results for static sites. However, for motion involves sites such as lung, motion artifacts in CBCT led to significant dose discrepancies between the doses calculated from planning CT and CBCT images [136]. Therefore, high quality 4D-CBCT with inter-phase motion information is needed for motion involves sites to calculate and accumulate the delivered dose. Enabled by SMEIR-reconstructed high-quality 4D-CBCT and inter-phase DVFs, we evaluated the tumor motion variation in lung SBRT patients among different treatment fractions and developed a 4D-CBCT image-based dose calculation and accumulation tool to reconstruct the actually delivered dose. This 4D-CBCT based dose reconstruction scheme utilizes most updated patient motion model and offers a way to evaluate delivered dose for quality assurance and adaptive radiation therapy.

4.2 METHODS AND MATERIALS

Fourteen targets from 12 lung cancer patients who received SBRT were used to evaluate the motion variation and reconstruct delivered dose based on SMEIR-reconstructed 4D-CBCT. 4D-CT images were acquired with a helical CT scanner (Brilliance Big Bore, Phillips Healthcare,

Cleveland, OH). All treatment plans were generated in the treatment planning system (PINNACLE, Philips Medical Systems, Madison, WI) for an Elekta Synergy system. One patient's treatment had 3 fractions, while the others' had 5 fractions. At each treatment fraction, CBCT acquired right before the beam delivery were used for the analysis. In total, we obtained 68 (13*5+1*3) groups of 4D-CBCT images for dose reconstruction and inter-fractional motion variation evaluation. The number of projections in each CBCT scan ranged from 650 to 710. Using the SMEIR method, we reconstructed 4D-CBCT at each fraction and built a respiration motion model to evaluate the motion pattern variation between CT and CBCT as well as between different treatment fractions. The 4D-CBCT images reconstructed by SMEIR were then used to calculate and evaluate the delivered dose.

4.2.1 SMEIR method

Simultaneous motion estimation and image reconstruction (SMEIR) [46] is a reconstruction algorithm that iterates and alternates between motion-compensated reconstruction and intensity matching-based motion estimation. In this method, CBCT projections are divided into 10 phases based on the diaphragm's motion. The ART-TV[36] method is used to independently reconstruct the initial image of each phase. In this study, we selected the end-of-exhale phase as the reference phase. We used the demons registration algorithm [43] to generate initial DVFs from all other phases to the reference phase (phase 10). The workflow of SMEIR method shows in Figure 3-1 and the detailed the description of SMEIR method is in CHAPTER TWO 2.2.1.1 and 2.2.1.2.

4.2.2 Motion variation evaluation

We extracted tumor motion trajectories from 4D images and compared motion trajectories extracted from planning 4D-CT and 4D-CBCT acquired at each treatment fraction. We also evaluated inter-fraction motion variation, denoted by the difference in motion trajectories between different treatment fractions.

For 4D-CT images, we chose end-of-exhale as the reference phase. We used the B-Spline deformable image registration (Elastix [140]), to generate inter-phase DVFs between the reference phase and other phases. Tumor contours in the reference phase were propagated to other phases using these DVFs. We extracted the tumor center of mass for each phase to form the trajectory of tumor motion during the planning CT acquisition. Displacements of tumor center of mass in the superior-inferior (SI), left-right (LR), and anterior-posterior (AP) directions were extracted separately and combined to form the 3D vectors' motion magnitude.

Table 4-1 Registration accuracy evaluation using 11 lung SBRT patients with landmarks

	Number of Landmarks	Landmarks motion (mm) (EI vs EE)	Registration Residual (mm)
Patient 01	74	4.3	1.4
Patient 02	80	6.3	2.1
Patient 03	79	5.4	2.1
Patient 04	80	6.2	2.0
Patient 05	79	6.8	2.3

Patient 06	70	6.4	2.2
Patient 07	80	4.3	1.6
Patient 08	90	10.8	3.0
Patient 09	80	6.2	3.0
Patient 10	80	6.0	1.5
Patient 11	80	8.3	2.6

We evaluate the deformation registration accuracy using 4D lung SBRT patient data with landmarks [118]. We use the same parameter in the B-Spline to deform the reference phase to other phases and generate the DVFs between the reference phases to other 4D-CT phases. We evaluate the accuracy of DVFs by comparing the displacement of landmarks with the displacement of landmarks extracted from the DVFs generated by B-Spline. The results are shown in the Table 4-1. The comparison shows that the B-Spline deformable image registration we used can achieve high accuracy DVF estimation. Landmarks motion defined as the magnitude of landmarks displacement between end-of-inhale phase and end-of-exhale phase. Meanwhile the registration residual defined as the magnitude of the difference between landmarks displacement and displacement extracted from DVFs. Compared with registration residual in previous publication [118], the deformable registration we can achieve high accuracy and can be used in motion evaluate.

For 4D-CBCT images, we also chose end-of-exhale as the reference phase. SMEIR outputs motion models in the form of DVFs to describe the displacement between the reference phase and the other phases. The tumor center of mass on the 4D-CBCT images were identified from tumor contours. From the DVFs resulted from SMEIR, we extracted the displacements of tumors' centers

of mass from the reference phase to other phases using the average value of a 2x2x2 voxel cube around the center of mass to form the trajectory of tumor motion on the treatment day.

We compared the motion trajectory of 4D-CT images with that of any 4D-CBCT images to evaluate the tumor motion consistency between planning and treatment for each patient. We also compared the trajectories of 4D-CBCT images of different fractions to evaluate the consistency of tumor motion throughout the treatment course. We used the Wilcoxon signed-rank test [141] to evaluate inter-fraction motion pattern differences as well as the motion pattern difference between 4D-CBCT and planning 4D-CT.

4.2.3 Dose recalculation

Figure 4-1 shows the workflow for dose reconstruction and evaluation based on 4D-CBCT images. First, we obtained 4D-CBCT images using SMEIR algorithm and 3D-CBCT image using ART-TV. We also obtained the average CT from 10 phases of 4D-CT images. We used Elastix to rigidly register the 3D-CBCT image to the average CT image. In our clinic, CT based average intensity projection (AIP) are aligned to 3D-CBCT tumor for patient setup in SBRT lung treatment. Since the treatment plan was based on the coordinates of the CT image, we transformed the 3D-CBCT image to the same location in the CT field of view after rigid registration. The third image (from left to right) in Figure 4-1(B) shows an example of this location transformation. Second, 4D-CT images were deformably registered to the 4D-CBCT images, phase by phase, using Elastix. Modified 4D-CBCT (m4D-CBCT) images keep the geometric anatomy from 4D-CBCT images

while having the corrected HU number from the 4D-CT images. The fourth image (from left to right) in Figure 4-1(B) shows the registration result.

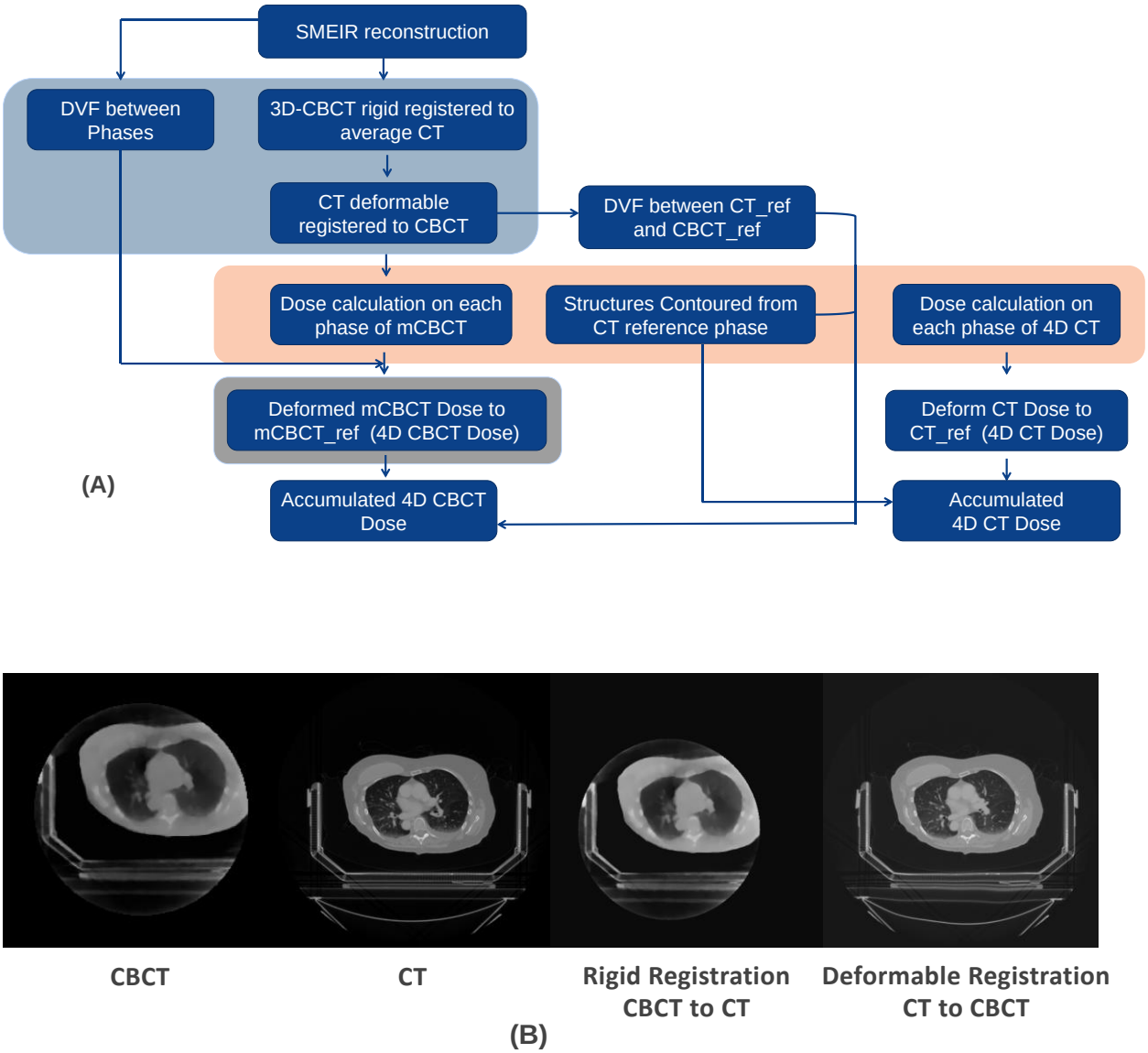

Figure 4-1(A) Workflow of 4D-CBCT based dose reconstruction process (B) Examples of the results after each registration

We used the Eclipse treatment planning system (Varian Medical Systems, Palo Alto, CA, USA) to recalculate the dose based on each phase of the m4D-CBCT images, employing the delivered SBRT treatment plan. Internal target volume drawn by physicians is based on the

maximum intensity projection (MIP) of tumor fusing all phases. An isotropic 5 mm margin is added to the ITV to obtain the planning target volume (PTV).

Using the DVFs generated from SMEIR, we deformed the dose calculated from other phases to the reference phase dose to form the 4D-CBCT based accumulated dose. This accumulated dose at each treatment fraction was then deformed and accumulated to the first treatment fraction, which was considered as the dose delivered during the whole treatment course. Doses were also calculated based on each phase of planning 4D-CT, using the same plan. Using the inter-phase DVFs generated between the 4D-CT reference phase and the other phases, we deformed the dose calculated from each phase 4D-CT image to the 4D-CT reference phase dose to form the accumulated 4D-CT dose, which is the planned dose for the treatment course.

We compared the accumulated 4D-CBCT dose with the planning 4D-CT dose to investigate the potential discrepancy between the delivered dose and the planned dose. The tumor and organs-at-risk, including the spinal cord, lung, and body, were contoured on the reference phase 4D-CT image. DVFs between the reference 4D-CT image and the 4D-CBCT image were obtained using Elastix. Contours were deformed to the 4D-CBCT images from the 4D-CT images. We compared the dose-volume histograms (DVH) from the planning 4D-CT and accumulated 4D-CBCT doses.

4.3 RESULTS

4.3.1 Motion variation evaluation

For a 4D image, motion between the reference phase and other phases is denoted by the displacement of the target's center of mass, represented as a 3D vector containing the displacement in the SI, AP, and LR directions. The motion magnitude is defined as the Euclidean distance between the target's center of mass at the end-of-exhale (reference) phase and at other phases, which is the length of the 3D displacement vector. Figure 4-2 Motion patterns of 4D-CT and 4D-CBCT images for each fraction shows the motion variation of each target. Each point denotes one value of motion magnitude for that phase in the respiration cycle. Compared to motion pattern variations among different treatment fractions, motion patterns changed more between planning 4D-CT and 4D-CBCT, as shown in Figure 4-2.

We used the Wilcoxon signed-rank test to evaluate the motion pattern differences. For each target, we tested the motion pattern difference between planning CT and 4D-CBCT images at each fraction. For each fraction, the motion magnitude of all phases composed one vector. For planning CT, we composed one motion magnitude vector. Therefore, in total, there are 68 pairs of 4D-CT and 4D-CBCT images for motion pattern comparison. Fifty-nine of the 68 pairs showed a statistically significant ($p<0.05$) difference between the 3D vector displacement of the planning CT and 4D-CBCT. For Target 7, we found no statistically significant differences between 4D-CT and 4D-CBCT motion patterns for all 5 fractions. For each target, we also tested the CBCT motion pattern difference between fractions. For each patient, there are 3 or 5 fractions and we can extract the motion pattern for every fraction. The comparison is made between each pair of fractions. For targets with 5 fractions, we can generate 10 comparisons for every pair of fraction. For targets with 3 fractions, we can generate 3 pairs of comparisons. In total, there are 133 inter-fraction pairs of CBCT images for comparing inter-fraction motion patterns. Thirty-five of the 133 pairs showed

statistically significant differences between fractions ($p<0.005$) (The value is 0.005 since Bonferroni correction was applied for multi-comparison test).

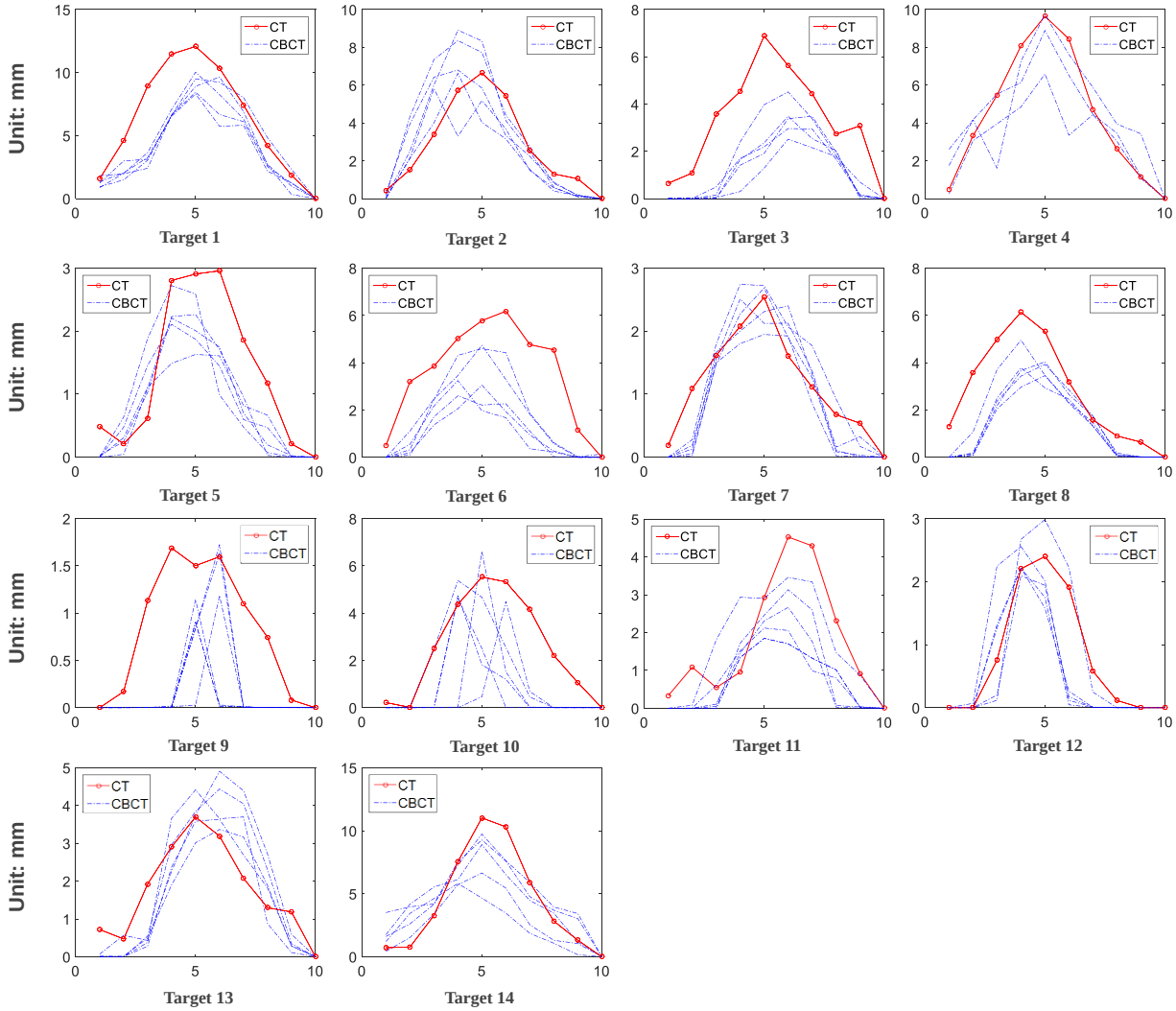

Figure 4-2 Motion patterns of 4D-CT and 4D-CBCT images for each fraction

The red line denotes the tumor trajectory from 4D-CT, and the dashed blue line denotes the tumor trajectory from 4D-CBCT.

4.3.2 Dose calculation

Comparisons between the accumulated 4D-CBCT and planning 4D-CT doses for each patient are shown in Figure 4-3 and Figure 4-4. Tumor size and tumor location inside the lung varied between tumors. Tumor motion patterns also diverged, as shown in section 4.3.1. However, from the DVH of the gross tumor volume (GTV), all targets except Targets 4, 13, and 14 showed high dosimetry agreement between the planning 4D-CT and accumulated 4D-CBCT doses. The motion patterns between 4D-CT and 4D-CBCT and among 4D-CBCT fractions showed statistically significant differences for Target 4, which may account for the DVH difference of the GTV. Our evaluation of the motion variation showed that Target 13's CBCT motion range is greater than its 4D-CT motion range, so the plan may not cover the whole tumor motion during treatment, which may account for the different dose distribution. Target 14 has 2 fractions in which the 4D-CBCT motion range is only half of the CT motion range. This also contributes to the difference between delivered and planned dose distributions. For organs-at-risk, all targets showed high agreement between the accumulated 4D-CBCT and planning 4D-CT doses. The prescribed dose for target 11 is 60 Gy. The DVH matched well before 70 Gy for target 11since, the target 11 the motion range of 4D-CT is larger than that of the 4D-CBCT the tumor is fully covered for dose delivery.

Table 4-2 Quantitative comparison between the 4D-CBCT accumulated dose and the planning 4D-CT dose of GTV.

Target	Prescription Dose (Gy)	4D-CBCT			4D-CT		
		D_{100} (Gy)	D_{90} (Gy)	V_{100}	D_{100} (Gy)	D_{90} (Gy)	V_{100}
1	40	41.2	49.2	100%	43.5	50.0	100%
2	50	43.7	57.6	99.28%	52.1	57.8	100%
3	50	50.8	66.7	100%	56.2	67.9	100%
4	50	59.1	65.4	100%	65.5	68.8	100%

5	60	72.8	81.3	100%	76.9	82.8	100%
6	60	77.7	82.9	100%	80.2	85.9	100%
7	42	43.1	46.7	100%	42.9	46.2	100%
8	54	75.0	76.3	100%	75.2	76.2	100%
9	60	74.8	79.4	100%	71.9	73.9	100%
10	60	77.5	82.8	100%	78	83.5	100%
11	60	63.5	68.2	100%	65.5	70.0	100%
12	60	60.6	65.2	100%	64.7	67.7	100%
13	60	54	65.2	97.49%	64.7	67.7	100%
14	60	59.2	69.6	99.99%	74.0	77.3	100%

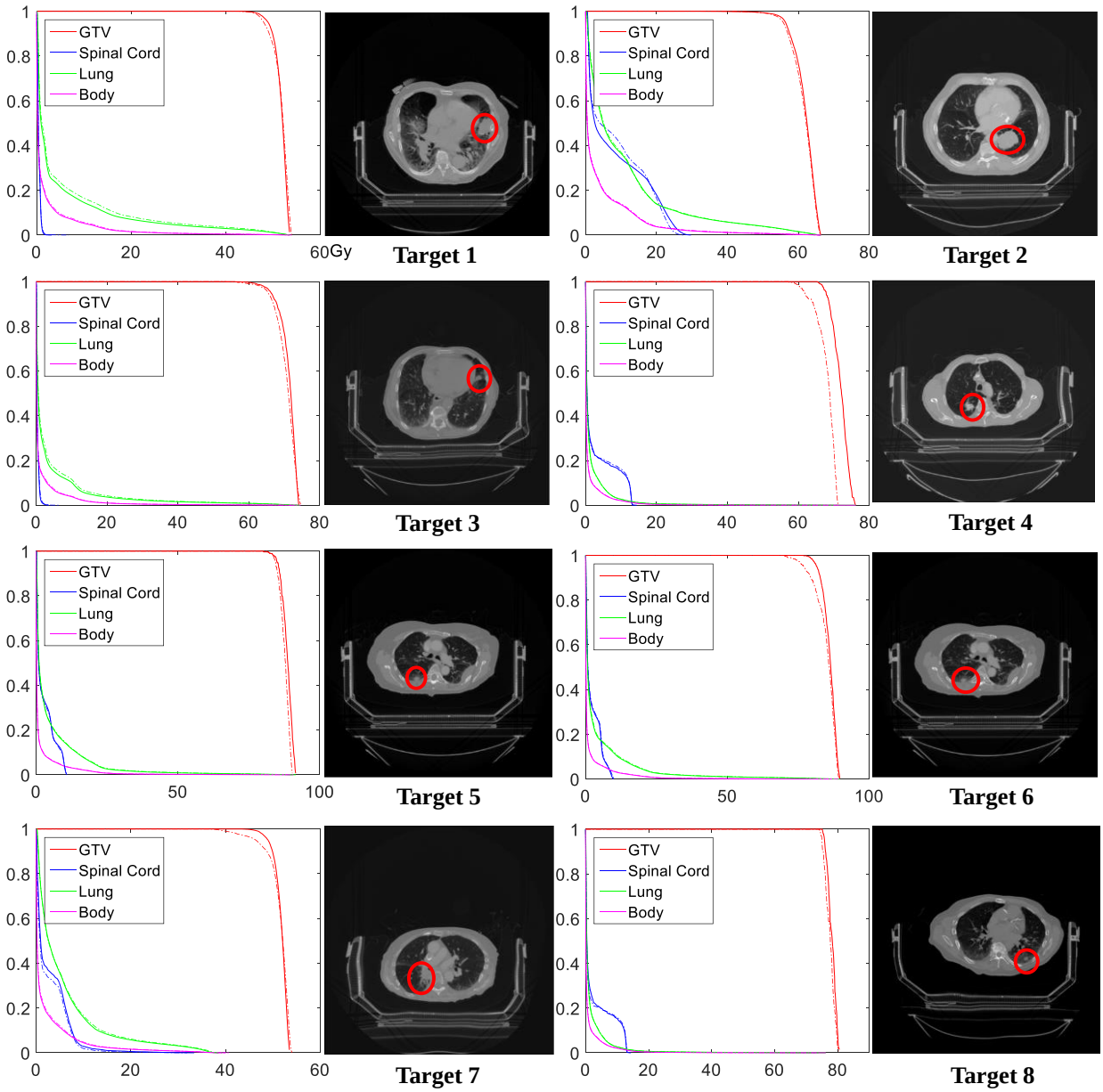

Figure 4-3 DVHs of the accumulated 4D-CBCT dose and the planning 4D-CT dose for Targets 1-8.

The DVH of the accumulated 4D-CBCT is shown by the dashed line, and the accumulated 4D-CT dose is shown by the solid line. For each target, DVHs of the GTV and three organs-at-risk (spinal cord, lung and body) are shown on the left, and one slice of the m4D-CBCT image is shown on the right with the tumor location circled in red.

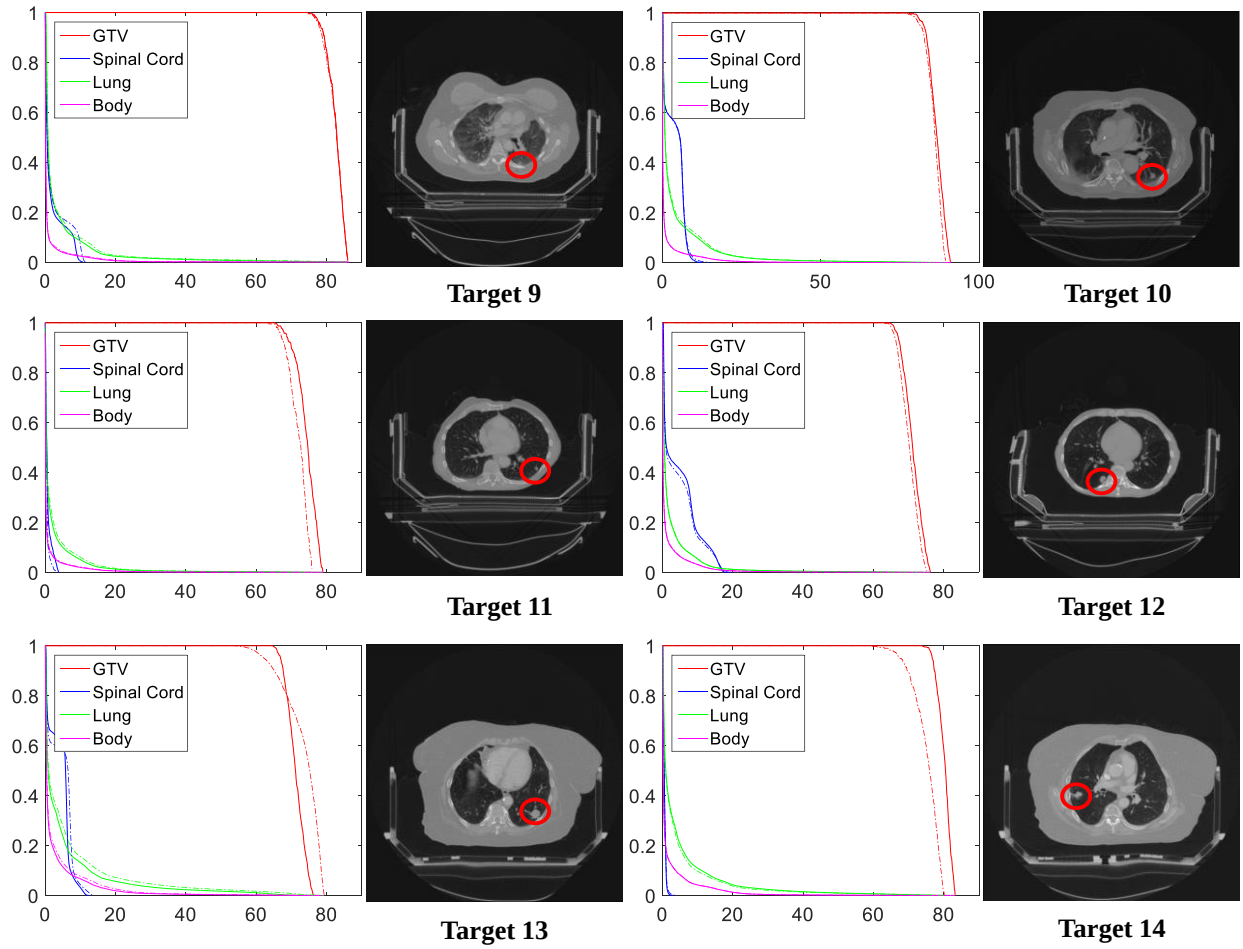

Figure 4-4 DVHs of the accumulated 4D-CBCT dose and the planning 4D-CT dose for Targets 9-14.

The DVH of the accumulated 4D-CBCT is shown by the dashed line, and the planning 4D-CT dose is shown by the solid line. For each target, DVHs of the GTV and three organs-of-risk (spinal cord, lung and body) are shown on the left, and one slice of the m4D-CBCT image is shown on the right with the tumor location circled in red.

We quantified the dose calculation using D_{100} (Gy), D_{90} (Gy), and V_{100}. The quantitative analysis and comparison are shown in Table 4-2. All V_{100} for accumulated 4D-CBCT doses were greater than 97%, meaning more than 97% of the GTV received the prescribed dose. However, 3 of 14 targets, D_{100} of the GTV were smaller than the prescription dose.

4.4 DISCUSSION AND CONCLUSION

This study investigated inter-fraction motion variation as well as motion pattern changes between planning 4D-CT and 4D-CBCT images for lung cancer patients receiving SBRT. In current clinical practice, the tumor motion range at each treatment fraction is not assessed in the standard lung SBRT protocol. Based on the tumor motion characterized by 4D-CT acquired on the simulation day, patient-specific internal margins can be applied to generate an internal treatment volume (ITV). However, tumor motion range and pattern may vary day-to-day as shown in several previous analyses [142-146]. One study[142] based on repeated 4D-CT scans on 8 patients during lung SBRT treatment indicated that the random variation of the motion range for lower lobe tumors is 3.4 mm along the craniocaudal direction in different treatment fractions; the tumor motion range change was more than 10 mm for one patient. Another study[143] on repeated 4D-CT scans also showed tumor motion amplitude changes more than 5 mm in 5 out of 10 patients within the first week of radiotherapy treatment. The results reported in this work echo those previous findings and suggest the importance of re-evaluating tumor motion range and pattern at each treatment fraction. By taking the motion variation between planning 4D-CT and on-treatment 4D-CBCT in to account, the clinical target volume (CTV) margin can be updated to match the motion-of-the-day to avoid missing treatment target and reduce unnecessary margins.

To investigate the influence of tumor motion variation on the delivered dose, we calculated the delivered dose based on 4D-CBCT images obtained at each treatment fraction. We compared the planned dose based on simulation 4D-CT with the accumulated dose based on 4D-CBCT. In the dose reconstruction tool, we used image registration to assign HU value of CT images to CBCT images to obtain the correct HU of the CT images while keeping the CBCT images' geometric information. While the current lung SBRT practice can achieve 100% coverage for GTV in most

of targets, 3 out of 14 GTVs did not receive 100% prescription dose due to large motion variation between planning 4D-CT and on-treatment 4D-CBCT. The tool we developed for dose accumulation based on 4D-CBCT can be used to evaluate the target dose for adaptive radiation therapy.

Our methods applied an advanced 4D-CBCT reconstruction methods which can use 3D-CBCT projections to generate 4D-CBCT images which saved acquisition time and limited on-board image dose obtained by patients, compared with 4D-CBCT acquisition protocol. The SMEIR method we applied can generate the inter-phase motion model simultaneously during the reconstruction. We can directly applied the motion estimated through the SMEIR method to estimate the tumor motion on the treatment day and further applied in the 4D dose calculation as a better measurement for tumor dose received. By applying the advanced 4D-CBCT reconstruction in the 4D dose estimation system, the tool we developed shown its advantage in evaluating the accumulate dose for lung SBRT patients. However, the limitation lies in the speed for image reconstruction, which takes several ours to obtain high-quality 4D-CBCT images. Considering the SBRT treatment protocol that each fraction are delivered daily or every other day [147], the time requirement is acceptable our method. And the other challenge thing is that for lung SBRT, detector cannot always cover the whole body due to the limitation of detector size which will bring FOV truncation for 4D-CBCT images. The outside FOV regions are assigned with 4D-CT images from the corresponding phases, which may bring uncertainty in dose calculation due to the difference between 4D-CT and 4D-CBCT geometry.

In summary, we investigated the tumor motion variation between planning 4D-CT acquisition and each treatment fraction characterized by 4D-CBCT reconstructed by the SMEIR

technique. Tumor motion patterns changed between simulation and treatments while the motion patterns were more consistent during different treatment fractions. We developed a tool that uses 4D-CBCT images to calculate the accumulated 4D radiation dose for lung SBRT. This dose reconstruction tool offers needed information for lung SBRT adaptive radiation therapy.

5 CHAPTER FIVE
Conclusion and future work

5.1 CONCLUSION

To improve the 4D-CBCT image quality for its utilization in IGRT, we have investigated two methods to improve the inter-phase motion model accuracy for a simultaneous motion estimation and image reconstruction (SMEIR) 4D-CBCT scheme. Then, the feasibility of using 4D-CBCT reconstructed with SMEIR reconstruction scheme for IGRT in motion management and dose calculation is evaluated.

The SMEIR method integrates motion estimation and motion-compensated reconstruction into an alternatively iterative loop to update image as well as the inter-phase motion model. The 2D-3D registration in the motion estimation step in SMEIR is based on projection domain intensity matching, which can perform well in the region where projection has high contrast such as lung boundary while the motion model accuracy is low inside lung where the projection contrast in low. The high accuracy motion model at the lung boundary serves as the boundary condition in the biomechanical modeling, which is a physics-driven method by introducing lung tissue related elasticity properties to derive the inner lung motion model from the boundary condition. The comparisons between the original SMEIR and SMEIR-Bio are performed on two aspects: the accuracy of generated DVFs and the 4D-CBCT reconstructed using DVFs generated by different methods. The accuracy of DVFs is evaluated using landmarks' displacement inside of the lung as "ground-truth". 4D-CT is regarded as the "gold-standard" to evaluate reconstructed 4D-CBCT. SMEIR-Bio outperforms SMEIR in both aspects that it can obtain motion estimation inside of the lung with higher accuracy as well as better intricate structures restoration inside lung in 4D-CBCT reconstruction.

In addition to biomechanical modeling based motion estimation, CNN based DVFs fine-tuning framework is proposed under the assumption that the relationship exists between boundary deformation and inner lung deformation and can be learned and employed to solve the inner lung motion model when the boundary DVFs are available. Information stores in the boundary DVFs are extracted and used to estimate the inside lung DVFs through U-net structure. The performance of CNN based DVFs fine-tuning method is compared with the original SMEIR and SMEIR-Bio. Using Monte Carlo simulated projections, U-net based method can bring higher accuracy for the updated inner lung DVFs compared with SMEIR. While U-net and biomechanical modeling have similar performance on the inner lung DVFs derivation. In terms of time, U-net based method outperforms biomechanical modeling with at least 10 times computation time reduction. U-net based methods improve the efficiency for inner lung motion estimation which facilitates clinical adaptation of high quality 4D-CBCT.

High-quality 4D-CBCT images are useful in several aspects of IGART. The first aspect is tumor motion estimation and analysis. 4D-CBCT increases the tumor localization accuracy by offering anatomy of each respiration phase. Therefore, the tumor motion pattern consisting of tumor displacement from reference phase to each respiration phase can be generated and compared with motion pattern obtained from 4D-CT. For most targets, we observed the tumor motion range is larger in CT than CBCT while inter-fraction motion range agreed with each other for most cases. The second aspect is for 4D accumulated dose calculations. As the beam delivery is a dynamic process, dose calculated based on each respiration phase are deformed to the reference phase to obtain accumulated 4D dose. 4D-CBCT accumulated doses are compared to planned dose to monitor and evaluate the delivered dose. The 4D-CBCT based dose reconstruction tool achieves high accuracy, which can be used to evaluate delivered dose for adaptive radiation therapy.

5.2 FUTURE WORK

In this dissertation, methods using biomechanical modeling and CNN are applied to obtain the inner organ motion models when boundary DVFs are available. We can extend the CNN based method to other organs and combine CNN method with biomechanical modeling to improve the accuracy of estimated inner-organ motion model. For example, in the liver region, it is hard to delineate tumor in CBCT image due to low inherent contrast. Deforming contours on CT images to CBCT image can be an alternative method for tumor targeting by estimating DVFs from biomechanical modeling. Biomechanical modeling requires high quality boundary deformation to derive inner liver motion model. 2D-3D registration method is applied to obtain relative high accuracy DVFs in the region that the projection has high contrast such as liver upper boundary. For liver lower boundary region, it is challenging to differentiate liver from surrounding tissues resulting in low accuracy DVFs. In order to obtain high accuracy boundary DVFs, CNN based method can be utilized here to build the relationship between upper and lower boundary DVFs. By inputting upper boundary DVFs, whole liver boundary DVFs can be obtained and used in the biomechanical modeling to generate whole liver motion model.

The CNN based motion estimation scheme has the potential to be used for other image modalities. One example is for real-time lung tumor motion tracking from a single projection. The relationship between the tumor motion in image domain and tumor motion in projection domain can be described and extracted using convolutional neural network. When a new projection comes, the CNN based model can be used to generate the image-domain DVFs. A more sophisticated CNN architecture may be designed for this application.

BIBLIOGRAPHY

[1] R. Baskar, K. A. Lee, R. Yeo, and K.-W. Yeoh, "Cancer and radiation therapy: current advances and future directions," *International journal of medical sciences,* vol. 9, p. 193, 2012.

[2] P. Kelly, P. A. Balter, N. Rebueno, H. J. Sharp, Z. Liao, R. Komaki*, et al.*, "Stereotactic body radiation therapy for patients with lung cancer previously treated with thoracic radiation," *International Journal of Radiation Oncology* Biology* Physics,* vol. 78, pp. 1387-1393, 2010.

[3] S. Gianfaldoni, R. Gianfaldoni, U. Wollina, J. Lotti, G. Tchernev, and T. Lotti, "An overview on radiotherapy: from its history to its current applications in dermatology," *Open access Macedonian journal of medical sciences,* vol. 5, p. 521, 2017.

[4] M. Lederman, "The early history of radiotherapy: 1895–1939," *International Journal of Radiation Oncology* Biology* Physics,* vol. 7, pp. 639-648, 1981.

[5] D. Jaffray, P. Kupelian, T. Djemil, and R. M. Macklis, "Review of image-guided radiation therapy," *Expert review of anticancer therapy,* vol. 7, pp. 89-103, 2007.

[6] D. S. Yoo, T. Z. Wong, and D. M. Brizel, "The role of adaptive and functional imaging modalities in radiation therapy: approach and application from a radiation oncology perspective," in *Seminars in Ultrasound, CT and MRI*, 2010, pp. 444-461.

[7] Q. J. Wu, T. Li, Q. Wu, and F.-F. Yin, "Adaptive radiation therapy: technical components and clinical applications," *The cancer journal,* vol. 17, pp. 182-189, 2011.

[8] C. Western, D. Hristov, and J. Schlosser, "Ultrasound imaging in radiation therapy: From interfractional to intrafractional guidance," *Cureus,* vol. 7, 2015.

[9] S. M. Camps, D. Fontanarosa, F. Verhaegen, and B. G. Vanneste, "The use of ultrasound imaging in the external beam radiotherapy workflow of prostate cancer patients," *BioMed research international,* vol. 2018, 2018.

[10] C.-M. C. Ma and K. Paskalev, "In-room CT techniques for image-guided radiation therapy," *Medical dosimetry,* vol. 31, pp. 30-39, 2006.

[11] A. J. Mundt and J. C. Roeske, *Image-guided radiation therapy: a clinical perspective*: PMPH-USA, 2010.

[12] J. A. Oliver, O. Zeidan, S. L. Meeks, A. P. Shah, J. Pukala, P. Kelly*, et al.*, "Commissioning an in‐room mobile CT for adaptive proton therapy with a compact proton system," *Journal of applied clinical medical physics,* vol. 19, pp. 149-158, 2018.

[13] D. Verellen, M. De Ridder, and G. Storme, "A (short) history of image-guided radiotherapy," *Radiotherapy and Oncology,* vol. 86, pp. 4-13, 2008.

[14] A. L. Boyer, L. Antonuk, A. Fenster, M. Van Herk, H. Meertens, P. Munro*, et al.*, "A review of electronic portal imaging devices (EPIDs)," *Medical physics,* vol. 19, pp. 1-16, 1992.

[15] D. A. Jaffray, J. H. Siewerdsen, J. W. Wong, and A. A. Martinez, "Flat-panel cone-beam computed tomography for image-guided radiation therapy," *International Journal of Radiation Oncology* Biology* Physics,* vol. 53, pp. 1337-1349, 2002.

[16] J. Siewerdsen and D. Jaffray, "Cone‐beam computed tomography with a flat‐panel imager: Effects of image lag," *Medical physics,* vol. 26, pp. 2635-2647, 1999.

[17] L. Feldkamp, L. Davis, and J. Kress, "Practical cone-beam algorithm," *JOSA A,* vol. 1, pp. 612-619, 1984.

[18] J. Boda-Heggemann, F. Lohr, F. Wenz, M. Flentje, and M. Guckenberger, "kV cone-beam CT-based IGRT," *Strahlentherapie und Onkologie,* vol. 187, pp. 284-291, 2011.

[19] Y.-H. Hu, R. Fueglistaller, M. Myronakis, J. Rottmann, A. Wang, D. Shedlock*, et al.*, "Physics considerations in MV-CBCT multi-layer imager design," *Physics in Medicine & Biology,* vol. 63, p. 125016, 2018.

[20] E. Ford, J. Chang, K. Mueller, K. Sidhu, D. Todor, G. Mageras*, et al.*, "Cone‐beam CT with megavoltage beams and an amorphous silicon electronic portal imaging device: Potential for verification of radiotherapy of lung cancer," *Medical physics,* vol. 29, pp. 2913-2924, 2002.

[21] R. E. Colbeth, M. J. Allen, D. J. Day, D. L. Gilblom, M. E. Klausmeier-Brown, J. M. Pavkovich*, et al.*, "Characterization of an amorphous-silicon fluoroscopic imager," in *Medical Imaging 1997: Physics of Medical Imaging*, 1997, pp. 42-51.

[22] E. Kotter and M. Langer, "Digital radiography with large-area flat-panel detectors," *European radiology,* vol. 12, pp. 2562-2570, 2002.

[23] J. J. Sonke, L. Zijp, P. Remeijer, and M. van Herk, "Respiratory correlated cone beam CT," *Medical physics,* vol. 32, pp. 1176-1186, 2005.

[24] T. Li and L. Xing, "Optimizing 4D cone-beam CT acquisition protocol for external beam radiotherapy," *International Journal of Radiation Oncology* Biology* Physics,* vol. 67, pp. 1211-1219, 2007.

[25] M. Zaider and G. Minerbo, "Tumour control probability: a formulation applicable to any temporal protocol of dose delivery," *Physics in Medicine & Biology,* vol. 45, p. 279, 2000.

[26] L. B. Marks, E. D. Yorke, A. Jackson, R. K. Ten Haken, L. S. Constine, A. Eisbruch*, et al.*, "Use of normal tissue complication probability models in the clinic," *International Journal of Radiation Oncology* Biology* Physics,* vol. 76, pp. S10-S19, 2010.

[27] Y. Seppenwoolde, H. Shirato, K. Kitamura, S. Shimizu, M. Van Herk, J. V. Lebesque*, et al.*, "Precise and real-time measurement of 3D tumor motion in lung due to breathing and heartbeat, measured during radiotherapy," *International Journal of Radiation Oncology• Biology• Physics,* vol. 53, pp. 822-834, 2002.

[28] C. W. Hurkmans, M. van Lieshout, D. Schuring, M. J. van Heumen, J. P. Cuijpers, F. J. Lagerwaard*, et al.*, "Quality assurance of 4D-CT scan techniques in multicenter phase III trial of surgery versus stereotactic radiotherapy (radiosurgery or surgery for operable early stage (stage 1A) non–small-cell lung cancer [ROSEL] study)," *International Journal of Radiation Oncology* Biology* Physics,* vol. 80, pp. 918-927, 2011.

[29] J.-J. Sonke and J. Belderbos, "Adaptive radiotherapy for lung cancer," in *Seminars in radiation oncology*, 2010, pp. 94-106.

[30] G. D. Hugo, D. Yan, and J. Liang, "Population and patient-specific target margins for 4D adaptive radiotherapy to account for intra-and inter-fraction variation in lung tumour position," *Physics in medicine and biology,* vol. 52, p. 257, 2006.

[31] T. Li, X. Zhu, D. Thongphiew, W. R. Lee, Z. Vujaskovic, Q. Wu*, et al.*, "On-line adaptive radiation therapy: feasibility and clinical study," *Journal of oncology,* vol. 2010, 2010.

[32] R. Gordon, R. Bender, and G. T. Herman, "Algebraic reconstruction techniques (ART) for three-dimensional electron microscopy and X-ray photography," *Journal of theoretical Biology,* vol. 29, pp. 471-481, 1970.

[33] A. H. Andersen and A. C. Kak, "Simultaneous algebraic reconstruction technique (SART): a superior implementation of the ART algorithm," *Ultrasonic imaging,* vol. 6, pp. 81-94, 1984.

[34] J. Song, Q. H. Liu, G. A. Johnson, and C. T. Badea, "Sparseness prior based iterative image reconstruction for retrospectively gated cardiac micro‐CT," *Medical physics,* vol. 34, pp. 4476-4483, 2007.

[35] G. H. Chen, J. Tang, and S. Leng, "Prior image constrained compressed sensing (PICCS): a method to accurately reconstruct dynamic CT images from highly undersampled projection data sets," *Medical physics,* vol. 35, pp. 660-663, 2008.

[36] E. Y. Sidky and X. Pan, "Image reconstruction in circular cone-beam computed tomography by constrained, total-variation minimization," *Physics in Medicine & Biology,* vol. 53, p. 4777, 2008.

[37] X. Jia, Z. Tian, Y. Lou, J. J. Sonke, and S. B. Jiang, "Four‐dimensional cone beam CT reconstruction and enhancement using a temporal nonlocal means method," *Medical physics,* vol. 39, pp. 5592-5602, 2012.

[38] S. Rit, D. Sarrut, and L. Desbat, "Comparison of analytic and algebraic methods for motion-compensated cone-beam CT reconstruction of the thorax," *IEEE transactions on medical imaging,* vol. 28, pp. 1513-1525, 2009.

[39] T. Li, E. Schreibmann, Y. Yang, and L. Xing, "Motion correction for improved target localization with on-board cone-beam computed tomography," *Physics in medicine and biology,* vol. 51, p. 253, 2005.

[40] T. Li, A. Koong, and L. Xing, "Enhanced 4D cone‐beam CT with inter‐phase motion model," *Medical physics,* vol. 34, pp. 3688-3695, 2007.

[41] S. Rit, J. W. Wolthaus, M. van Herk, and J. J. Sonke, "On‐the‐fly motion‐compensated cone‐beam CT using an a priori model of the respiratory motion," *Medical physics,* vol. 36, pp. 2283-2296, 2009.

[42] J. Wang, T. Li, and L. Xing, "Iterative image reconstruction for CBCT using edge‐preserving prior," *Medical physics,* vol. 36, pp. 252-260, 2009.

[43] J.-P. Thirion, "Image matching as a diffusion process: an analogy with Maxwell's demons," *Medical image analysis,* vol. 2, pp. 243-260, 1998.

[44] M. Brehm, P. Paysan, M. Oelhafen, P. Kunz, and M. Kachelrieß, "Self‐adapting cyclic registration for motion‐compensated cone‐beam CT in image‐guided radiation therapy," *Medical physics,* vol. 39, pp. 7603-7618, 2012.

[45] J. Wang and X. Gu, "High-quality four-dimensional cone-beam CT by deforming prior images," *Physics in medicine and biology,* vol. 58, p. 231, 2012.

[46] J. Wang and X. Gu, "Simultaneous motion estimation and image reconstruction (SMEIR) for 4D cone‐beam CT," *Medical physics,* vol. 40, 2013.

[47] X. Gu, H. Pan, Y. Liang, R. Castillo, D. Yang, D. Choi*, et al.*, "Implementation and evaluation of various demons deformable image registration algorithms on a GPU," *Physics in medicine and biology,* vol. 55, p. 207, 2009.

[48] D. Yang, H. Li, D. A. Low, J. O. Deasy, and I. El Naqa, "A fast inverse consistent deformable image registration method based on symmetric optical flow computation," *Physics in medicine and biology,* vol. 53, p. 6143, 2008.

[49] F. Matthews and J. West, "Finite element displacement analysis of a lung," *Journal of biomechanics,* vol. 5, pp. 591IN7595-594600, 1972.

[50] P.-F. Villard, M. Beuve, B. Shariat, V. Baudet, and F. Jaillet, "Simulation of lung behaviour with finite elements: Influence of bio-mechanical parameters," in *Medical Information Visualisation-Biomedical Visualisation, 2005.(MediVis 2005). Proceedings. Third International COnference on*, 2005, pp. 9-14.

[51] F. Li and F. Porikli, "Biomechanical Simulation of Lung Deformation from One CT Scan," in *Bio-Imaging and Visualization for Patient-Customized Simulations*, ed: Springer, 2014, pp. 15-28.

[52] H. Zhong, J. Kim, H. Li, T. Nurushev, B. Movsas, and I. J. Chetty, "A finite element method to correct deformable image registration errors in low-contrast regions," *Physics in medicine and biology,* vol. 57, p. 3499, 2012.

[53] R. Alterovitz, K. Goldberg, J. Pouliot, I. C. J. Hsu, Y. Kim, S. M. Noworolski*, et al.*, "Registration of MR prostate images with biomechanical modeling and nonlinear parameter estimation," *Medical physics,* vol. 33, pp. 446-454, 2006.

[54] T. A. Sundaram and J. C. Gee, "Towards a model of lung biomechanics: pulmonary kinematics via registration of serial lung images," *Medical image analysis,* vol. 9, pp. 524-537, 2005.

[55] A. Hostettler, D. George, Y. Rémond, S. A. Nicolau, L. Soler, and J. Marescaux, "Bulk modulus and volume variation measurement of the liver and the kidneys in vivo using abdominal kinetics during free breathing," *Computer methods and programs in biomedicine,* vol. 100, pp. 149-157, 2010.

[56] S. Suwelack, H. Talbot, S. Röhl, R. Dillmann, and S. Speidel, "A biomechanical liver model for intraoperative soft tissue registration," in *Medical Imaging 2011: Visualization, Image-Guided Procedures, and Modeling*, 2011, p. 79642I.

[57] Y. Zhang, J. Meyer, H. Lee, J. Tehrani, and J. Wang, "Liver CBCT Reconstruction by Prior-Knowledge Guided Motion Modeling and Biomechanical Modeling," *International Journal of Radiation Oncology• Biology• Physics,* vol. 99, p. S95, 2017.

[58] R. Plantefève, I. Peterlik, N. Haouchine, and S. Cotin, "Patient-specific biomechanical modeling for guidance during minimally-invasive hepatic surgery," *Annals of biomedical engineering,* vol. 44, pp. 139-153, 2016.

[59] M. Sermesant, C. Forest, X. Pennec, H. Delingette, and N. Ayache, "Deformable biomechanical models: Application to 4D cardiac image analysis," *Medical image analysis,* vol. 7, pp. 475-488, 2003.

[60] A. Wittek, K. Miller, R. Kikinis, and S. K. Warfield, "Patient-specific model of brain deformation: Application to medical image registration," *Journal of biomechanics,* vol. 40, pp. 919-929, 2007.

[61] M. Holden, "A review of geometric transformations for nonrigid body registration," *IEEE transactions on medical imaging,* vol. 27, pp. 111-128, 2007.

[62] K. Fukushima, "Neocognitron: A hierarchical neural network capable of visual pattern recognition," *Neural networks,* vol. 1, pp. 119-130, 1988.

[63] A. Krizhevsky, I. Sutskever, and G. E. Hinton, "Imagenet classification with deep convolutional neural networks," in *Advances in neural information processing systems*, 2012, pp. 1097-1105.

[64] J. Long, E. Shelhamer, and T. Darrell, "Fully convolutional networks for semantic segmentation," in *Proceedings of the IEEE conference on computer vision and pattern recognition*, 2015, pp. 3431-3440.

[65] R. Liao, S. Miao, P. de Tournemire, S. Grbic, A. Kamen, T. Mansi*, et al.*, "An artificial agent for robust image registration," in *Thirty-First AAAI Conference on Artificial Intelligence*, 2017.

[66] G. Haskins, J. Kruecker, U. Kruger, S. Xu, P. A. Pinto, B. J. Wood*, et al.*, "Learning deep similarity metric for 3D MR–TRUS image registration," *International journal of computer assisted radiology and surgery,* vol. 14, pp. 417-425, 2019.

[67] J.-J. Sonke, M. Rossi, J. Wolthaus, M. van Herk, E. Damen, and J. Belderbos, "Frameless stereotactic body radiotherapy for lung cancer using four-dimensional cone beam CT guidance," *International Journal of Radiation Oncology* Biology* Physics,* vol. 74, pp. 567-574, 2009.

[68] E. Rietzel, G. T. Chen, N. C. Choi, and C. G. Willet, "Four-dimensional image-based treatment planning: Target volume segmentation and dose calculation in the presence of respiratory motion," *International Journal of Radiation Oncology* Biology* Physics,* vol. 61, pp. 1535-1550, 2005.

[69] S. Beddar, "Respiratory-phase correlated imaging, treatment planning and delivery Clinical Implementation," 2009.

[70] S. Sundaram and C. Feng, "Finite element analysis of the human thorax," *Journal of biomechanics,* vol. 10, pp. 505-516, 1977.

[71] J. M. Kaye, F. P. Primiano, and D. N. Metaxas, "A three-dimensional virtual environment for modeling mechanical cardiopulmonary interactions," *Medical Image Analysis,* vol. 2, pp. 169-195, 1998.

[72] T. Zhang, N. P. Orton, T. R. Mackie, and B. R. Paliwal, "Technical note: A novel boundary condition using contact elements for finite element based deformable image registration," *Medical physics,* vol. 31, pp. 2412-2415, 2004.

[73] A. Al‐Mayah, J. Moseley, M. Velec, and K. Brock, "Sliding characteristic and material compressibility of human lung: Parametric study and verification," *Medical physics,* vol. 36, pp. 4625-4633, 2009.

[74] J. Eom, C. Shi, X. G. Xu, and S. De, "Modeling respiratory motion for cancer radiation therapy based on patient-specific 4DCT data," in *International Conference on Medical Image Computing and Computer-Assisted Intervention*, 2009, pp. 348-355.

[75] J. Eom, X. G. Xu, S. De, and C. Shi, "Predictive modeling of lung motion over the entire respiratory cycle using measured pressure‐volume data, 4DCT images, and finite‐element analysis," *Medical physics,* vol. 37, pp. 4389-4400, 2010.

[76] Y. Zhang, F.-F. Yin, T. Pan, I. Vergalasova, and L. Ren, "Preliminary clinical evaluation of a 4D-CBCT estimation technique using prior information and limited-angle projections," *Radiotherapy and Oncology,* vol. 115, pp. 22-29, 2015.

[77] C. Della Biancia, E. Yorke, C.-S. Chui, P. Giraud, K. Rosenzweig, H. Amols*, et al.*, "Comparison of end normal inspiration and expiration for gated intensity modulated radiation therapy (IMRT) of lung cancer," *Radiotherapy and oncology,* vol. 75, pp. 149-156, 2005.

[78] G. Han, Z. Liang, and J. You, "A fast ray-tracing technique for TCT and ECT studies," in *Nuclear Science Symposium, 1999. Conference Record. 1999 IEEE*, 1999, pp. 1515-1518.

[79] J. Dang, X. Gu, T. Pan, and J. Wang, "A pilot evaluation of a 4-dimensional cone-beam computed tomographic scheme based on simultaneous motion estimation and image reconstruction," *International Journal of Radiation Oncology* Biology* Physics,* vol. 91, pp. 410-418, 2015.

[80] J. Wang and X. Gu, "Simultaneous motion estimation and image reconstruction (SMEIR) for 4D cone-beam CT," *Med Phys,* vol. 40, p. 101912, Oct 2013.

[81] Y. Zhang, J. Ma, P. Iyengar, Y. Zhong, and J. Wang, "A new CT reconstruction technique using adaptive deformation recovery and intensity correction (ADRIC)," *Med Phys,* vol. 44, pp. 2223-2241, Jun 2017.

[82] C. Guetter, H. Xue, C. Chefd'Hotel, and J. Guehring, "Efficient symmetric and inverse-consistent deformable registration through interleaved optimization," in *Biomedical Imaging: From Nano to Macro, 2011 IEEE International Symposium on*, 2011, pp. 590-593.

[83] J. N. Tehrani, Y. Yang, R. Werner, W. Lu, D. Low, X. Guo*, et al.*, "Sensitivity of tumor motion simulation accuracy to lung biomechanical modeling approaches and parameters," *Physics in medicine and biology,* vol. 60, p. 8833, 2015.

[84] Y. Zhang, J. N. Tehrani, and J. Wang, "A biomechanical modeling guided CBCT estimation technique," *IEEE transactions on medical imaging,* vol. 36, pp. 641-652, 2017.

[85] M. C. Boyce and E. M. Arruda, "Constitutive models of rubber elasticity: a review," *Rubber chemistry and technology,* vol. 73, pp. 504-523, 2000.

[86] L. Gao, D. G. Heath, B. S. Kuszyk, and E. K. Fishman, "Automatic liver segmentation technique for three-dimensional visualization of CT data," *Radiology,* vol. 201, pp. 359-364, 1996.

[87] A. H. Foruzan, C. Yen-Wei, R. A. Zoroofi, A. Furukawa, S. Yoshinobu, H. Masatoshi*, et al.*, "Segmentation of liver in low-contrast images using K-means clustering and geodesic active contour algorithms," *IEICE TRANSACTIONS on Information and Systems,* vol. 96, pp. 798-807, 2013.

[88] M. Baiker, J. Milles, J. Dijkstra, T. D. Henning, A. W. Weber, I. Que*, et al.*, "Atlas-based whole-body segmentation of mice from low-contrast Micro-CT data," *Medical image analysis,* vol. 14, pp. 723-737, 2010.

[89] M. Kass, A. Witkin, and D. Terzopoulos, "Snakes: Active contour models," *International journal of computer vision,* vol. 1, pp. 321-331, 1988.

[90] P. A. Yushkevich, J. Piven, H. C. Hazlett, R. G. Smith, S. Ho, J. C. Gee*, et al.*, "User-guided 3D active contour segmentation of anatomical structures: significantly improved efficiency and reliability," *Neuroimage,* vol. 31, pp. 1116-1128, 2006.

[91] Q. Fang and D. A. Boas, "Tetrahedral mesh generation from volumetric binary and grayscale images," in *Biomedical Imaging: From Nano to Macro, 2009. ISBI'09. IEEE International Symposium on*, 2009, pp. 1142-1145.

[92] S. A. Maas, B. J. Ellis, G. A. Ateshian, and J. A. Weiss, "FEBio: finite elements for biomechanics," *Journal of biomechanical engineering,* vol. 134, p. 011005, 2012.

[93] A. E. H. Love, *A treatise on the mathematical theory of elasticity*: Cambridge university press, 2013.

[94] D. Roylance, "Mechanical properties of materials," *Massachusetts Institute of Technology,* pp. 51-78, 2008.

[95] S. J. Lai-Fook, T. A. Wilson, R. E. Hyatt, and J. R. Rodarte, "Elastic constants of inflated lobes of dog lungs," *Journal of Applied Physiology,* vol. 40, pp. 508-513, 1976.

[96] K. Brock, M. Sharpe, L. Dawson, S. Kim, and D. Jaffray, "Accuracy of finite element model‐based multi‐organ deformable image registration," *Medical physics,* vol. 32, pp. 1647-1659, 2005.

[97] I. S. Sokolnikoff, *Mathematical theory of elasticity*, 2nd. Edition ed.: Krieger, Malabar FL, 1983.

[98] G. H. Golub and C. F. Van Loan, *Matrix computations* vol. 3: JHU Press, 2012.

[99] G. Upton and I. Cook, *A dictionary of statistics 3e*: Oxford university press, 2014.

[100] M. B. Rhudy, "Real Time Implementation of a Military Impulse Classifier," University of Pittsburgh, 2010.

[101] Z. Wang, A. C. Bovik, H. R. Sheikh, and E. P. Simoncelli, "Image quality assessment: from error visibility to structural similarity," *IEEE transactions on image processing,* vol. 13, pp. 600-612, 2004.

[102] Z. Zhong, X. Gu, P. Iyengar, W. Mao, X. Guo, and J. Wang, "A Multi-organ Meshing Method for Sliding Motion Modeling in 4D-CBCT Reconstruction," *International Journal of Radiation Oncology• Biology• Physics,* vol. 93, p. S117, 2015.

[103] X. Huang, Y. Zhang, and J. Wang, "A biomechanical modeling guided simultaneous motion estimation and image reconstruction technique (SMEIR-Bio) for 4D-CBCT reconstruction," in *SPIE Medical Imaging*, 2017, pp. 101322B-101322B-9.

[104] T. Gupta and C. A. Narayan, "Image-guided radiation therapy: Physician's perspectives," *Journal of medical physics,* vol. 37, p. 174, 2012.

[105] Y. Zhang, F. F. Yin, and L. Ren, "Dosimetric verification of lung cancer treatment using the CBCTs estimated from limited‐angle on‐board projections," *Medical physics,* vol. 42, pp. 4783-4795, 2015.

[106] B. Seyfi, A. P. Santhanam, and O. J. Ilegbusi, "A Biomechanical Model of Human Lung Deformation Utilizing Patient-Specific Elastic Property," *Journal of Cancer Therapy,* vol. 7, p. 402, 2016.

[107] Y. Zhang, F. F. Yin, W. P. Segars, and L. Ren, "A technique for estimating 4D‐CBCT using prior knowledge and limited‐angle projections," *Medical physics,* vol. 40, 2013.

[108] X. Huang, Y. Zhang, and J. Wang, "A biomechanical modeling-guided simultaneous motion estimation and image reconstruction technique (SMEIR-Bio) for 4D-CBCT reconstruction," *Physics in Medicine & Biology,* vol. 63, p. 045002, 2018.

[109] X. Yang, R. Kwitt, and M. Niethammer, "Fast predictive image registration," in *Deep Learning and Data Labeling for Medical Applications*, ed: Springer, 2016, pp. 48-57.

[110] H. Sokooti, B. de Vos, F. Berendsen, B. P. Lelieveldt, I. Išgum, and M. Staring, "Nonrigid image registration using multi-scale 3D convolutional neural networks," in *International Conference on Medical Image Computing and Computer-Assisted Intervention*, 2017, pp. 232-239.

[111] M.-M. Rohé, M. Datar, T. Heimann, M. Sermesant, and X. Pennec, "SVF-Net: learning deformable image registration using shape matching," in *International Conference on Medical Image Computing and Computer-Assisted Intervention*, 2017, pp. 266-274.

[112] B. D. de Vos, F. F. Berendsen, M. A. Viergever, M. Staring, and I. Išgum, "End-to-end unsupervised deformable image registration with a convolutional neural network," in *Deep Learning in Medical Image Analysis and Multimodal Learning for Clinical Decision Support*, ed: Springer, 2017, pp. 204-212.

[113] O. Ronneberger, P. Fischer, and T. Brox, "U-net: Convolutional networks for biomedical image segmentation," in *International Conference on Medical image computing and computer-assisted intervention*, 2015, pp. 234-241.

[114] J. Wang, W. Mao, and T. Solberg, "Scatter correction for cone-beam computed tomography using moving blocker strips: a preliminary study," *Med Phys,* vol. 37, pp. 5792-800, Nov 2010.

[115] S. A. Maas, B. J. Ellis, G. A. Ateshian, and J. A. Weiss, "FEBio: finite elements for biomechanics," *J Biomech Eng,* vol. 134, p. 011005, Jan 2012.

[116] Y. Zhang, J. N. Tehrani, and J. Wang, "A Biomechanical Modeling Guided CBCT Estimation Technique," *IEEE Trans Med Imaging,* vol. 36, pp. 641-652, Feb 2017.

[117] D. P. Kingma and J. Ba, "Adam: A method for stochastic optimization," *arXiv preprint arXiv:1412.6980,* 2014.

[118] R. Werner, J. Ehrhardt, R. Schmidt, and H. Handels, "Patient‐specific finite element modeling of respiratory lung motion using 4D CT image data," *Medical physics,* vol. 36, pp. 1500-1511, 2009.

[119] X. Jia, H. Yan, L. Cerviño, M. Folkerts, and S. B. Jiang, "A GPU tool for efficient, accurate, and realistic simulation of cone beam CT projections," *Medical physics,* vol. 39, pp. 7368-7378, 2012.

[120] Y. Xu, T. Bai, H. Yan, L. Ouyang, A. Pompos, J. Wang*, et al.*, "A practical cone-beam CT scatter correction method with optimized Monte Carlo simulations for image-guided radiation therapy," *Physics in Medicine & Biology,* vol. 60, p. 3567, 2015.

[121] C. De Boor, C. De Boor, E.-U. Mathématicien, C. De Boor, and C. De Boor, *A practical guide to splines* vol. 27: springer-verlag New York, 1978.

[122] C. C. Shieh, Y. Gonzalez, B. Li, X. Jia, S. Rit, C. Mory*, et al.*, "SPARE: Sparse‐view reconstruction challenge for 4D cone‐beam CT from a 1‐min scan," *Medical physics,* vol. 46, pp. 3799-3811, 2019.

[123] H. Abdi, "Bonferroni and Šidák corrections for multiple comparisons."

[124] E. W. Weisstein, "Bonferroni correction," 2004.

[125] Q. J. Wu, T. Li, Q. Wu, and F. F. Yin, "Adaptive radiation therapy: technical components and clinical applications," *Cancer J,* vol. 17, pp. 182-9, May-Jun 2011.

[126] A. Al-Mayah, J. Moseley, M. Velec, S. Hunter, and K. Brock, "Deformable image registration of heterogeneous human lung incorporating the bronchial tree," *Med Phys,* vol. 37, pp. 4560-71, Sep 2010.

[127] M. Li, E. Castillo, X. L. Zheng, H. Y. Luo, R. Castillo, Y. Wu*, et al.*, "Modeling lung deformation: a combined deformable image registration method with spatially varying Young's modulus estimates," *Med Phys,* vol. 40, p. 081902, Aug 2013.

[128] Y. Wu and K. He, "Group normalization," in *Proceedings of the European Conference on Computer Vision (ECCV)*, 2018, pp. 3-19.

[129] T. B. Lanni Jr, I. S. Grills, L. L. Kestin, and J. M. Robertson, "Stereotactic radiotherapy reduces treatment cost while improving overall survival and local control over standard fractionated radiation therapy for medically inoperable non-small-cell lung cancer," *American journal of clinical oncology,* vol. 34, pp. 494-498, 2011.

[130] T. G. Purdie, J.-P. Bissonnette, K. Franks, A. Bezjak, D. Payne, F. Sie*, et al.*, "Cone-beam computed tomography for on-line image guidance of lung stereotactic radiotherapy: localization, verification, and intrafraction tumor position," *International Journal of Radiation Oncology* Biology* Physics,* vol. 68, pp. 243-252, 2007.

[131] I. S. Grills, G. Hugo, L. L. Kestin, A. P. Galerani, K. K. Chao, J. Wloch*, et al.*, "Image-guided radiotherapy via daily online cone-beam CT substantially reduces margin requirements for stereotactic lung radiotherapy," *International Journal of Radiation Oncology* Biology* Physics,* vol. 70, pp. 1045-1056, 2008.

[132] L. Masi, F. Casamassima, C. Menichelli, K. Pasciuti, R. Doro, C. Polli*, et al.*, "On-line image guidance for frameless stereotactic radiotherapy of lung malignancies by cone beam CT: comparison between target localization and alignment on bony anatomy," *Acta Oncologica,* vol. 47, pp. 1422-1431, 2008.

[133] R. A. Sweeney, B. Seubert, S. Stark, V. Homann, G. Müller, M. Flentje*, et al.*, "Accuracy and inter-observer variability of 3D versus 4D cone-beam CT based image-guidance in SBRT for lung tumors," *Radiation Oncology,* vol. 7, p. 81, 2012.

[134] J. Santoro, J. McNamara, E. Yorke, H. Pham, A. Rimner, K. Rosenzweig*, et al.*, "A study of respiration‐correlated cone‐beam CT scans to correct target positioning errors in radiotherapy of thoracic cancer," *Medical physics,* vol. 39, pp. 5825-5834, 2012.

[135] J.-J. Sonke, J. Lebesque, and M. Van Herk, "Variability of four-dimensional computed tomography patient models," *International Journal of Radiation Oncology* Biology* Physics,* vol. 70, pp. 590-598, 2008.

[136] Y. Yang, E. Schreibmann, T. Li, C. Wang, and L. Xing, "Evaluation of on-board kV cone beam CT (CBCT)-based dose calculation," *Physics in medicine and biology,* vol. 52, p. 685, 2007.

[137] M. L. Schmidt, L. Hoffmann, M. Kandi, D. S. Møller, and P. R. Poulsen, "Dosimetric impact of respiratory motion, interfraction baseline shifts, and anatomical changes in radiotherapy of non-small cell lung cancer," *Acta Oncologica,* vol. 52, pp. 1490-1496, 2013.

[138] I. Fotina, J. Hopfgartner, M. Stock, T. Steininger, C. Lütgendorf-Caucig, and D. Georg, "Feasibility of CBCT-based dose calculation: comparative analysis of HU adjustment techniques," *Radiotherapy and Oncology,* vol. 104, pp. 249-256, 2012.

[139] G. Altorjai, I. Fotina, C. Lütgendorf-Caucig, M. Stock, R. Pötter, D. Georg*, et al.*, "Cone-beam CT-based delineation of stereotactic lung targets: the influence of image modality and target size on interobserver variability," *International Journal of Radiation Oncology* Biology* Physics,* vol. 82, pp. e265-e272, 2012.

[140] S. Klein, M. Staring, K. Murphy, M. A. Viergever, and J. P. Pluim, "Elastix: a toolbox for intensity-based medical image registration," *IEEE transactions on medical imaging,* vol. 29, pp. 196-205, 2010.

[141] R. Woolson, "Wilcoxon signed‐rank test," *Wiley encyclopedia of clinical trials,* pp. 1-3, 2007.

[142] K. Matsugi, Y. Narita, A. Sawada, M. Nakamura, Y. Miyabe, Y. Matsuo*, et al.*, "Measurement of interfraction variations in position and size of target volumes in stereotactic body radiotherapy for lung cancer," *Int J Radiat Oncol Biol Phys,* vol. 75, pp. 543-8, Oct 1 2009.

[143] K. R. Britton, G. Starkschall, S. L. Tucker, T. Pan, C. Nelson, J. Y. Chang*, et al.*, "Assessment of gross tumor volume regression and motion changes during radiotherapy for non-small-cell lung cancer as measured by four-dimensional computed tomography," *Int J Radiat Oncol Biol Phys,* vol. 68, pp. 1036-46, Jul 15 2007.

[144] M. Guckenberger, J. Wilbert, J. Meyer, K. Baier, A. Richter, and M. Flentje, "Is a single respiratory correlated 4D-CT study sufficient for evaluation of breathing motion?," *Int J Radiat Oncol Biol Phys,* vol. 67, pp. 1352-9, Apr 1 2007.

[145] J. P. Bissonnette, K. N. Franks, T. G. Purdie, D. J. Moseley, J. J. Sonke, D. A. Jaffray*, et al.*, "Quantifying interfraction and intrafraction tumor motion in lung stereotactic body radiotherapy using respiration-correlated cone beam computed tomography," *Int J Radiat Oncol Biol Phys,* vol. 75, pp. 688-95, Nov 1 2009.

[146] J. J. Sonke, J. Lebesque, and M. van Herk, "Variability of four-dimensional computed tomography patient models," *Int J Radiat Oncol Biol Phys,* vol. 70, pp. 590-8, Feb 1 2008.

[147] R. D. Timmerman, "An overview of hypofractionation and introduction to this issue of seminars in radiation oncology," in *Seminars in radiation oncology*, 2008, pp. 215-222.